Advanced Space Plasma Simulations Using a High-Order Accurate Method and the Magnetohydrodynamics with Embedded Particle-in-Cell Model

by

Yuxi Chen

A dissertation submitted in partial fulfillment
of the requirements for the degree of
Doctor of Philosophy
(Atmospheric, Oceanic, and Space Sciences and Scientific Computing)
in The University of Michigan
2017

Doctoral Committee:

Research Professor Gábor Tóth, Co-Chair
Professor Tamas I. Gombosi, Co-Chair
Associate Professor Xianzhe Jia
Professor Kenneth G. Powell
Professor James A. Slavin

Yuxi Chen

yuxichen@umich.edu

ORCID ID: 0000-0001-7288-2805

ACKNOWLEDGEMENTS

This dissertation has been made possible with the help from many people, whom I would like to acknowledge and thank.

First and foremost, I would like to thank my advisors, Prof. Gabor Toth and Prof. Tamas Gombosi, for their financial support, excellent and patient guidance. I feel very fortunate to have the opportunity to study at the University of Michigan and work with my advisors. What they have taught me, including the physics knowledge, the numerical techniques, as well as the strict working attitude, will continuously benefit my future career. I would like to thank Prof. James Slavin and Prof. Xianzhe Jia for their valuable suggestions on my research. I would like to thank Prof. Kenneth Powell for serving on my committee.

I also would like to thank my colleagues and friends, with whom I have had a great time in Michigan. Finally, I would like to thank my parents, my brother and my wife, for their love and support.

TABLE OF CONTENTS

LIST OF FIGURES

Figure

LIST OF TABLES

Table

ABSTRACT

Global magnetohydrodynamics (MHD) models have been important tools for space physics research in recent decades. In order to improve the numerical accuracy and the physics capability of an MHD mode, a fifth-order accurate finite difference scheme for hyperbolic equations on block-adaptive curvilinear grids is developed to improve the accuracy of the Michigan MHD model BATS-R-US. To model kinetic phenomena, like magnetic reconnection, BATS-R-US is two-way coupled with a particle-in-cell (PIC) code iPIC3D to incorporate kinetic physics into a global model. The two-way coupled model is called magnetohydrodynamics with embedded particle-in-cell (MHD-EPIC) model. This dissertation research focuses on the development of the fifth-order scheme and the applications of the MHD-EPIC model.

The fifth-order finite-difference scheme constructs the face fluxes with a monotonicity preserving limiter MP5, and achieves high-order spatial derivatives by a flux correction step. This scheme is generalized to curvilinear grids with a free-streaming discretization. For the locally refined mesh, high-order accuracy is also achieved by careful interpolation of ghost cells near the grid resolution changes. Numerical tests are presented to demonstrate the accuracy and robustness of the algorithm.

The MHD-EPIC model is applied to study Earth's dayside magnetopause reconnection and Mercury's magnetotail reconnection. From the Earth simulation, the generation and evolution of flux transfer events (FTEs) are studied. It is found the magnetic field signature of FTEs at their early formation stage is similar to a 'crater FTE'. After the FTE core field grows to a significant value, it becomes an FTE with typical flux rope structure. Kinetic phenomena, such as the crescent electron phase

space distribution, the Larmor electric field, and the lower hybrid drift instability are identified from the global simulation. The Mercury simulations apply MHD-EPIC to study the magnetotail reconnection. The properties of the magnetotail flux ropes agree well with the MESSENGER observations. The reconnection dawn-dusk asymmetry also arises from the simulations; the reconnection jets are stronger on the dawn side, which agrees with the MESSENGER observations.

CHAPTER I

Introduction

This dissertation consists of the development of a high-order scheme, and the magnetospheric simulations with the magnetohydrodynamics with embedded particle-in-cell (MHD-EPIC) model. This chapter will present the physics background first, and then introduce the numerical techniques and model details.

1.1 Solar Wind-Magnetosphere Interaction

As the only star in our solar system, the Sun is the energy source for most space physics phenomena. The solar wind originating from the solar surface controls the dynamics of the inner planetary magnetospheres. This section describes the solar wind and its interaction with Earth's and Mercury's magnetospheres.

1.1.1 Solar Wind

The solar wind is a stream of ions and electrons originating from the solar corona, which is part of the solar upper atmosphere. By observing the motions of comet tails, *Biermann* (1951) suggested that the gas continuously flowing outward from the Sun has a velocity of 500 km/s to 1500 km/s. *Parker* (1958, 1965) studied the solar atmosphere with detailed mathematical analyses. He pointed out that a static equilibrium solution does not exist for the solar atmosphere and the solar wind is

accelerated to be supersonic by the pressure gradient between the solar corona base and the interplanetary space. He also predicted that the interplanetary magnetic field (IMF), one end of which is fixed at the sun, is twisted due to the rotation of the sun. The twisted structure of IMF is called the Parker spiral. Based on the differences in the solar wind composition and velocity, the solar wind is classified into two types: the slow wind with a typical velocity of $300 \sim 500\,\mathrm{km/s}$ and a composition that is similar to the corona, and the fast wind with a typical velocity of $750\,\mathrm{km/s}$ and a composition that matches the photosphere. At 1 AU, the typical solar wind velocity is about $400\,\mathrm{km/s}$, density is $7\,\mathrm{amu/cm^3}$, proton temperature is $10^5\,\mathrm{K}$, and magnetic field strength is about $7\,\mathrm{nT}$ (*Kivelson and Russell*, 1995).

Since the solar wind consists of ions and electrons, which is also called plasma, these charged particles interact with magnetized planets. The interaction between the solar wind and planetary intrinsic magnetic fields drives the formation and evolution of planetary magnetospheres. The magnetospheres of Earth and Mercury are studied in this dissertation, and their properties are introduced in the following subsections.

1.1.2 Earth's Magnetosphere

Earth's intrinsic magnetic field can be approximated by a dipole with field strength of $31000\,\mathrm{nT}$ at the magnetic equator. The structure of the dipole field is reshaped by the supersonic solar wind. The region that is dominated by the Earth's intrinsic magnetic field is the magnetosphere. A cartoon to illustrate the structure of Earth's magnetosphere is shown in Figure 1.1.

Since the solar wind is supersonic and also super-Alfvenic with fast magnetosonic Mach number (M_f) of $6 \sim 12$ at 1 AU, a bow shock forms before the solar wind reaches the edge of the magnetosphere. Across the bow shock, the solar wind is compressed, heated and slowed. Relative to the Earth, the solar wind speed reduces from super-Alfvenic to sub-Alfvenic so that information can propagate from the edge

of the magnetosphere to the bow shock. The location of the bow shock depends on the properties of the solar wind, as well as the size and shape of the obstacle body. For the Earth's bow shock, it is about 3 R_E away from the edge of the magnetosphere near the Sun-Earth line. Behind the shock, the plasma flow is slowed down but it is still moving around the Earth. The interface, where the magnetic pressure of the confined Earth's dipole field balances the total pressure of the shocked solar wind, is known as magnetopause. The region between the magnetopause and the bow shock is the magnetosheath. The magnetic field lines of the dipole are compressed on the dayside, while they are stretched on the nightside to form the magnetotail. The magnetotail is divided into two parts by the current sheet: the northern lobe contains magnetic field lines pointing towards the Earth while the southern lobe magnetic field is pointing away from the Earth. The structure shown in Figure 1.1 is just the average state of the magnetosphere. Driven by the varying solar wind, the whole magnetosphere can change dynamically.

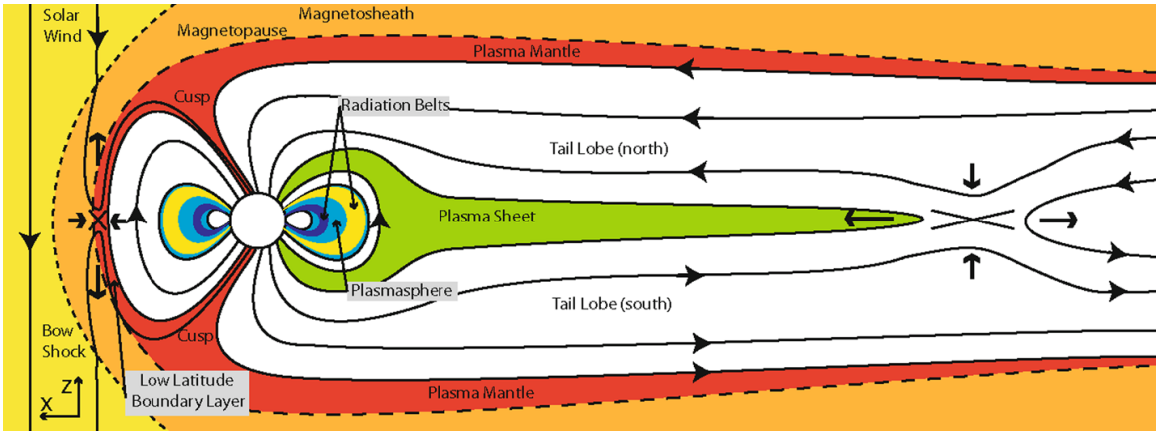

Figure 1.1: The structure of Earth's magnetosphere (from *Eastwood et al.* (2015)).

1.1.2.1 Dungey cycle

Dungey (1961) discussed the global magnetospheric convection, and he predicted the magnetic reconnection at both the dayside magnetopause and the magnetotail.

This convection model is known as Dungey cycle. Figure 1.2 is a carton showing different phases of a Dungey cycle. The reconnection between the solar wind magnetic field lines and the dipole field lines at the dayside magnetopause creates open field lines. One end of the open field lines is connected to the Earth and the other end is linked to the solar wind. These open field lines form a channel for the solar wind plasma penetrating into the magnetosphere. Since the open field lines are moving together with the tailward moving magnetosheath plasma, these field lines are transported from the dayside to the tailside, and accumulate in the tail. The magnetic reconnection at the tail closes the open field lines and transports the magnetic flux back to the dayside. A Dungey cycle takes about 1 hour for Earth.

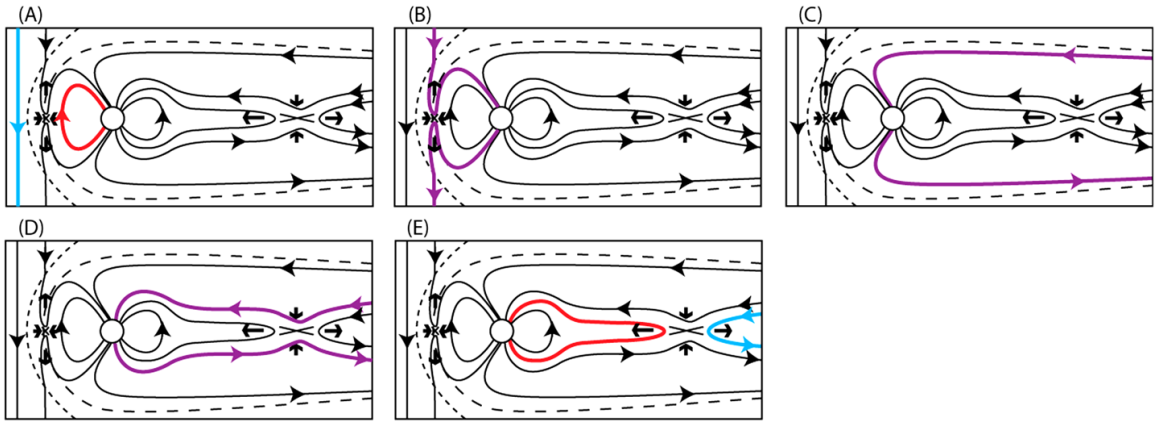

Figure 1.2: The progression of the Dungey cycle (from *Eastwood et al.* (2015)).

1.1.2.2 Magnetic Reconnection

During the magnetic reconnection process, the magnetic field lines break and reconnect. This topology rearrangement process is accompanied with the energy conversion from magnetic energy to kinetic and thermal energy. The Sweet-Parker reconnection model (*Parker*, 1957) has been successfully applied to explain the magnetic reconnection in a collisional plasma. However, the plasma in the solar wind or inside the magnetospheres is collisionless, and the magnetic reconnection described

by the Sweet-Parker model is not fast enough to match the observation results. Hall effect, which is caused by the electron-ion velocity difference at the sub-ion gyroradius scales, probably plays an important role in the reconnection process. A set of simulations have demonstrated that the magnetic reconnection can be fast once the Hall effect is included in the numerical models (*Birn et al.*, 2001; *Ma and Bhattacharjee*, 2001; *Drake et al.*, 2008). Evidences that support the occurrence of Hall reconnection have been observed as well (*Nagai et al.*, 2001; *Phan et al.*, 2007).

Magnetic reconnection has been an important research topic for both the plasma and space physics communities in the past decades, but a lot of mysteries still need to be discovered. A few of the magnetosphere related unknown questions are listed as examples:

- How is the magnetopause reconnection related to other dayside dynamics, such as flux transfer events (FTEs)? What is the global reconnection rate? How much solar wind plasma is transferred into the magnetosphere by reconnection?

- How is the magnetic reconnection at the near-Earth magnetotail triggered? What is the relationship between the near-Earth reconnection and the magnetospheric substorm?

The knowledge about the kinetic features of reconnection as well as the global effects of reconnection are needed to answer these questions.

1.1.2.3 Flux Transfer Events

Flux transfer events (FTEs) are widely considered as a phenomenon related to dayside non-steady reconnection (*Russell and Elphic*, 1978). An FTE is a bundle of reconnected magnetic fluxtubes created at the magnetopause and moving anti-sunward along the magnetopause. A cartoon showing the structure of FTEs is presented in Figure 1.3. Such events are characterized by a bipolar variation of the magnetopause

normal magnetic field B_N, and are usually associated with an enhancement of core field, the magnetic field component along the axial direction of the FTE. An FTE exhibits a flux-rope structure in three-dimensional space. It has been observed that the plasma inside an FTE is usually a mixture of magnetospheric and magnetosheath plasma (*Daly et al.*, 1981), indicating that FTEs are generated by magnetic reconnection process. The diameter of an FTE can vary from several ion inertial lengths (*Eastwood et al.*, 2016) (a few hundred kilometers) to several Earth radii (*Rijnbeek et al.*, 1984; *Hasegawa et al.*, 2006). In the dawn-dusk direction along the magnetopause, FTEs can extend over a long distance (*Fear et al.*, 2008). FTEs frequently occur as a quasi-periodic process, and *Rijnbeek et al.* (1984) reported that the FTEs were observed about every 8 minutes during periods of southward magnetosheath magnetic field.

FTEs have been studied with various global numerical models. Compared to local simulations, a global model can offer more realistic plasma and magnetic field context. *Fedder et al.* (2002) used a global ideal MHD model to study the generation of FTEs. The typical magnetic field signature is captured by their model, and their simulation suggests that the FTEs are formed by non-steady reconnection along the separator at the magnetopause. *Raeder* (2006) performed a high resolution ideal MHD simulation with the OpenGGCM model. FTEs formed by multiple X line reconnection with a tilted dipole field in this study. *Dorelli and Bhattacharjee* (2009) revisited the FTE generation mechanism with resistive MHD using the OpenGGCM model, and the authors argue that the FTEs are generated by flow vortices and the formation of new X lines is the consequence, rather than the cause of FTE formation. *Sibeck et al.* (2008) studied crater FTEs with the BATS-R-US MHD model. All these global simulations are based on ideal or resistive MHD codes, and the generation of FTEs relies either on ad hoc resistivity (*Dorelli and Bhattacharjee*, 2009) or numerical resistivity (*Fedder et al.*, 2002; *Raeder*, 2006). Recently, a two-dimensional global magneto-

spheric hybrid-Vlasov simulation was performed to study the global magnetopause reconnection rate and the production of FTEs by *Hoilijoki et al.* (2017).

Typical FTEs are associated with an enhancement of the field strength at the center of a flux rope. On the other hand, the so-called crater FTEs show more complicated structure: the center field is surrounded by two 'trenches' and the field strength usually show a dip just at the center (*LaBelle et al.*, 1987; *Owen et al.*, 2008). The FTEs with enhanced core field are more frequently observed than crater FTEs (*Zhang et al.*, 2010). The generation mechanism of crater FTEs has been explored with both numerical simulations (*Sibeck et al.*, 2008) and analytic models (*Zhang et al.*, 2010). *Zhang et al.* (2010) proposed that crater FTEs are the initial stage of typical FTEs based on hundreds of events selected from THEMIS observations. The structure of the core field can be even more complicated, for example, *Eriksson et al.* (2016) found a tripolar core field flux rope at the magnetopause.

1.1.3 Mercury's Magnetosphere

Mercury is the innermost and also the smallest planet in the solar system. It has a rocky Earth-like body with radius of $R_M = 2440\,\mathrm{km}$. Mariner 10 was first spacecraft launched to fly by Mercury. These flybys provided us the basic knowledge about Mercury's magnetosphere and its ambient space environment. About 30 years later, the MErcury Surface, Space ENvironment, GEochemistry, and Ranging (MESSENGER) spacecraft revisited Mercury, and gave us a chance to have a close look at Mercury's magnetosphere. MESSENGER impacted Mercury's surface on 30 April 2015 after its four-year orbiting around Mercury. More secrets of Mercury are still waiting to be discovered by the upcoming dual-spacecraft BepiColombo mission.

Mercury has a relatively small but dynamic magnetosphere due to its weak intrinsic magnetic field and the strong ambient solar wind. Its intrinsic magnetic field can be approximated by a dipole field with equatorial magnetic field strength of

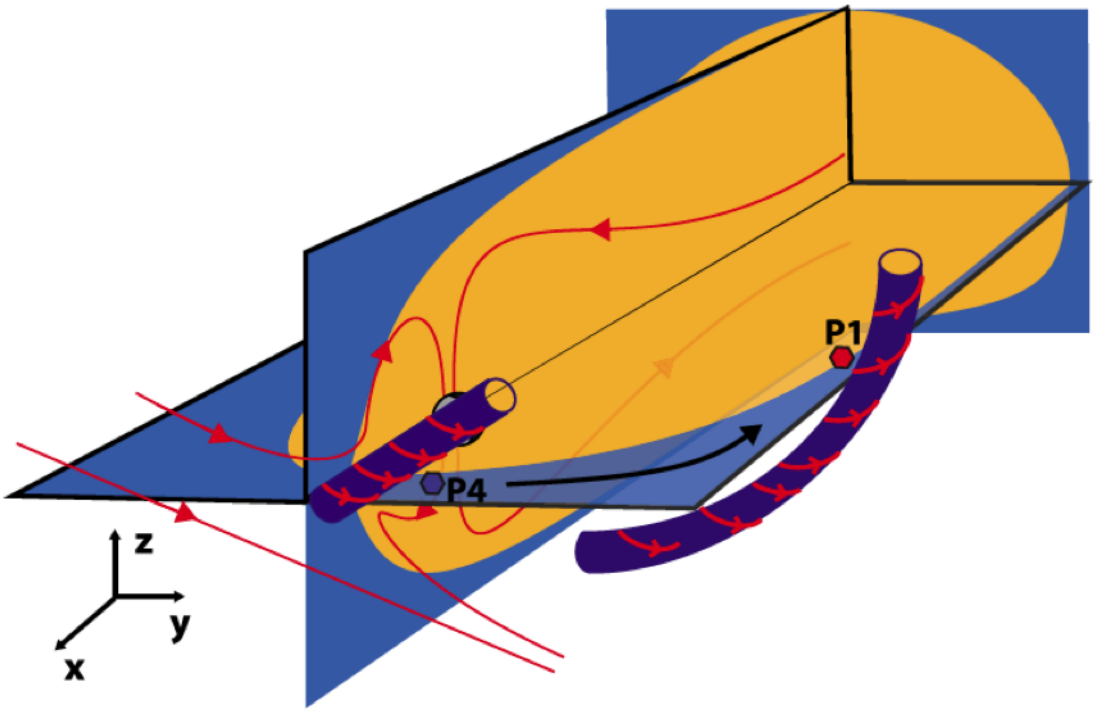

Figure 1.3: The structure of FTEs under IMF conditions of $B_y > 0$ and $B_z < 0$. (from *Eastwood et al.* (2012)).

200 nT, which is about 1/150 of Earth's equatorial field strength. The center of the dipole field is offset northward about $0.2\,R_M$ (*Anderson et al.*, 2011). The solar wind has already been accelerated to a value close to its asymptotic speed (typically 400 km/s) at Mercury's orbit of $0.31 \sim 0.47$ AU, and the solar wind density is about 40 amu/cm^3, resulting in a dynamic pressure of 11 nPa, which is much larger than that at Earth. Compared with Earth, the interaction between the weaker intrinsic magnetic field and higher solar wind dynamic pressure creates the smaller Mercury's magnetosphere. Figure 1.4 is a cartoon showing the typical structure of Mercury's magnetosphere, which consists of the bow shock, the magnetosheath, the magnetopause, the cusps, the magnetotail and several boundary layers. The structure of Mercury's magnetosphere is similar to that of Earth, but the scales are different. The averaged subsolar magnetopause distance to the surface is $1.45\,R_M$ (*Winslow et al.*,

2013), and the diameter of the magnetotail is about $5\,R_M$. The small size of the magnetosphere leads to a fast Dungey cycle period of ~ 2 min (*Slavin et al.*, 2009).

Since the averaged magnetopause location is only $1.45\,R_M$ away from the Mercury's surface, *Slavin and Holzer* (1979) suggested that the Hermaean magnetopause has a significant chance to be eroded to very low altitude due to the magnetopause reconnection, so that the solar wind can directly interact with Mercury's surface. However, a large proportion of Mercury's interior is filled with highly conducting material (*Smith et al.*, 2012). The induction effect arising from the conducting core can strengthen Mercury's intrinsic magnetic field, therefore may prevent the collapse of the dayside magnetosphere (*Hood and Schubert*, 1979; *Suess and Goldstein*, 1979). *Jia et al.* (2015) demonstrated that the induction effect of the conducting core does stiffen the dayside magnetosphere from global MHD simulations. Dayside magnetopause reconnection erodes the dayside magnetosphere, but the induction effect strengths the intrinsic magnetic field. These two effects play important roles on dayside magnetospheric dynamics. The questions, such as whether the magnetopause can be eroded to the surface and what is the solar wind conditions that can result in such strong erosion, still needs to be clarified.

Flux ropes, which are the products of magnetic reconnection, are found in Mercury's magnetotail. *Slavin et al.* (2009, 2012) analyzed the flux ropes based on the magnetic field data from the MESSENGER flybys. These flux ropes moving past the satellite within $1 \sim 3\,s$, which corresponding to diameters of $0.2 \sim 0.6\,R_M$. *DiBraccio et al.* (2015) conducted a detailed statistical survey with about three Earth years of MESSENGER orbit measurements. This survey shows that the average flux rope radius is about 345 km ($0.14\,\mathrm{R_M}$), the core field strength is ~ 40 nT, and the average time duration is about $0.74\,s$. The flux ropes are moving either tailward or planetward. The planetward moving flux ropes are identified by south-then-north B_z variations, and the tailward moving flux ropes are identified by north-then-south B_z

variations. The mean location of the near Mercury neutral line (NMNL) is estimated to be around $-2\,R_M$ based on the distribution of the tailward and planetward flux ropes (*DiBraccio et al.*, 2015). *Sun et al.* (2016) studied the spatial distribution of the flux ropes and the depolarization fronts, and found both of them occur more frequently on the dawnside of the magnetotail. This asymmetry implies that the reconnection prefers to happen on the dawnside, which is opposite to the asymmetry in Earth's tail, where the reconnection signatures are more frequently observed on the duskside (*Walsh et al.*, 2014). The cause of the dawn-dusk asymmetry is still not clear.

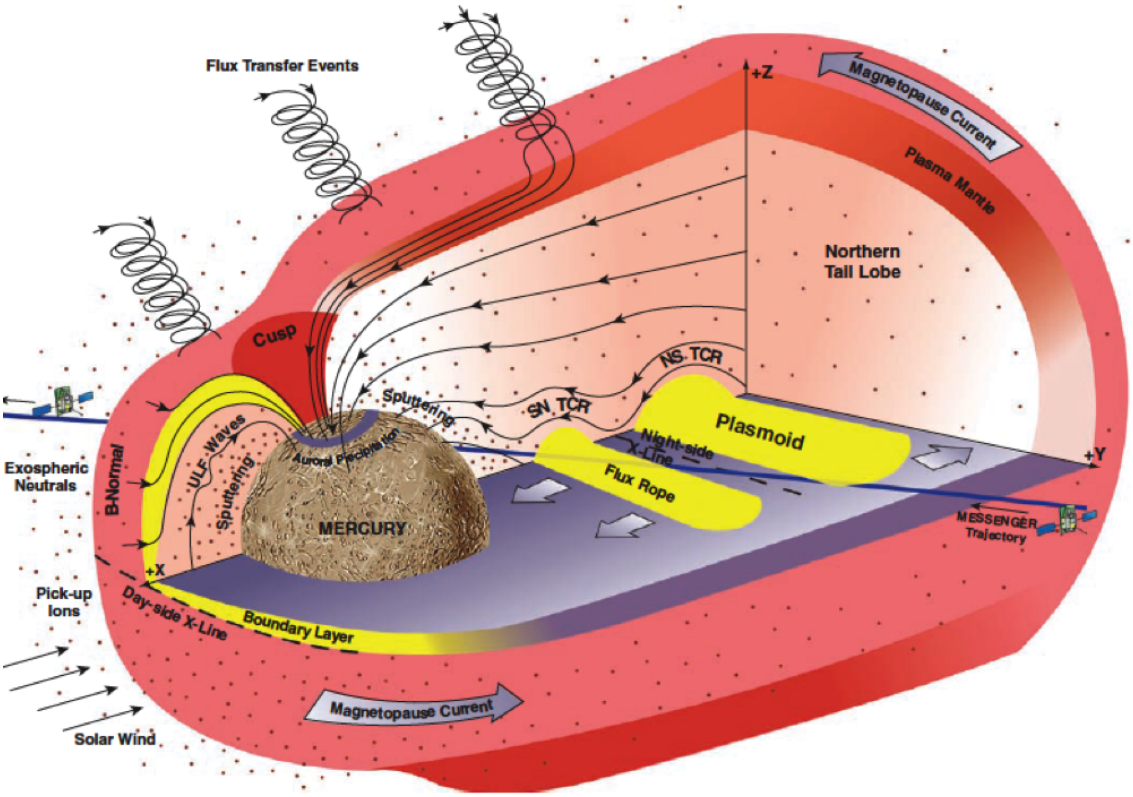

Figure 1.4: The typical structure of Mercury's magnetosphere (from *Slavin et al.* (2009)).

1.2 Numerical Modeling of Magnetosphere

Magnetohydrodynamics (MHD) models have achieved great success to study global structures of magnetospheres, such as the location of the bow shocks and the global response to the solar wind variation. MHD models treat the space plasma as charged fluid flowing in the electromagnetic field. These models solve equations for plasma density, velocity, pressure and the magnetic field. For example, the ideal MHD model treats the plasma as a single fluid and solves the following equations:

$$\frac{\partial \rho}{\partial t} + \nabla \cdot (\rho \mathbf{u}) = 0, \tag{1.1}$$

$$\frac{\partial \rho \mathbf{u}}{\partial t} + \nabla \cdot \left[\rho \mathbf{u}\mathbf{u} + I \left(p + \frac{1}{2\mu_0} B^2 \right) - \frac{1}{\mu_0} \mathbf{B}\mathbf{B} \right] = 0, \tag{1.2}$$

$$\frac{\partial \mathbf{B}}{\partial t} + \nabla \cdot (\mathbf{u}\mathbf{B} - \mathbf{B}\mathbf{u}) = 0, \tag{1.3}$$

$$\frac{\partial e}{\partial t} + \nabla \cdot \left[\mathbf{u} \left(e + p + \frac{1}{2\mu_0} B^2 \right) - \frac{1}{\mu_0} \mathbf{u} \cdot \mathbf{B}\mathbf{B} \right] = 0, \tag{1.4}$$

where ρ, $\mathbf{u}$, p, $\mathbf{B}$ are the plasma mass density, velocity, pressure and magnetic field, respectively, and μ_0 is the magnetic permeability. The total energy density is

$$e = \frac{p}{\gamma - 1} + \frac{\rho u^2}{2} + \frac{B^2}{2\mu_0}, \tag{1.5}$$

where γ is the adiabatic index. The equations above are a set of hyperbolic equations. They can be rewritten in the following form:

$$\frac{\partial \mathbf{U}}{\partial \mathbf{t}} + \nabla \cdot (\mathbf{F}(\mathbf{U})) = 0 \tag{1.6}$$

where

$$\mathbf{U} = \begin{pmatrix} \rho \\ \rho\mathbf{u} \\ \mathbf{B} \\ e \end{pmatrix} \tag{1.7}$$

and

$$\mathbf{F}(\mathbf{U}) = \begin{pmatrix} \rho\mathbf{u} \\ \rho\mathbf{u}\mathbf{u} + I\left(p + \frac{1}{2\mu_0}B^2\right) - \frac{1}{\mu_0}\mathbf{B}\mathbf{B} \\ \mathbf{u}\mathbf{B} - \mathbf{B}\mathbf{u} \\ \mathbf{u}\left(e + p + \frac{1}{2\mu_0}B^2\right) - \frac{1}{\mu_0}\mathbf{u}\cdot\mathbf{B}\mathbf{B} \end{pmatrix}. \tag{1.8}$$

Analytic solutions of the ideal MHD equations can only be found for simple initial conditions and boundary conditions, therefore numerical MHD simulations play an important role in magnetospheric research. Several MHD models have been developed to study the three-dimensional (3D) global structure of the magnetosphere, such as BATS-R-US (*Powell et al.*, 1999; *Tóth et al.*, 2012), LFM (*Lyon et al.*, 2004), OpenGGCM (*Raeder et al.*, 2001) and GUMICS (*Janhunen et al.*, 2012). In order to make the numerical simulations as close to the real magnetosphere as possible, both the numerical accuracy and the physics capability of the MHD models should be improved. Numerical diffusion is the most important factor that controls the numerical accuracy for most MHD solvers. Even though the numerical diffusion is helpful to suppress numerical artifacts, such as overshoots and undershoots near a discontinuity, it can also suppress the development of physical instabilities, for example, the Kelvin-Helmholtz instability (KHI) caused by velocity shear. In order to capture more physics, numerical diffusion should be minimized. High-order accurate methods can help to achieve this goal since they have less numerical diffusion than the lower order schemes. A numerical method is said to be k^{th} order if the error is proportional to the cell size Δx to the power k. The methods of third-order or higher

order accuracy are called high-order methods. More about high-order methods will be discussed later. On the other hand, the scope of applications is limited by the physics capabilities of MHD models. For example, ideal MHD assumes there is no charge separation, pressure is isotropic, and the magnetic field is frozen-in with the ion flow, therefore Langmuir waves, anisotropic pressure, whistler waves would not arise in the ideal MHD model no matter how small the cell size/time step is or how accurate the numerical scheme is. To improve the physics capabilities, various extended MHD models have been developed, such as Hall MHD, multi-species MHD and multi-fluid MHD. But the kinetic physics is still missing in these models. In order to incorporate the kinetic physics into an MHD model, one approach is coupling the MHD model with a kinetic code so that the regions where kinetic effects are important can be correctly handled by the kinetic code. This idea leads to the development of the magnetohydrodynamics with embedded particle-in-cell model (MHD-EPIC) (*Daldorff et al.*, 2014).

To improve both the numerical accuracy and the physics capability of the MHD model BATS-R-US, we developed a fifth-order finite difference method for the MHD equations and coupled BATS-R-US with a PIC code to resolve the kinetic physics. Before discussing these numerical improvements, the MHD model BATS-R-US will be briefly described first.

1.2.1 The BATS-R-US Model

The Block-Adaptive Tree Solarwind Roe-type Upwind Scheme (BATS-R-US) is a flexible, highly modular MHD model that is widely used for space physics research. It is designed to solve a variety of MHD equations, such as ideal MHD, semirelativistic MHD, Hall MHD, multi-species MHD, multi-fluid MHD, etc., on a Cartesian or curvilinear block adaptive grid. The whole computational domain is divided into dozens to thousands of blocks. These blocks can be refined or coarsened according

to regions of interest. Various numerical schemes have been implemented for BATS-R-US. BATS-R-US uses a second order spatial discretization with total variation diminishing (TVD) slope limiters (*Harten*, 1983; *van Leer*, 1979). Various Godunov-type flux functions have been implemented, including the Rusanov (*Rusanov*, 1961), HLLE (*Harten et al.*, 1983), Artificial Wind (*Sokolov et al.*, 2002), HLLD (*Miyoshi and Kusano*, 2005), Roe (*Roe*, 1981) and Godunov (*Godunov et al.*, 1961) fluxes. Various time discretization schemes are also available, such as the explicit, point-implicit, semi-implicit, fully implicit, and part-implicit schemes (*Tóth et al.*, 2012).

1.2.2 High-Order Accurate Methods for Hyperbolic Equations

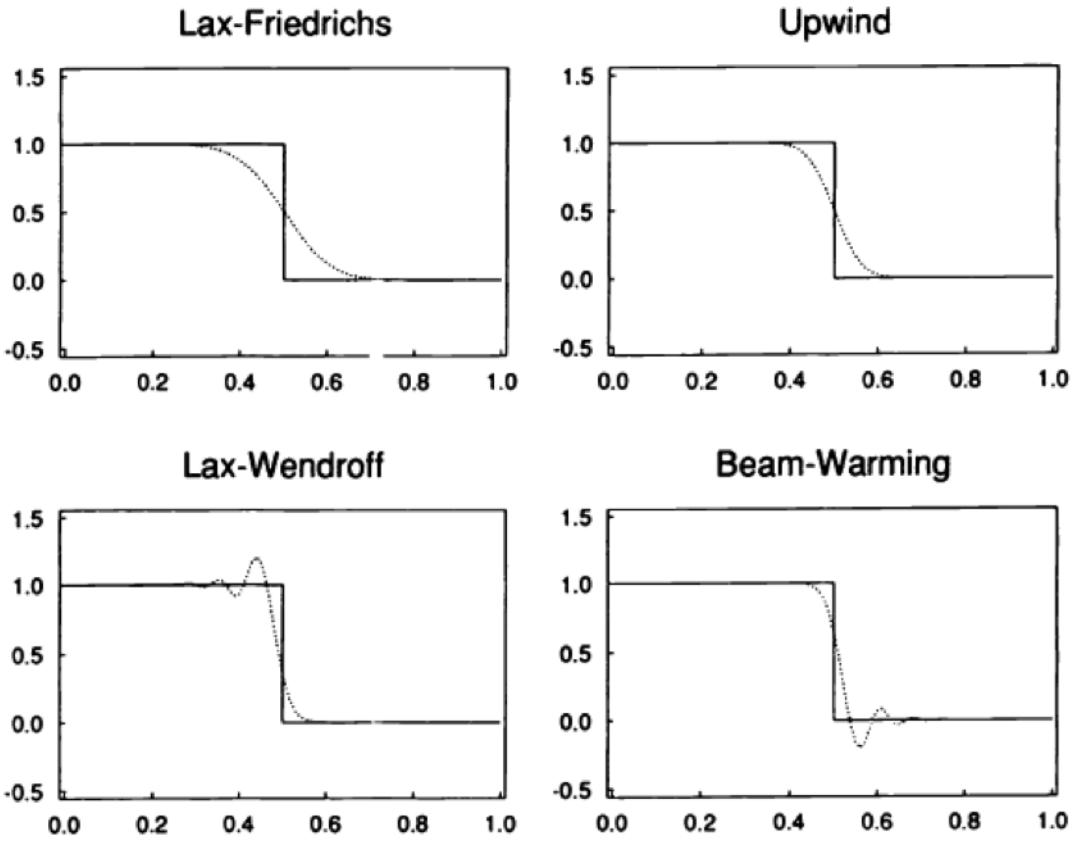

Figure 1.5: Numerical and exact solution to a Riemann problem with different numerical methods (from *LeVeque* (1992)).

Discontinuities are allowed to develop and exist in the solutions of the hyperbolic equations. Inappropriate handling of the discontinuities would cause spurious oscillations in a numerical simulation. Examples are shown in Figure 1.5. These artificial oscillations will finally ruin the simulation results. For a Godunov-type finite volume method, the cell average values are usually stored and calculated at the cell centers. A reconstruction procedure is applied to calculate the face values from the cell averages. Finally a Riemann solver is required to solve the discontinuity problems at the cell faces. The choice of Riemann solver has great impact on the accuracy of the solution, but the reconstruction algorithm determines the order of accuracy. Godunov's theorem predicted that any second or higher order accurate linear schemes would potentially generate new extrema. To break the constraint of Godunov's theorem, Van Leer introduced the Monotonic Upstream-Centered Scheme for Conservation Laws (MUSCL). MUSCL employs flux limiters to limit the linear reconstruction of the face values. The MUSCL scheme is second order in the smooth region since the linear reconstruction produces second order accurate face values.

The second order schemes have achieved great success in the computational fluid dynamics applications. In the past two decades, high-order schemes (third or higher order) have drawn considerable attention due to their potential to minimize the numerical diffusion. A lot of high-order accurate methods have been proposed, such as the discontinuous Galerkin (DG) method, the essentially non-oscillatory (ENO) scheme, the weighted essentially non-oscillatory (WENO) scheme, and the monotonicity-preserving (MP) scheme. High-order schemes usually need more computational resource per stage than the lower order scheme, but they can produce higher quality results for the same grid resolution. Generally high-order schemes can provide more accurate results with the same computational cost. our goal is to develop a high-order accurate scheme for BATS-R-US, which solves a variety of systems of equations. This means that the scheme should not rely on characteristic variables

and the numerical scheme should not require major modifications to become applicable to a new system of equations. In general, we try to keep the algorithm flexbile yet relatively simple to make implementation easier. In summary, we are looking for a scheme with the following properties

- Works on curvilinear block-adaptive grids.
- Oscillation free.
- Obtains correct weak solutions.
- At least 4th-order accurate.
- Requires a small stencil.
- No characteristic decomposition is needed.
- Efficient and simple.

We use the above requirements for selecting the ingredients and design of our high-order scheme.

The discontinuous Galerkin (DG) method is a way to achieve high-order accuracy. Significant progress has been made since it was introduced by *Reed and Hill* (1973) to solve hyperbolic equations, see *Cockburn and Shu* (1998, 2001). DG offers flexibility to achieve high-order accuracy and can be easily extended to complicated geometries, but it is significantly more complicated than the finite volume (FV) and finite difference (FD) schemes.

High-order finite volume (FV) and finite difference (FD) methods have been extensively explored. Harten designed the essentially non-oscillatory (ENO) scheme (*Harten et al.*, 1987) with 3rd and higher order accuracy, Liu et al. presented the weighted essentially non-oscillatory (WENO) scheme (*Liu et al.*, 1994) with similar high-order accuracy. Unfortunately, most ENO and WENO schemes require characteristic decomposition to work well for systems of equations (*Shu*, 2009; *Qiu and*

Shu, 2002). The central WENO (CWENO) scheme by *Capdeville* (2008) is an exception, as it works well without characteristic variables, and we have implemented CWENO as a possible option. An alternative to the ENO/WENO/CWENO type limiters is the monotonicity-preserving (MP) limiter developed by *Suresh and Huynh* (1997). MP schemes have been applied to turbulent simulation by *Li and Jaberi* (2012), to astrophysics by *Porth et al.* (2014); *Mignone et al.* (2010) and *Del Zanna et al.* (2007). It is also combined with WENO as an extra limiter by *Balsara and Shu* (2000). The MP schemes are considerably simpler and computationally less expensive than WENO type schemes, and work well without characteristic decomposition. Comparisons by *Li and Jaberi* (2012) showed that the MP scheme is competitive with WENO schemes, and our experience also showed that the fifth order MP5 limiter works as well or better than the 5th order CWENO scheme. We will therefore use the MP5 limiter as the first ingredient of our scheme. A small modification is introduced to better maintain positivity of density, pressure etc.

All the schemes described above are finite volume (FV) methods in their originally published form. They construct face values based on cell-averages. The FV approach makes conservation of variables straightforward, which is important for obtaining correct weak solutions. However, the finite volume approach becomes complicated for two (2D) or three dimensional (3D) simulations, because the face fluxes have to be integrated over the cell faces with high-order accuracy. Source terms also have to be integrated in the control volume with a Gaussian quadrature that further increases computational cost. In addition, constructing proper control volumes for dynamically adaptive non-Cartesian grids is very complicated.

The finite difference (FD) approach is based on cell point values and it approximates spatial derivatives for each dimension independently, so it can be easily and inexpensively extended to 2D and 3D. Source terms can be simply evaluated in the cell centers. Curvilinear grids can be relatively easily accommodated by transforming

the governing equations and discretizing them with the same FD method in the generalized coordinates. High-order accuracy can be achieved as long as the coordinate transformation is smooth. Conservative properties can be ensured if the FD scheme is written in a flux difference form and the same face fluxes are used to update the values of neighboring cell centers. This is, unfortunately, not easy to achieve at grid resolution changes of an adaptive grid beyond second-order accuracy. In practice, however, the FD scheme can work well even if the conservation properties are not exact at grid resolution changes. We will demonstrate this through several numerical tests.

Following the finite difference approach, *Shu and Osher* (1988, 1989) introduced the finite difference ENO, and *Jiang and Shu* (1996) developed the finite difference WENO schemes. These finite difference methods directly construct face fluxes from cell center fluxes (FD-Flux). The fluxes of the characteristic variables are used by *Shu* (2009); *Li and Jaberi* (2012); *Mignone et al.* (2007), but this approach is very expensive and requires the construction of Roe-matrices that we wish to avoid. The alternative approach is to use the original fluxes with global Lax-Friedrichs scheme (*Shu*, 2009; *Porth et al.*, 2014), which we tried and found to be quite diffusive despite the formally high-order accuracy. *Del Zanna et al.* (2003, 2007) suggested an alternative way to design the high-order finite difference scheme: first construct high-order accurate but properly limited left and right face values of the primitive variables (FD-Primitive), calculate the corresponding face fluxes with an arbitrary approximate Riemann solver and then calculate a high-order spatial derivative using up to 6 face fluxes. This last step can also be regarded as a 'correction' of the face fluxes to ensure that spatial derivatives achieve high order accuracy. This scheme turns out to be the same as one of the explicit weighted compact nonlinear schemes (WCNS) introduced by *Deng and Zhang* (2000). We chose this FD-Primitive approach, but we modified the flux correction step to maintain the same stencil as the MP5 limiter

uses. This is an important improvement, because it allows smaller grid blocks with fewer ghost cells and more flexible grid adaptation.

Generalizing the high-order FD scheme to curvilinear grids is relatively straightforward, but satisfying free-stream preservation is still a challenge. The geometric coefficients, which relate the curvilinear mesh to a computational Cartesian mesh, are involved in the spatial derivatives of numerical fluxes and generate numerical errors. If these numerical errors do not cancel each other for a uniform flow, the errors may accumulate and become non-ignorable, see *Visbal and Gaitonde* (2002) and *Nonomura et al.* (2010). *Thomas and Lombard* (1979) proposed that evaluating both geometric coefficients and convection terms with the same interpolation formula ensures the numerical errors exactly cancel each other and leads to a free-stream preserving solution. *Deng et al.* (2011) carefully analyzed how the cancellation works. We adapt this approach to our particular FD-Primitive discretization with the flux correction.

The final step is to combine the high-order FD scheme with daptive mesh refinement (AMR). This technique was introduced by *Berger and Colella* (1989) to capture local details in a computationally efficient manner. Cell based grid adaptation is very difficult to combine with high-order finite difference schemes, but block and patch based AMR is doable. There has been significant progress to combine high-order schemes and AMR in recent years. *McCorquodale and Colella* (2011) implemented a fourth-order finite volume method combined with AMR, where they fill in the ghost cells by solving a linear least square problem. *Shen et al.* (2011) developed the high-order FD-Flux type AMR-WENO scheme, in which they used an odd refinement ratio to simplify the prolongation and restriction operations. The ADER (Arbitrary Derivative Riemann Problem) scheme, which only needs one-step temporal update, is advantageous to AMR meshes, and the finite volume ADER-WENO AMR scheme has been explored by *Balsara et al.* (2009) and *Dumbser et al.* (2013). We

implement the high-order MP5 finite difference scheme (*Chen et al.*, 2016) into the Block-Adaptive Tree Library (BATL) (*Tóth et al.*, 2012) which uses the usual factor of 2 refinement ratio. Thanks to the careful design of the finite difference algorithm, only three ghost cells are required for the grid blocks. We use a high-order accurate interpolation method to fill in the ghost cells. For sake of efficiency, the interpolation is done along carefully selected 1D stencils, so there is no need to solve for general multi-dimensional interpolation. The interpolations all employ a new general limiter that is based on the principles of the MP limiter, so that there are no spurious oscillations at resolution changes but the high-order accuracy is still maintained.

1.2.3 Magnetohydrodynamics with Embedded Particle-in-Cell (MHD-EPIC) Model

MHD models are quite efficient for 3D global magnetospheric simulations, but the physics capability of these models is limited by the assumptions underlying the MHD equations. Kinetic physics, which goes beyond the Maxwellian particle distribution, is missing in the MHD models, thus MHD models cannot correctly handle the kinetic processes, like magnetic reconnection. On the other hand, particle-in-cell (PIC) methods have been demonstrated as a powerful tool to study kinetic physics. But the PIC codes are so computationally expensive that it is still extremely difficult to do global simulations (*Lapenta*, 2012; *Peng et al.*, 2015). The MHD-EPIC model was developed to combine the efficiency of the MHD model and the physics capability of the PIC code (*Daldorff et al.*, 2014).

1.2.3.1 Particle-in-Cell Method

The collisionless plasma can be described by the Vlasov-Maxwell system. The Vlasov equation is:

$$\frac{\partial f_s}{\partial t} + \mathbf{v} \cdot \frac{\partial f_s}{\partial \mathbf{x}} + \frac{q_s}{m_s} (\mathbf{E} + \mathbf{v} \times \mathbf{B}) \frac{\partial f_s}{\partial \mathbf{v}} = 0, \tag{1.9}$$

where $f_s(\mathbf{x}, \mathbf{v}, t)$ describes the phase space density of particles of species s with velocity $\mathbf{v}$ near the location $\mathbf{x}$; q_s and m_s are the particle charge and mass, respectively; $\mathbf{E}$ and $\mathbf{B}$ are the electric and magnetic fields. This equation is closed by coupling with Maxwell equations:

$$\nabla \cdot \mathbf{E} = \frac{\rho_q}{\epsilon_0}, \tag{1.10}$$

$$\nabla \cdot \mathbf{B} = 0, \tag{1.11}$$

$$\frac{\partial \mathbf{B}}{\partial t} = -\nabla \times \mathbf{E}, \tag{1.12}$$

$$\frac{1}{c^2} \frac{\partial \mathbf{E}}{\partial t} = \nabla \times \mathbf{B} - \mu_0 \mathbf{j}, \tag{1.13}$$

where ρ_q is the net charge density; the constants ϵ_0, μ_0 and c are the electric permittivity, magnetic permeability and speed of light, respectively. The particle-in-cell (PIC) method is a class of methods solving the Vlasov equation by sampling the phase space distribution with macro-particles. A macro-particle is a computational particle representing many physical particles that are close to each other in the phase space. Most particle-in-cell codes assume the macro-particles have certain shape in space in order to reduce the numerical collisions *Dawson* (1983); *Birdsall and Langdon* (2004). The cloud-in-cell scheme, which represents a macro-particle with a flat-top function, is widely used. The motion of the macro-particles is controlled by the electromagnetic

field:

$$\frac{d\mathbf{x}_p}{dt} = \mathbf{v}_p, \tag{1.14}$$

$$\frac{d\mathbf{v}_p}{dt} = \frac{q_s}{m_s}\left(\mathbf{E}_p + \mathbf{v}_p \times \mathbf{B}_p\right), \tag{1.15}$$

where $\mathbf{x}_p$ and $\mathbf{v}_p$ are the center position and velocity of a macro-particle; $\mathbf{E}_p$ and $\mathbf{B}_p$ are the electric field and magnetic field exerting at the macro-particle. Particle-in-cell methods trace the trajectories of the macro-particles in the electromagnetic field by solving Eq. (1.14)-(1.15). The Maxwell equations (Eq. (1.10)-(1.13)) are solved on a Cartesian grid . The charge density and the currents are interpolated from the macro-particles to the grid.

Discretization errors are present in all numerical models. In addition to the usual spatial and temporal truncation errors, the PIC codes also suffer from statistical errors because randomly chosen macro-particles are used to represent the phase space distribution $f_s(\mathbf{x}, \mathbf{v}, t)$. The statistical noise is proportional to $\frac{1}{\sqrt{N}}$, where N is the number of macro-particles in one cell. In order to suppress this noise, dozens to thousands of macro-particles per cell are used in the simulations, therefore billions or trillions of macro-particles are usually needed for a 3D or even 2D local simulation. The numerous macro-particles pose a challenge for computational efficiency.

Most PIC codes solve the equations with an explicit time discretization scheme, for instance, the leap-frog algorithm is widely used. These explicit PIC codes need to resolve the Debye length to avoid finite grid instability, and the time step is limited by the plasma frequency and also the speed of light (*Birdsall and Langdon*, 2004; *Dawson*, 1983; *Lapenta*, 2012). To relax the stability constraints, implicit particle methods, which solve the equations with implicit schemes, have been considered for decades (*Mason*, 1981; *Brackbill and Forslund*, 1982; *Markidis et al.*, 2010). The implicit code is linearly unconditionally stable and larger cell size and time step can

be used compared with explicit PIC methods. In the MHD-EPIC model, the implicit code iPIC3D, which is developed by *Markidis et al.* (2010), is coupled with the MHD model BATS-R-US to combine the advantages of kinetic models and MHD models.

1.2.3.2 The Two-Way Coupling of an MHD Model with a PIC Code

BATS-R-US and iPIC3D are coupled through the Space Weather Modeling Framework (SWMF) (*Tóth et al.*, 2012). These two models are compiled together to generate a single executable file. Both models can run simultaneously on specified processors and the information exchange is efficiently handled by the Message Passing Interface (MPI).

The flow of the coupling between BATS-R-US and iPIC3D is shown in Figure 1.6. At the beginning of the coupling, BATS-R-US sends the information, including density, velocity, pressure and magnetic field, to iPIC3D. iPIC3D initializes the electric field based on Ohm's law. Macro-particles are generated with Maxwellian distribution according to the fluid information so that iPIC3D and BATS-R-US have consistent density, velocity and pressure at the same position. After the PIC initialization, the MHD and PIC models update independently with their own time steps. The coupling frequency between these two models can be set to a value that is independent of the MHD or PIC time step. During the coupling, iPIC3D calculates moments of the particle distribution function, such as the density, velocity and pressure, and overwrites the MHD cells overlapped with the PIC region. In return the MHD model provides electromagnetic field as well as particle boundary conditions for iPIC3D. For the particle boundary, iPIC3D removes the particles in the boundary cells, and re-generates new particles based on the fluid variables obtained from MHD. Between the two coupling time points, iPIC3D uses the latest information obtained from BATS-R-US as boundary conditions during each iteration.

BATS-R-US uses Cartesian or curvilinear adaptive grids, and iPIC3D always uses

2D or 3D uniform Cartesian mesh. Figure 1.7 shows an example of the spatial discretization of the MHD-EPIC model in 2D, where BATS-R-US uses a cylindrical grid. The electric field at the boundary nodes with $i_n = 0$ or $j_n = 0$ is fixed with values obtained from MHD as the boundary condition for iPIC3D. Similarly, the magnetic field at the boundary cells with $i_c = 0$ or $j_c = 0$ is also obtained from MHD. The plasma density, velocity and pressure at the nodes with $i_c = 0, 1$ and $j_c = 0, 1$ are also obtained from MHD, and the ghost particles (small red dots in Figure 1.7) are re-generated based on these fluid values. More details about the coupling algorithm can be found in *Daldorff et al.* (2014). In the recent two years, we have improved the performance and capability of the MHD-EPIC model:

- The PIC part becomes about twice faster after coupling with the latest iPIC3D, which optimized the particle mover and the message exchange between processors.
- An adaptive time stepping algorithm is implemented to automatically control the iPIC3D time step.
- The coupling process is also optimized by reducing the unnecessary information exchange between BATS-R-US and iPIC3D.
- The multi-species MHD, multi-fluid MHD and the MHD models with separate electron pressure equation are coupled with iPIC3D.
- Grid alignment is not required anymore.
- Multiple PIC boxes can be used in one computational domain.

1.3 Overview of the Dissertation

This dissertation includes the development of the high-order scheme for BATS-R-S, and the magnetospheric simulations using the MHD-EPIC model. The fifth-order

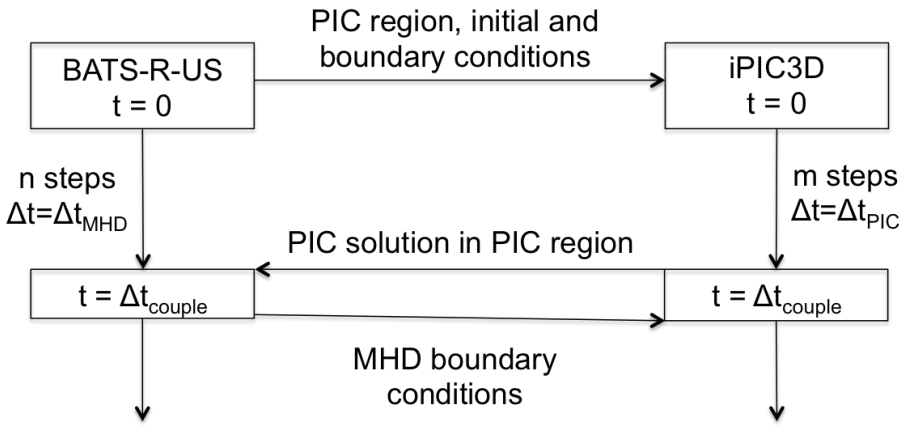

Figure 1.6: The flow of the coupling algorithm.

finite difference scheme is introduced in chapter II. This section starts with describing the high-order scheme on uniform Cartesian grid. How the high-order accuracy is achieved on block-adaptive curvilinear mesh is also discussed. Various numerical tests are provided to demonstrate the accuracy and capability of the fifth-order scheme. Chapter III presents the 3D MHD-EPIC simulation of Earth's magnetosphere. The PIC box is placed on the dayside magnetopause to study the dayside reconnection. The formation and evolution of the flux transfer events (FTEs) is discussed. The kinetic features found from the simulation, such as the crescent electron phase space distribution, the Larmor electric field and the lower hybrid drift instability (LHDI), are also presented. Chapter IV discusses Mercury's tail dynamics studied with the MHD-EPIC model. The simulation results regarding the magnetotail reconnection, flux ropes and the dawn-dusk asymmetry are discussed.

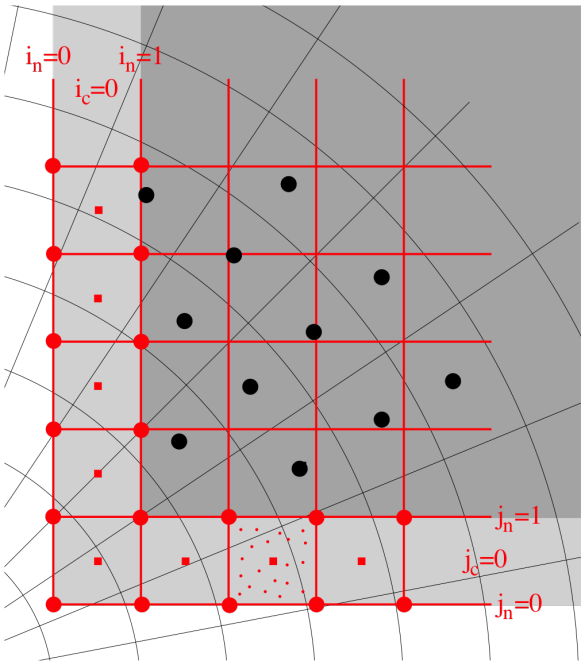

Figure 1.7: Spatial discretization of the MHD-EPIC model. The curvilinear black mesh represents the MHD mesh. The black circles represent the MHD cell centers. The red lines are the iPIC3D grids. The red dots are the PIC nodes and the red squares are the PIC cell centers. The dark gray region is the PIC domain and the light region is the PIC ghost cells. The small red dots represent the macro-particles.

CHAPTER II

A Fifth-Order Finite Difference Scheme for Hyperbolic Equations on Block-Adaptive Curvilinear Grids

Minimizing numerical diffusion is an important approach to improve numerical accuracy and capture more physics. The most straightforward way is refining the grid, which is easy to implement but computationally expensive. Without increasing computational cost significantly, high order numerical schemes, adaptive mesh refinement and curvilinear grids can all improve accuracy relative to low-order schemes employed on uniform Cartesian meshes. Combining the benefits of these approaches can further enhance the accuracy of the code, but it also leads to new challenges. High order schemes are easiest to realize on uniform grids, while adaptive mesh refinement creates non-uniform stencils. Block and patch based adaptive grids have locally uniform grids that can be large enough to cover stencils required by the high-order scheme, but grid resolution changes still pose a problem. Curvilinear grids also introduce additional complexity both for adaptive mesh refinement and for maintaining high order accuracy. This chapter will discuss how we handle these challenges and design a high order accurate method on a block-adaptive curvilinear mesh.

2.1 Fifth-Order Finite Difference Scheme on a Uniform Cartesian Grid

2.1.1 Governing Equations

We begin to describe the method for a 1D hyperbolic system:

$$\frac{\partial \mathbf{U}}{\partial t} + \frac{\partial \mathbf{F}(\mathbf{U})}{\partial x} = 0 \tag{2.1}$$

where $\mathbf{U}$ is the vector of conservative variables and $\mathbf{F}$ are the fluxes. In the following part, we will also use primitive variables $\mathbf{W}$. For example, in the case of 1D Euler equations, $\mathbf{U} = (\rho, \rho u, \rho E)$ and $\mathbf{W} = (\rho, u, p)$.

We discretize the equation in a semi-discrete form:

$$\frac{\partial \mathbf{U}_i}{\partial t} + \frac{1}{\Delta x}(\hat{\mathbf{F}}_{i+1/2} - \hat{\mathbf{F}}_{i-1/2}) = 0 \tag{2.2}$$

where $\hat{\mathbf{F}}_{i+1/2} = \hat{\mathbf{F}}(\mathbf{U}_{i-l}, \cdots, \mathbf{U}_{i+r})$ is the numerical flux at $x_{i+1/2}$, the middle point between x_i and x_{i+1}, and the stencil extends from $i-l$ to $i+r$. The goal is to find appropriate values of $\hat{\mathbf{F}}_{i+1/2}$ and $\hat{\mathbf{F}}_{i-1/2}$ so that the the spatial difference in (2.2) is high order accurate. A Runge-Kutta solver can be applied to the time integration. In this chapter, we use superscript '*' to represent the exact solution. For example, $\mathbf{U}_i^{*n}$ is the exact conservative values at x_i and t_n.

2.1.2 Fifth-Order Spatial Derivative

We use the primitive variables $\mathbf{W}$ instead of conservative variables $\mathbf{U}$ or characteristic variables for face value interpolation. Interpolation based on primitive variables is simpler and more efficient compared to characteristic variables, and it is easier to keep density and pressure positive.

First, we calculate fifth-order accurate face primitive values $\mathbf{W}_{i+1/2}^L$ and $\mathbf{W}_{i+1/2}^R$

from the cell center values:

$$\mathbf{W}^L_{i+1/2} = (3\mathbf{W}_{i-2} - 20\mathbf{W}_{i-1} + 90\mathbf{W}_i + 60\mathbf{W}_{i+1} - 5\mathbf{W}_{i+2})/128 \tag{2.3}$$

$$\mathbf{W}^R_{i+1/2} = (3\mathbf{W}_{i+3} - 20\mathbf{W}_{i+2} + 90\mathbf{W}_{i+1} + 60\mathbf{W}_i - 5\mathbf{W}_{i-1})/128 \tag{2.4}$$

The MP5 limiter (*Suresh and Huynh*, 1997) is used to suppress the unphysical oscillations for the interpolations above. The limited face values are fifth-order accurate in smooth regions. Three nearby cells at each side are needed for this face value reconstruction, so three ghost cell layers are required for each block in each direction. Then, any approximate Riemann solver, like Roe solver, HLL type solver, Lax-Friedrichs solver, etc., can be employed to calculate face flux $\mathbf{F}_{i+1/2}$ from $\mathbf{U}^L_{i+1/2}$ and $\mathbf{U}^R_{i+1/2}$. $\mathbf{F}_{i+1/2}$ is a fifth-order accurate approximation to $\mathbf{F}^*_{i+1/2}$. Based on $\mathbf{F}_{i+1/2}$, we can find the numerical fluxes $\hat{\mathbf{F}}_{i+1/2}$ for high-order spatial derivative:

$$\hat{\mathbf{F}}_{i+1/2} = \mathbf{F}_{i+1/2} - \Delta^{(2)}\mathbf{F}_{i+1/2} + \Delta^{(4)}\mathbf{F}_{i+1/2} \tag{2.5}$$

where,

$$\begin{aligned} \Delta^{(2)}\mathbf{F}_{i+1/2} &= \frac{1}{6}(\mathbf{F}_i - 2\mathbf{F}_{i+1/2} + \mathbf{F}_{i+1}) \\ \Delta^{(4)}\mathbf{F}_{i+1/2} &= \frac{1}{180}(\mathbf{F}_{i-1} - 9\mathbf{F}_i + 16\mathbf{F}_{i+1/2} - 9\mathbf{F}_{i+1} + \mathbf{F}_{i+2}) \end{aligned} \tag{2.6}$$

The flux correction terms $\Delta^{(2)}\mathbf{F}_{i+1/2}$ and $\Delta^{(4)}\mathbf{F}_{i+1/2}$ are proportional to the second and fourth spatial derivatives of $\mathbf{F}$ at $x_{i+1/2}$, respectively. For flux correction, *Del Zanna et al.* (2007) used face fluxes, *Nonomura et al.* (2010) employed a combination of face fluxes and cell centered fluxes to improve the robustness of their scheme, while we only use cell centered physical fluxes to make the stencil smaller. The original MP scheme introduced by *Suresh and Huynh* (1997) is monotonicity-preserving for linear problems, however, we corrected the face fluxes in (2.5) without limiting and the

correction will destroy the monotonicity-preserving property. Near discontinuities, some oscillations are expected, but in practice, as shown by the numerical tests, the oscillations are small, because the correction terms have small coefficients (2.6). A limiter could be introduced to suppress the oscillations in the future.

Substituting $\hat{\mathbf{F}}_{i+1/2}$ and $\hat{\mathbf{F}}_{i-1/2}$ into (2.2), a fifth-order accurate spatial derivative is obtained. To simplify the notation, let operator $\mathcal{D}$ represent the spatial derivative calculation (2.2) as a function of the face centered and cell centered fluxes:

$$\left.\frac{\Delta \mathbf{F}}{\Delta x}\right|_{x_i} = \frac{\hat{\mathbf{F}}_{i+1/2} - \hat{\mathbf{F}}_{i-1/2}}{\Delta x} = \mathcal{D}(\mathbf{F}_{i-2}, \mathbf{F}_{i-1}, \mathbf{F}_{i-1/2}, \mathbf{F}_{i+1/2}, \mathbf{F}_{i+1}, \mathbf{F}_{i+2}) \tag{2.7}$$

Operator $\mathcal{D}$ will also be used to calculate geometric coefficients of the curvilinear mesh in section 3.

The scheme described above needs three ghost cell layers on each side, which is reasonable compared to the TVD schemes, which need two layers.

2.1.3 Error Analysis for Uniform Grids

There are some subtle details related to the errors. Using the linear advection with velocity +1 as an example, so that $\mathbf{F} = \mathbf{U} = \mathbf{W}$, then $\mathbf{F}_{i+1/2} = \mathbf{W}^L_{i+1/2}$ if an upwind scheme is used. The face flux $\mathbf{F}_{i+1/2}$ is a fifth-order approximation to $\mathbf{F}^*_{i+1/2}$, but it is divided by Δx in (2.7), so it is not obvious if the scheme is indeed fifth-order accurate. From (2.3), we have:

$$\begin{aligned}
\mathbf{F}_{i+1/2} &= \mathbf{F}^*_{i+1/2} - \frac{3}{256}\Delta x^5 \left.\frac{\partial^5 \mathbf{F}^*}{\partial x^5}\right|_{x_{i+1/2}} + O(\Delta x^6) \\
\mathbf{F}_{i-1/2} &= \mathbf{F}^*_{i-1/2} - \frac{3}{256}\Delta x^5 \left.\frac{\partial^5 \mathbf{F}^*}{\partial x^5}\right|_{x_{i-1/2}} + O(\Delta x^6)
\end{aligned} \tag{2.8}$$

so in the finite difference formula

$$\begin{aligned}\frac{\mathbf{F}_{i+1/2}-\mathbf{F}_{i-1/2}}{\Delta x} &= \frac{\mathbf{F}^*_{i+1/2}-\mathbf{F}^*_{i-1/2}+O(\Delta x^6)}{\Delta x} \\ &= \frac{\mathbf{F}^*_{i+1/2}-\mathbf{F}^*_{i-1/2}}{\Delta x}+O(\Delta x^5)\end{aligned} \tag{2.9}$$

the leading error terms cancel if $\frac{\partial^5 \mathbf{F}^*}{\partial x^5}$ is continuous. The equation above is only a second-order approximation to $\frac{\partial \mathbf{F}^*}{\partial x}\big|_{x_i}$ since

$$\frac{\mathbf{F}_{i+1/2}-\mathbf{F}_{i-1/2}}{\Delta x} = \left.\frac{\partial \mathbf{F}^*}{\partial x}\right|_{x_i} + \frac{\Delta x^2}{24}\cdot\left.\frac{\partial^3 \mathbf{F}^*}{\partial x^3}\right|_{x_i} + \frac{\Delta x^4}{1920}\cdot\left.\frac{\partial^5 \mathbf{F}^*}{\partial x^5}\right|_{x_i} + O(\Delta x^5) \tag{2.10}$$

where $\frac{\partial \mathbf{F}^*}{\partial x}\big|_{x_i}$, $\left.\frac{\partial^3 \mathbf{F}^*}{\partial x^3}\right|_{x_i}$ and $\left.\frac{\partial^5 \mathbf{F}^*}{\partial x^5}\right|_{x_i}$ are the analytic derivatives at x_i. To eliminate the $O(\Delta x^2)$ and $O(\Delta x^4)$ terms, the flux correction (2.5) is necessary.

2.2 Free-Stream Preservation

In 3D, the hyperbolic system in conservative form is:

$$\frac{\partial \mathbf{U}}{\partial t}+\frac{\partial \mathbf{F}}{\partial x}+\frac{\partial \mathbf{G}}{\partial y}+\frac{\partial \mathbf{H}}{\partial z}=0 \tag{2.11}$$

On curvilinear grids using generalized coordinates ξ, η and ζ, this hyperbolic system can be transformed into

$$\frac{\partial \tilde{\mathbf{U}}}{\partial t}+\frac{\partial \tilde{\mathbf{F}}}{\partial \xi}+\frac{\partial \tilde{\mathbf{G}}}{\partial \eta}+\frac{\partial \tilde{\mathbf{H}}}{\partial \zeta}=0 \tag{2.12}$$

where

$$\begin{aligned}
\tilde{\mathbf{U}} &= \mathbf{U}/J \\
\tilde{\mathbf{F}} &= \tilde{\xi}_x\mathbf{F} + \tilde{\xi}_y\mathbf{G} + \tilde{\xi}_z\mathbf{H} \\
\tilde{\mathbf{G}} &= \tilde{\eta}_x\mathbf{F} + \tilde{\eta}_y\mathbf{G} + \tilde{\eta}_z\mathbf{H} \\
\tilde{\mathbf{H}} &= \tilde{\zeta}_x\mathbf{F} + \tilde{\zeta}_y\mathbf{G} + \tilde{\zeta}_z\mathbf{H}
\end{aligned} \tag{2.13}$$

and the subscripts indicate partial derivatives. The inverse Jacobian J^{-1} is:

$$J^{-1} = \left|\frac{\partial(x,y,z)}{\partial(\xi,\eta,\zeta)}\right| \tag{2.14}$$

and $\tilde{\xi}_x ... \tilde{\zeta}_z$ are the transformation metrics, for example, $\tilde{\xi}_x = \xi_x/J = y_\eta z_\zeta - y_\zeta z_\eta$. Physically, $\mathbf{F}$ is the flux along the x direction, and $\tilde{\xi}_x$ projects $\mathbf{F}$ to $\tilde{\mathbf{F}}$, which is the flux along the ξ direction. The meaning of $\tilde{\mathbf{G}}$ and $\tilde{\mathbf{H}}$ are analogous. The inverse Jacobian $1/J$ is related to the volume of the cell of the finite volume method.

At the generalized coordinates (ξ_i, η_j, ζ_k), the cell center primitive values $\mathbf{W}_{i,j,k}$ are known at each time step. Applying (2.3) and (2.4) to each variable in each direction, we can obtain the face values, for example $\mathbf{W}^{L,R}_{i+1/2,j,k}$. Then an approximate Riemann solver can obtain the face fluxes $\mathbf{F}$, $\mathbf{G}$ and $\mathbf{H}$. The cell center fluxes are obtained from $\mathbf{W}_{i,j,k}$. Using the metrics $\tilde{\xi}_x ... \tilde{\zeta}_z$ at both cell centers and cell faces, the fluxes $\tilde{\mathbf{F}}$, $\tilde{\mathbf{G}}$ and $\tilde{\mathbf{H}}$ at the cell centers and faces are obtained from (2.13). Then spatial derivatives in (2.12) can be calculated through operator $\mathcal{D}$.

Free-streaming preservation requires that a constant state with a constant flow is maintained with round-off errors only. Let us take an initial condition with all the variables $\mathbf{W}$ and fluxes $\mathbf{F}$, $\mathbf{G}$, $\mathbf{H}$ uniform in physical space. Therefore, the spatial derivatives in (2.12) reduce to the numerical spatial derivatives of geometric coefficients $\tilde{\xi}_x ... \tilde{\zeta}_z$. Analytically, the sum of spatial derivatives in (2.12) should be zero. However, this is not ensured by numerical differences unless some special techniques

are used. To keep free-stream preserving, the metrics in (2.13) should be calculated numerically with the following conservative form (*Thomas and Lombard*, 1979):

$$\begin{aligned}
\tilde{\xi}_x &= (y_\eta z)_\zeta - (y_\zeta z)_\eta, \quad \tilde{\xi}_y = (z_\eta x)_\zeta - (z_\zeta x)_\eta, \quad \tilde{\xi}_z = (x_\eta y)_\zeta - (x_\zeta y)_\eta \\
\tilde{\eta}_x &= (y_\zeta z)_\xi - (y_\xi z)_\zeta, \quad \tilde{\eta}_y = (z_\zeta x)_\xi - (z_\xi x)_\zeta, \quad \tilde{\eta}_z = (x_\zeta y)_\xi - (x_\xi y)_\zeta \\
\tilde{\zeta}_x &= (y_\xi z)_\eta - (y_\eta z)_\xi, \quad \tilde{\zeta}_y = (z_\xi x)_\eta - (z_\eta x)_\xi, \quad \tilde{\zeta}_z = (x_\xi y)_\eta - (x_\eta y)_\xi
\end{aligned} \tag{2.15}$$

All derivatives in the expressions above should be calculated in the same way and with at least fifth-order accuracy. We describe the numerical calculation of y_η at cell center (ξ_i, η_j, ζ_k) as an example. Similar to the discretization of $\frac{\partial \mathbf{F}}{\partial x}$ in (2.7), we calculate the face value first. Let us denote the interpolation from the cell center values to a face value as $\mathcal{F}$ defined as

$$\begin{aligned}
y_{i+1/2} &= \mathcal{F}(y_{i-2}, y_{i-1}, y_i, y_{i+1}, y_{i+2}, y_{i+3}) \\
&= \frac{3}{256}(y_{i-2} + y_{i+3}) - \frac{25}{256}(y_{i-1} + y_{i+2}) + \frac{150}{256}(y_i + y_{i+1})
\end{aligned} \tag{2.16}$$

where we only kept subscript i and omitted j and k for sake of simplicity. We use the same formula for $y_{i-1/2}$, then the numerical y_η at cell center (ξ_i, η_j, ζ_k) is obtained as

$$\left.\frac{\Delta y}{\Delta \eta}\right|_{\xi_i} = \mathcal{D}(y_{i-2}, y_{i-1}, y_{i-1/2}, y_{i+1/2}, y_{i+1}, y_{i+2}) \tag{2.17}$$

Applying (2.16) and (2.17) to all the derivatives in (2.15) gives the cell center numerical coefficients $\tilde{\xi}_x ... \tilde{\zeta}_z$, whose cell face values can also be obtained with the interpolation formula $\mathcal{F}$ (2.16).

The key to reach a free-stream preserving solution is using operator $\mathcal{D}$ for both flux correction (2.5) and geometric coefficient calculation (2.17), and all the face metrics should be interpolated with the same formula $\mathcal{F}$ (2.16), but it is not necessary to use the same formula as for the face primitive calculation (see (2.3), (2.4)), where the MP5 limiter is applied. Here we illustrate the statements above in an intuitive

way, for more details, we refer to *Thomas and Lombard* (1979); *Visbal and Gaitonde* (2002); *Jiang et al.* (2013). Assume only flux $\mathbf{F}$ is non-zero and uniform in space, then (2.12) reduces to:

$$\tilde{\mathbf{U}}_t + \mu \mathbf{F} = 0 \tag{2.18}$$

where

$$\mu = (\tilde{\xi}_x)_\xi + (\tilde{\eta}_x)_\eta + (\tilde{\zeta}_x)_\zeta \tag{2.19}$$

Here $(\tilde{\xi}_x)_\xi$ results from the derivative of $\tilde{\mathbf{F}}$ in the ξ direction that is discretized with the $\mathcal{D}$ operator. The $\tilde{\xi}_x$ term itself depends on derivatives in the η and ζ directions (see (2.15)) and these should also be calculated with the same formula so that the spatial derivative calculation is symmetric. That is why (2.17) should also use operator $\mathcal{D}$ just as (2.7), and all the face geometric coefficients should be calculated using the same operator $\mathcal{F}$. Similar considerations apply to $(\tilde{\eta}_x)_\eta$ and $(\tilde{\zeta}_x)_\zeta$. All the three derivatives in μ involve the same grid points in three dimensions because of symmetry, and numerical errors introduced by each derivative can cancel each other to make sure that μ is zero up to rounding error. If a limiter was used in the flux correction in (2.5), it should be designed carefully so that it does not modify the interpolation and difference formulas under free-streaming conditions (uniform $\mathbf{F}$, $\mathbf{G}$ and $\mathbf{H}$).

2.3 High-Order Scheme for AMR Grid

2.3.1 Limiter for Interpolation

The standard MP5 limiter introduced by *Suresh and Huynh* (1997) is used for our face value reconstruction. This limiter tries to control overshoots and undershoots, and it is monotonicity preserving for linear hyperbolic equations. We also need a

limiter for interpolations related to AMR. This limiter should be able to control overshoots and undershoots, but it does not need to be monotonicity preserving. So, following the ideas of MP5 (*Suresh and Huynh*, 1997), we introduce a new limiter $\mathcal{L}$, which is a simplification of MP5, but generalized it to non-equal spaced stencils. We use this limiter in all the interpolations for high-order ghost cells, grid refinement and coarsening, but not for face reconstruction. An example of six-point interpolation is given to illustrate this limiter.

For a set of seven points lying along a line at coordinates $x_{-3} < x_{-2} < x_{-1} < x_0 < x_1 < x_2 < x_3$, we want to interpolate u_0 from the known values $u_{-3}, u_{-2}, u_{-1}, u_1, u_2$ and u_3. These points are not required to be equally spaced. We first interpolate u_0 from the other six points without any limiting and denote this interpolated value as u_0^{orig}. We also calculate the linear extrapolated values from left (u_0^L) and right (u_0^R), and the linearly interpolated u_0^M (see Figure 2.1):

$$u_0^L = \frac{x_{-1} - x_0}{x_{-1} - x_{-2}} u_{-2} + \frac{x_0 - x_{-2}}{x_{-1} - x_{-2}} u_{-1} \tag{2.20}$$

$$u_0^R = \frac{x_2 - x_0}{x_2 - x_1} u_1 + \frac{x_0 - x_1}{x_2 - x_1} u_2 \tag{2.21}$$

$$u_0^M = \frac{x_1 - x_0}{x_1 - x_{-1}} u_{-1} + \frac{x_0 - x_{-1}}{x_1 - x_{-1}} u_1 \tag{2.22}$$

The median of above three values is:

$$u_0^{MD} = \text{median}(u_0^L, u_0^R, u_0^M). \tag{2.23}$$

The final interpolated u_0 should be located in the interval $[u_{min}, u_{max}]$, where:

$$u_{min} = \min(u^{MD}, u_{-1}, u_1) \tag{2.24}$$

$$u_{max} = \max(u^{MD}, u_{-1}, u_1) \tag{2.25}$$

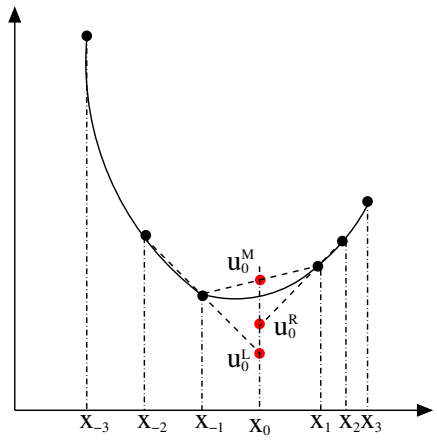

Figure 2.1: Illustration of the limiter.

Finally, we get:

$$u_0 = \text{median}(u^{orig}, u_{min}, u_{max}) \tag{2.26}$$

This limiter suppresses overshoots and undershoots while preserving accuracy near extrema similar to the MP5 limiter (*Suresh and Huynh*, 1997). For positive quantities, like density, pressure, etc, the limiter cannot ensure that the interpolated values are positive, so we use an extra trick to keep positivity: if u_0 from (2.26) is negative and it is positive variable, then replace it with $u_0 = u^M$.

Notice that only the nearby four values (two values each side) are used for limiting, and we notate the limiter as $\mathcal{L}(u_{-2}, u_{-1}, u^{orig}, u_1, u_2)$, which represents the procedures from (2.20) to (2.26) including the positivity fix. This limiter is applied to all the interpolations in this section, and it needs two points on each side. However, for some interpolations in the following, we only know one point on one side, and only one extrapolated value u_0^L or u_0^R can be obtained. For this situation, we assume u_0^{MD} is this known extrapolated value and do not use (2.23) any more. For example, if x_2 and x_3 are not known, u_0^R can not be calculated and we assume $u_0^{MD} = u_0^L$.

2.3.2 High-Order Ghost Cells Calculation

The high-order scheme requires three ghost cell layers, and each block should at least contain twice as many physical cells than ghost cells in each direction in order to satisfy the regridding requirement (*Tóth et al.*, 2012). For making the grid truly adaptive, small size blocks are preferred. So, in this section, we use 6×6 (2D) physical cells blocks, that contain 12×12 cells including ghost cells, to illustrate our algorithm.

After each iteration, the physical cells are updated to a new time level, while the ghost cells still contain the values at the previous time stage. When a ghost cell has the same size as the overlapping physical cell of the neighbor block, such as G1 in Figure 2.2, it is straightforward to obtain the ghost cell value. If the ghost cell and the overlapping physical cell are not at the same refinement level, like G2 in Figure 2.2, we need to interpolate the ghost cell from nearby cells. For pure hyperbolic PDEs, only face ghost cells are needed to calculate fluxes. But corner ghost cells are useful in some other circumstances, such as Hall MHD (*Tóth et al.*, 2008) and dynamic AMR. So high-order corner ghost cells are also calculated.

All the 2D refinement possibilities are shown in Figure 2.3. We calculate ghost cells based on the following rules:

1) Calculate ghost cells from surrounding physical cells with dimension by dimension interpolations. Try fifth-order interpolation first, otherwise use fourth-order interpolation.

2) If some ghost cell values can not be interpolated from physical cells, try to use the ghost cells already interpolated.

3) If several symmetric interpolations are available based on approach 2), use their average.

A 3D grid contains many more possibilities and interpolations are more complicated. Following the strategies described for 2D, we have also implemented high-order interpolation for the ghost cells in 3D.

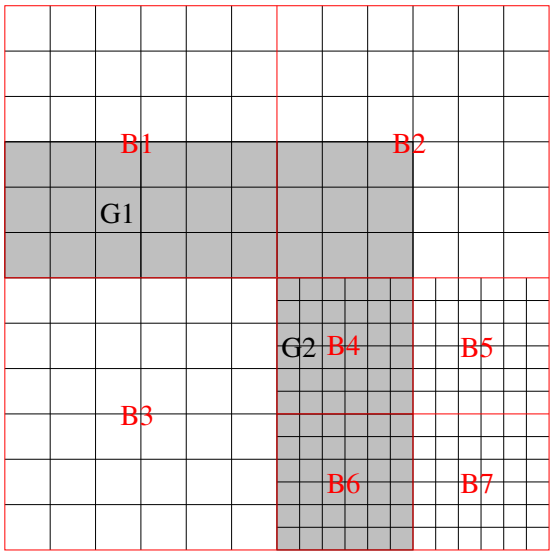

Figure 2.2: Red lines are block edges, black lines are cell boundaries, and the gray region represents B3's ghost cells. Red solid lines represent block edges in all the figures.

2.3.2.1 High-Order Restriction

High-order restriction is done remotely: we restrict the ghost cells of a coarse block on its neighbor fine block, then the fine block sends the ghost cell values to the coarse block.

Case 1 in Figure 2.3 is the simplest situation for high order restriction, where resolution only changes in one direction. The interpolation procedure is shown in Figure 2.4. To restrict ghost cells (red circles) of the coarse block, we use dimension by dimension interpolations: interpolate to the face values (red rectangles) along the y direction first, then interpolate ghost cells from these face values and the coarse cell center value (black circle) in the x direction.

Cases 2 and 3 in Figure 2.3 are more complicated. The interpolation procedure is shown in Figure 2.5. Most ghost cells (red solid circles) are calculated in the same way as for the simple resolution change (Figure 2.4) using left or upper coarse cells. Some of these ghost cells can be obtained both ways, so according to our strategy we use the average of the two interpolations. The corner ghost cell (red dashed circle)

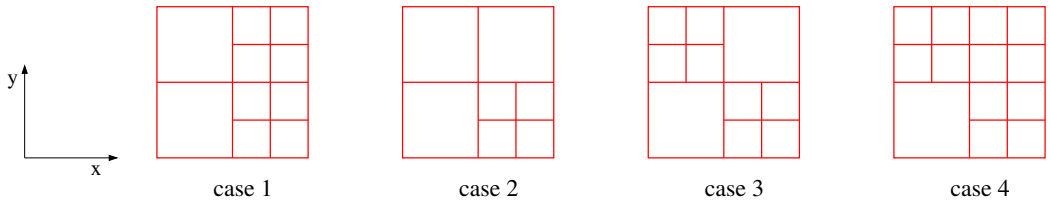

Figure 2.3: Four possibilities of grid resolution change in 2D. Red lines represent block edges.

can be interpolated on the coarse grid using the coarse physical cells and the already calculated coarse ghost cell values. This can be done both in the x and y directions, so again the average is used.

Face ghost cell restriction for case 4 is exactly the same as for case 1. Corner ghost cell restriction for case 4 is shown in Figure 2.6. Most corner ghost cells (red solid circles) are also interpolated with the same idea: dimension by dimension interpolation with nearby physical cells. For the corner ghost cell (dashed red circle), it is not easy to apply dimension by dimension interpolations, and we interpolate it diagonally from coarse physical cells and already known ghost cells.

The limiter $\mathcal{L}$ defined in section 4.1 is applied to all interpolations described in this section, and also the next subsection 4.2.2.

2.3.2.2 High-order Prolongation

High-order prolongation is done locally: we prolong the fine ghost cells using coarse and fine physical cell values passed from the neighboring blocks. This means that the interpolation stencil is restricted to three layers of cells from the surrounding blocks.

To fill in the ghost cells of the fine blocks, we use dimension by dimension interpolations as well. Consider case 1 in Figure 2.3 first, as shown in Figure 2.7. We interpolate in the y direction to get red circles first, then using these red circles and fine physical cells (black squares) we obtain the ghost cells (red squares) with inter-

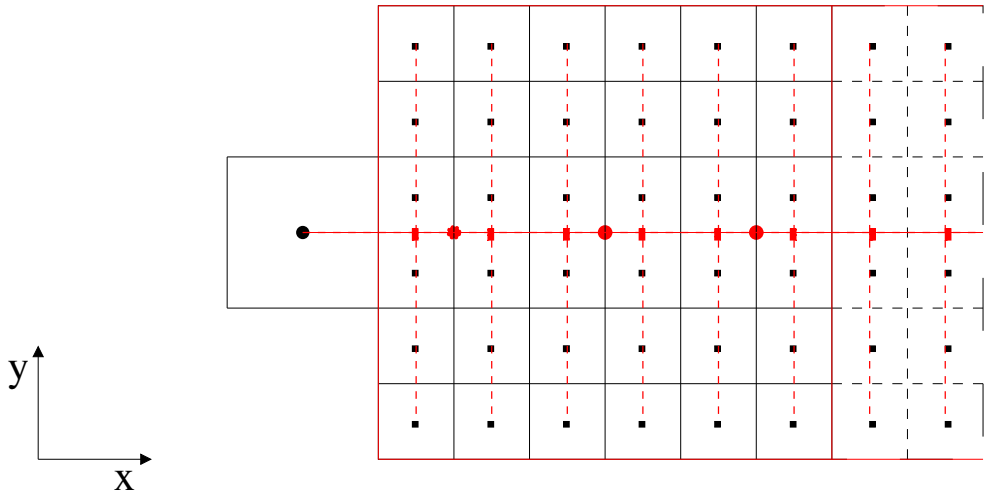

Figure 2.4: High-order restriction at simple resolution change (case 1 in Figure 2.3). Black solid lines and dashed lines represent cell boundaries. The black solid circle is the coarse block cell center value, and the black squares are cell centers of the fine block. We first interpolate to the face values (red rectangles) in the y direction, then use these face values and the coarse cell center value (black circle) to interpolate in the x direction to calculate the ghost cells (red circles) of the coarse block. For a 6×6 block the rightmost two layers of cells (dashed lines) are ghost cells, so we may not be able to use rightmost two face values (red rectangles). In this case the rightmost ghost cell (red circle) is interpolated from the available face values and the limiter is only applied with left extrapolation.

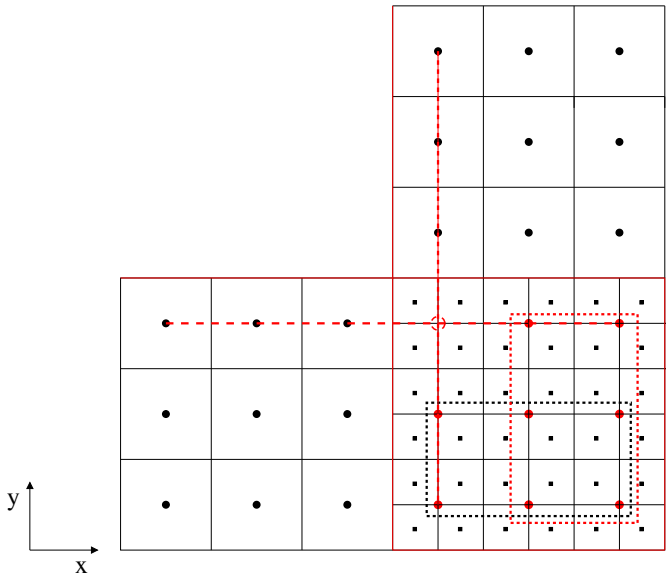

Figure 2.5: High-order restriction for cases 2 and 3 in Figure 2.3. Black circles and squares are physical cells. Red symbols represent ghost cells of the left and upper coarse blocks. Red solid circles in the black and red boxes are calculated the same way as at simple resolution changes (Figure 2.4) with left and upper coarse cells, respectively. For the four points in both boxes, they can be obtained both ways and we use their average. The red dashed circle uses the average of the interpolations from the coarse physical and ghost cells in the x or y directions along the red dashed lines.

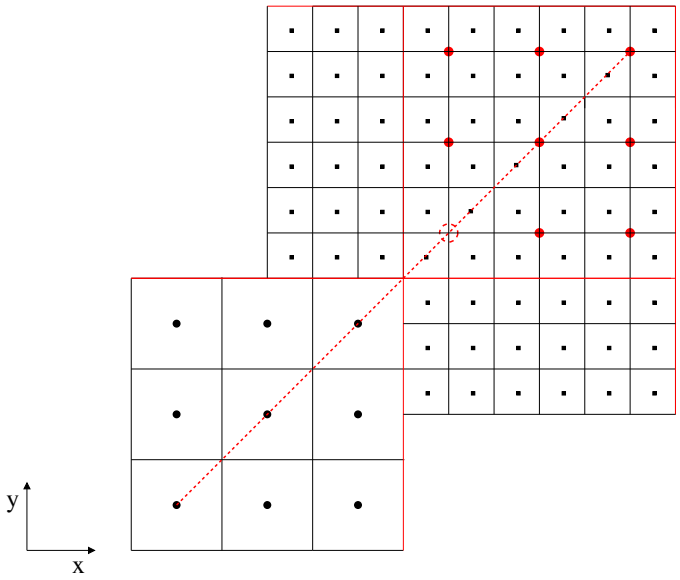

Figure 2.6: High-order restriction for corner ghost cells of case 4 in Figure 2.3. Black circles and squares are physical cells. Red symbols represent corner ghost cells of the coarse block. The red solid circles are calculated from dimension by dimension interpolations. The red dashed circle is interpolated diagonally from coarse physical cells and already interpolated coarse ghost cells.

polation in the x direction. This approach is also applicable to all the fine face ghost cells of case 2 in Figure 2.3.

Cases 3 and 4 contain more possibilities. Some ghost cells (red squares in Figure 2.8) can still be filled in with fifth-order values using the dimension by dimension approach discussed for Figure 2.7. Above the red hexagons in Figure 2.8, there are fewer coarse ghost cells (black circles). We use 4th order accurate interpolation for these ghost cells, which needs fewer points in the y direction. The red circles are obtained with the y direction interpolations, which involves already known ghost cells.

So far, all the face ghost cells for fine blocks are obtained, but their corner ghost cells in case 2 and case 4 are still unknown. We calculate the corner ghost cells remotely. We use case 2 as an example. In case 2, the corner neighbor of the fine block is a coarse block, whose ghost cells are already fifth-order accurate after high-

order restriction. It is easy to calculate the ghost cells of the fine block on the coarse block, and then pass this information to the fine block.

2.3.3 Conservation at Resolution Change

To make the scheme conservative at grid resolution changes, a flux correction (*Berger and Colella*, 1989) procedure should be used. However, we do not use this correction, because it would make the scheme only second-order accurate near resolution changes. As it was analyzed by *Shen et al.* (2011), the flux difference between the coarse and fine meshes is $O(\Delta x^5)$, so the error is small for smooth data. As long as discontinuities do not cross the grid resolutions or move through them quickly, the weak solution will also be accurate. We demonstrate these statements with the numerical tests.

2.3.4 High-Order Dynamic AMR

After all the ghost cells have been filled in with high-order accurate data, including corner ghost cells, it is straightforward to make the mesh refinement and coarsening also high-order accurate. We simply apply high-order dimension by dimension interpolations to every points as needed, and limiter $\mathcal{L}$ is also employed. We note that this procedure is only conservative to truncation error.

2.3.5 Error Analysis for Adaptive Grids

Just as we mentioned in section 2.3, the numerical flux $\mathbf{F}_{i+1/2}$ is a fifth-order accurate approximation, see Eq. (2.8). Most of the ghost cells are fifth-order accurate, which will not change the accuracy of $\mathbf{F}_{i+1/2}$. Near resolution changes, however, the face fluxes at $i-1/2$ and $i+1/2$ have different coefficients in front of the Δx^5 error terms, so these fifth-order errors will not cancel in the spatial difference formula (2.9). Eventhough the ghost cells are fifth-order, the local errors of the finite difference

scheme near resolution changes are only fourth-order accurate. If some of the ghost cells are only fourth-order accurate (see Figure 2.8), the local errors near these cells are third-order.

As long as the lower order accuracy is restricted to a lower dimensional subspace of the computational domain, we can still achieve fifth-order accuracy in the L_1 norm, even if the L_∞ error is only third-order. Let us consider the 2D mesh, case 4 in Figure 2.3. For a given fine grid resolution Δx there are N physical cells and N is proportional to Δx^{-2}. The total number of ghost cells along the grid resolution changes is proportional to Δx^{-1}, so the number of fourth-order accurate physical cells near the resolution changes is $n_4 \propto \Delta x^{-1}$. The number of fourth-order accurate ghost cells at the corners of the grid resolution change is constant, so the number of third-order physical cells n_3 influenced by them is also constant. The L_1 error for this case is then

$$E_{\mathrm{L1}} = \frac{n_3 O(\Delta x^3) + n_4 O(\Delta x^4) + (N - n_4 - n_3) O(\Delta x^5)}{N} = O(\Delta x^5) \qquad (2.27)$$

2.4 Numerical Tests

We solve the Euler equations for density ρ, momentum density $\rho\mathbf{u}$, and energy density e. The pressure is: $p = (\gamma - 1)(\rho e - \frac{1}{2}\rho u^2)$ with $\gamma = 1.4$. To keep the scheme stable and high-order accurate, the strong stability-preserving (SSP) third-order accurate Runge-Kutta (RK3) scheme (*Shu and Osher*, 1988) is employed for time integration. The same time step is used in all grid blocks. The HLLE Riemann solver (*Einfeldt*, 1988) is used for all the simulations below.

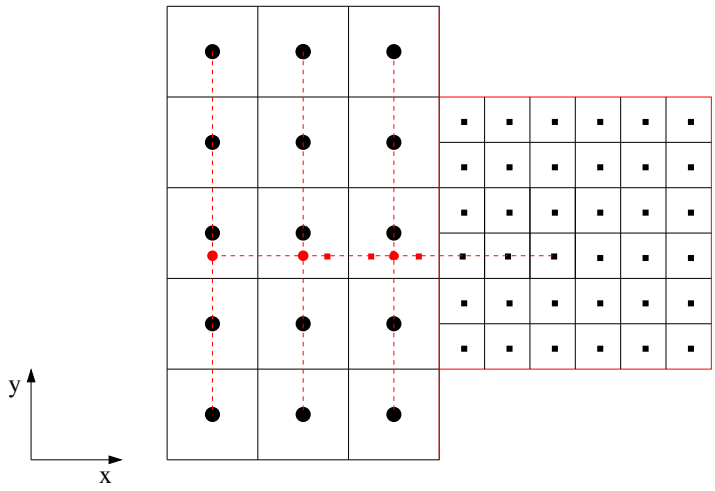

Figure 2.7: High-order prolongation at simple resolution change (case 1 in Figure 2.3). Black circles and squares are physical cells. Red squares are ghost cells of right fine block. We first calculate the face values (red circles) in the y direction, then use these face values and physical cell values (black squares) to interpolate ghost cells in the x direction.

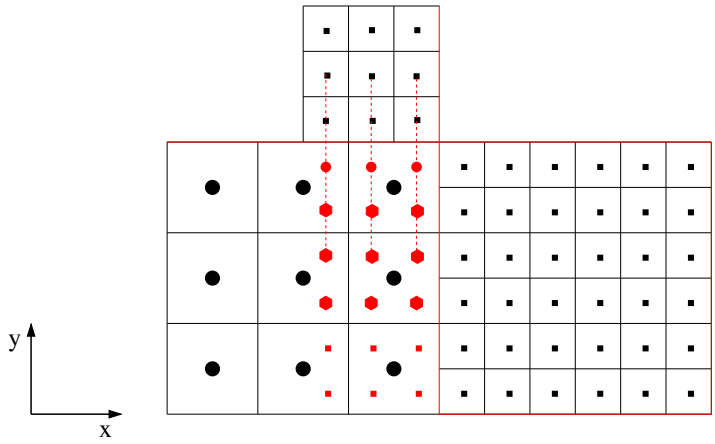

Figure 2.8: High-order prolongation for cases 3 and 4 in Figure 2.3. Red symbols are ghost cells of the right fine block. Red squares are calculated as ghost cells at simple resolution change (Figure 2.7). Red hexagons are also calculated with dimension by dimension interpolations, but the interpolations are only fourth-order accurate and there may be only one point at one side of the interpolated point. The red circles are interpolated in the y direction.

2.4.1 Polynomial Interpolation

To test the accuracy of ghost cells, we set the physical cell values as a fourth-order polynomial of the coordinates:

$$\begin{aligned} f(x,y,z) =& x^4 + y^4 + z^4 + x^3y + x^3z + y^3x + y^3z + z^3x + z^3y \\ &+ x^2y^2 + x^2z^2 + y^2z^2 + x^2yz + xy^2z + xyz^2 \end{aligned} \tag{2.28}$$

then calculate ghost cells. If the interpolations are fifth-order accurate, the ghost cells should be the same as analytic values up to rounding errors. All the possible refinements are tested, and all the ghost cells are proved to be fifth-order except for the red points in Figure 2.8, which are fourth-order accurate and they can achieve analytic values up to rounding errors for third-order polynomials.

The same fourth-order polynomial is also used to test the mesh refinement and coarsening, which are also fifth-order accurate.

2.4.2 2D Acoustic Wave on Refined Cartesian Grid

A smooth but non-linear problem, 2D acoustic wave propagation, is used to test the accuracy of the high-order FD methods on a locally refined Cartesian grid. The acoustic wave is generated by a symmetric pressure perturbation, which is given by a Gaussian profile on the domain $(x, y) \in [0, 1]^2$:

$$p = \begin{cases} 0.6 & \text{if } d > 0.3 \\ 0.6 + 0.1e^{-(d/0.15)^2} \cos^6(0.25\pi d/0.15) & \text{if } d \leq 0.3 \end{cases} \tag{2.29}$$

where $d = \sqrt{(x-0.5)^2 + (y-0.5)^2}$. Note that this function has continuous fifth derivatives. The other variables are uniform: $\rho = 1$ and $\mathbf{u} = 0$.

We run this problem on two different locally refined meshes: the center refined mesh (middle plot of Figure 2.9) and diagonally refined mesh(right panel of Figure

2.9). To study the convergence, we run the same simulation with different cell sizes, and calculate the errors at $t = 0.2$ and list them in Table 2.1. To calculate the error of each point, the 'exact' solution is linearly interpolated from a high resolution (cell size 1/4800) simulation result. Because the spatial derivative is fifth-order, while the time integration is only third-order accurate, we use smaller CFL numbers on finer grids to ensure that the errors are dominated by the spatial discretization errors. The L_1 errors and convergence rates shown in Table 2.1 verify the fifth-order convergence for both kind of refined meshes. As shown in Figure 2.9, the errors in the coarse cells are dominating, and errors do not accumulate near resolution changes.

In the diagonally refinement grid (right panel of Figure 2.9), some special ghost cells of the finer blocks are only fourth-order accurate (see Figure 2.8). These cells are near the domain center for this acoustic wave simulation, where errors are small and do not play an important role. To investigate the influence of these fourth-order ghost cells, we present the following linear advection tests.

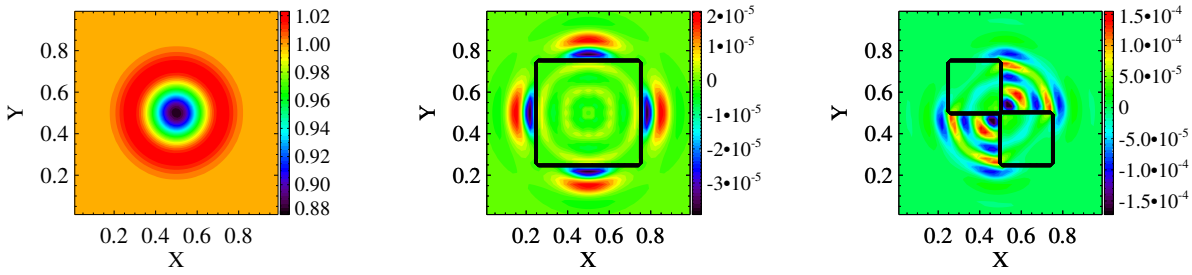

Figure 2.9: Acoustic wave test. Left: density at $t = 0.2$. Middle and right: density errors at $t = 0.2$. The cell size within the black box is 1/96 and outside is 1/48. The refined region is $(x, y) \in [0.25, 0.75] \times [0.25, 0.75]$ for the middle plot. For the right plot, the regions $(x, y) \in [0.25, 0.50] \times [0.50, 0.75]$ and $(x, y) \in [0.50, 0.75] \times [0.25, 0.50]$ are refined. $CFL = 0.4$ is used.

Table 2.1: 2D acoustic wave: density errors

		Middle case in Figure 2.9		Right case in Figure 2.9	
cell size	CFL	L_1 error	L_1 order	L_1 error	L_1 order
1/24 or 1/48	0.8	6.95×10^{-5}	-	1.74×10^{-4}	-
1/48 or 1/96	0.4	3.26×10^{-6}	4.41	1.47×10^{-5}	3.57
1/96 or 1/192	0.2	1.00×10^{-7}	5.03	5.35×10^{-7}	4.78
1/192 or 1/384	0.1	3.00×10^{-9}	5.04	1.70×10^{-8}	4.98

2.4.3 Advection of a Smooth Density Peak on a Two-Level Grid

2.4.3.1 2D Cartesian Grid

To evaluate the influence of the fourth-order ghost cells, we run a linear advection problem with a Gaussian wave moving through the region influenced by these ghost cells. The grids tested are shown in Figure 2.10. For simplicity, we name the refined mesh in the middle and right panels of Figure 2.10 as refined-mesh-1 and refined-mesh-2, respectively. The initial condition in the domain $(x, y) \in [0, 1]^2$ has density

$$\rho = \begin{cases} 1 & \text{if } d > 0.3 \\ 1 + 0.1e^{-(d/0.15)^2} \cos^6(0.25\pi d/0.15) & \text{if } d \leq 0.3 \end{cases} \tag{2.30}$$

where $d = \sqrt{(x - 0.35)^2 + (y - 0.3)^2}$. The velocity $u_x = u_y = 1$ and pressure $p = 1$ are uniform, so the Euler equations reduce to a linear advection equation. The density and errors at $t = 0.35$ are shown in Figure 2.10, and the convergence rates are also listed in Table 2.2 and Table 2.3.

For the refined-mesh-1, the coarse cells dominate the errors and we cannot see the influence of the ghost cells near resolution changes. Figure 2.10 shows that the errors are smooth and the convergence rate is 5 in Table 2.2. This does not mean that the order of accuracy at grid resolution changes is not important. If we switch to a simple second-order accurate interpolation for all ghost cells, then the global L_1 convergence rate drops to 2 (as shown in the rightmost column of Table 2.2) eventhough the same

fifth-order accurate scheme is used otherwise.

The convergence rates of refined-mesh-2 are shown in Table 2.3, which also demonstrate fifth-order accuracy. Although some ghost cells are only fourth-order accurate and influence passing points, the errors are still smooth (right panel of Figure 2.10)

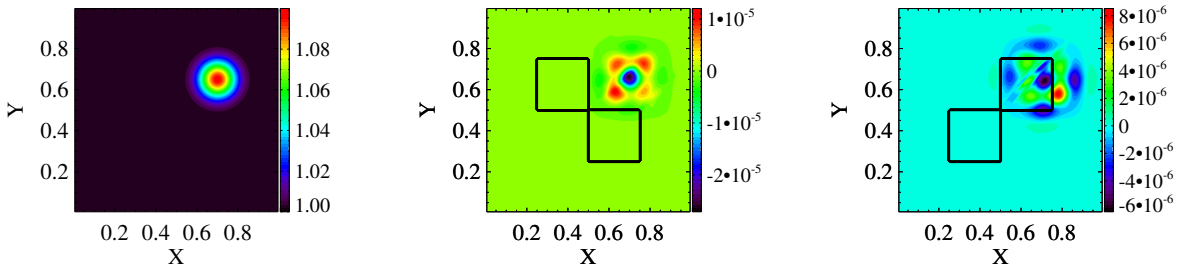

Figure 2.10: Left: density at $t = 0.35$. Middle and right: density errors at $t = 0.35$. The cell size within the black boxes is 1/192 and 1/96 outside. $CFL = 0.2$ is used. The refined regions are $(x, y) \in [0.25, 0.50] \times [0.50, 0.75]$ and $(x, y) \in [0.50, 0.75] \times [0.25, 0.50]$ for the middle plot. For the right plot, the regions $(x, y) \in [0.25, 0.50] \times [0.25, 0.50]$ and $(x, y) \in [0.50, 0.75] \times [0.50, 0.75]$ are refined. We name the refined mesh in the middle and right as refined-mesh-1 and refined-mesh-2, respectively.

Table 2.2: Errors of smooth advection test with refined-mesh-1 (middle panel of Figure 2.10).

		high-order ghost cells		second-order ghost cells	
cell sizes	CFL	L_1 error	L_1 order	L_1 error	L_1 order
1/24 & 1/48	0.8	2.02×10^{-4}	-	3.12×10^{-4}	-
1/48 & 1/96	0.4	1.28×10^{-5}	3.98	5.03×10^{-5}	2.63
1/96 & 1/192	0.2	4.19×10^{-7}	4.93	1.14×10^{-5}	2.14
1/192 & 1/384	0.1	1.31×10^{-8}	5.00	2.82×10^{-6}	2.02

2.4.3.2 2D Curvilinear Grid

To verify the order of accuracy on a non-Cartesian grid, we redo the advection test on a refined cylindrical mesh. The simulation domain is part of a cylinder: $r \in [1, 10], \theta \in [0°, 180°]$. The initial condition is $u_x = 2$, $u_y = 2$, $p = 1$ and

Table 2.3: Errors of smooth advection test with refined-mesh-2 (right panel of Figure 2.10.

cell sizes	CFL	L_1 error	L_1 order
1/24 & 1/48	0.8	1.29×10^{-4}	-
1/48 & 1/96	0.4	8.06×10^{-6}	4.00
1/96 & 1/192	0.2	2.59×10^{-7}	4.96
1/192 & 1/384	0.1	8.01×10^{-9}	5.02

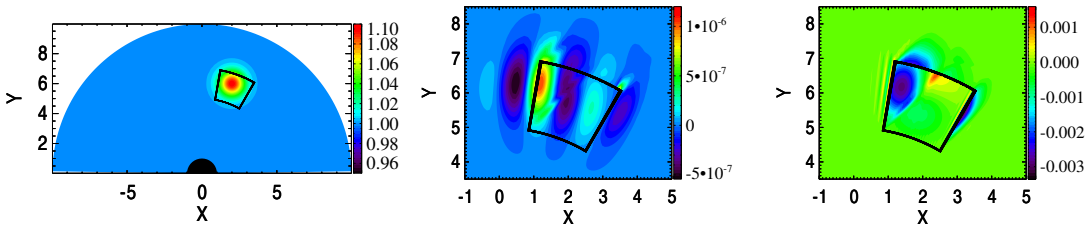

Figure 2.11: Linear advection on cylindrical mesh. The computational domain is $1 < r < 10$ and $0° < \theta < 180°$. The region $(r, \theta) \in [5, 7] \times [60°, 80°]$ indicated by the black box is refined with $\Delta r = 1/96$ and $\Delta\theta = 180°/432$, while the resolution outside the box is $\Delta r = 1/48$ and $\Delta\theta = 180°/216$. $CFL = 0.2$ is used. Left: density at $t = 1$. Middle: density errors for high-order ghost cells at $t = 1$. Right: density errors for second-order ghost cells at $t = 1$. Note that their color ranges are different.

$$\rho = \begin{cases} 1 & \text{if } d > 3 \\ 1 + 0.1e^{-(d/1.5)^2} \cos^6(0.25\pi d/1.5) & \text{if } d \le 3 \end{cases} \tag{2.31}$$

where $d = \sqrt{x^2 + (y-4)^2}$. The density perturbation moves across the corner of the refined mesh, and the cells along the moving path have aspect ratio about 5. The results and errors at $t = 1$ are shown in the left and middle panels of Figure 2.11. There are no errors in the uniform flow region thanks to the free-stream preserving discretiazion. The errors around the density peak are are smooth. For comparison, we also do the simulation with second order accurate ghost cells. In this case the errors concentrate at the resolution change (right panel). The errors and L_1 convergence rates listed in Table 2.4 verify fifth-order accuracy when the high-order accurate ghost cells are used.

Table 2.4: Errors of smooth advection test on a two-level cylindrical mesh (Figure 2.11).

cell sizes (ΔR)	CFL	L_1 error	L_1 order
1/12 & 1/24	0.8	2.39×10^{-5}	-
1/24 & 1/48	0.4	9.03×10^{-7}	4.73
1/48 & 1/96	0.2	2.92×10^{-8}	4.95
1/96 & 1/192	0.1	9.13×10^{-10}	5.00

2.4.3.3 3D Grid

A linear advection problem on 3D two-level Cartesian grid is also used to test accuracy. The center cube $(x, y, z) \in [0.25, 0.75]^3$ on the domain $(x, y, z) \in [0, 1]^3$ is refined. The initial condition is $u_x = u_y = u_z = 1$, $p = 1$ and

$$\rho = \begin{cases} 1 & \text{if } d > 0.3 \\ 1 + 0.1e^{-(d/0.15)^2} \cos^6(0.25\pi d/0.15) & \text{if } d \leq 0.3 \end{cases} \tag{2.32}$$

where $d = \sqrt{(x-0.4)^2 + (y-0.3)^2 + (z-0.3)}$. The wave is moving diagonally and the errors at $t = 0.35$ are shown in Table 2.5, confirming that the convergence rate is very close to 5.

Table 2.5: Errors of smooth advection test on a two-level 3D grid

cell sizes	CFL	L_1 error	L_1 order
1/24 & 1/48	0.8	1.60×10^{-5}	-
1/48 & 1/96	0.4	8.10×10^{-7}	4.31
1/96 & 1/192	0.2	2.59×10^{-8}	4.97
1/192 & 1/384	0.1	8.98×10^{-10}	4.85

2.4.4 Square Wave Advection on a Two-Level Mesh

The advection of a square wave on refined-mesh-1 (middle panel of Figure 2.10) is used to test for spurious oscillations near discontinuities and the conservation properties of the scheme. The grid resolution in 1/192 in the refined regions and 1/96

elsewhere. Initially, the square wave has density $\rho = 2$ between $x = 0.2$ and $x = 0.4$ and the background has $\rho = 1$. The velocity is $u_x = 1$ and periodic boundary conditions are applied in both directions.

After one period, at $t = 1$, a cut of the solution at $y \sim 0.45$ is shown in the left panel Figure 2.12. There are very small under- and overshoots near the discontinuities because the monotinicity-preserving property of the MP5 limiter is somewhat compromised by the high-order flux correction (2.5). The solution obtained on a uniform grid with cell size 1/96 is almost identical, which shows that the errors introduced by the grid resolution change are insignificant. This result demonstrates that the high-order finite difference scheme can resolve the discontinuity very well.

The average density will not change if the scheme is perfectly conservative, which is the case on the uniform grid. But our scheme is not conservative at grid resolution changes. The relative average density error is shown in Figure 2.13 for 10 periods. After the relative errors increase at the first few steps, the perfect square wave is slightly smoothed and the average density starts to oscillate with a very small amplitude as the wave moves through the resolution changes. The average density error remains very small and it does not accumulate.

2.4.5 Lax's Shocktube Problem

To prove that the scheme can obtain weak solutions correctly, we run Lax's shocktube problem (*Lax*, 1954) on a locally refined mesh, which is refined for $x \in [-2, -1]$ and $x \in [1, 2]$. The initial left and right states are

$$\begin{aligned} (\rho_L, u_L, p_L) &= (0.445, 0.698, 3.528) \\ (\rho_R, u_R, p_R) &= (0.5, 0, 0.571) \end{aligned} \tag{2.33}$$

The discontinuity is at $x = 0$ initially and the results at $t = 1.3$ are shown in Figure 2.14, which also includes uniform grid results for comparison. The two simulations

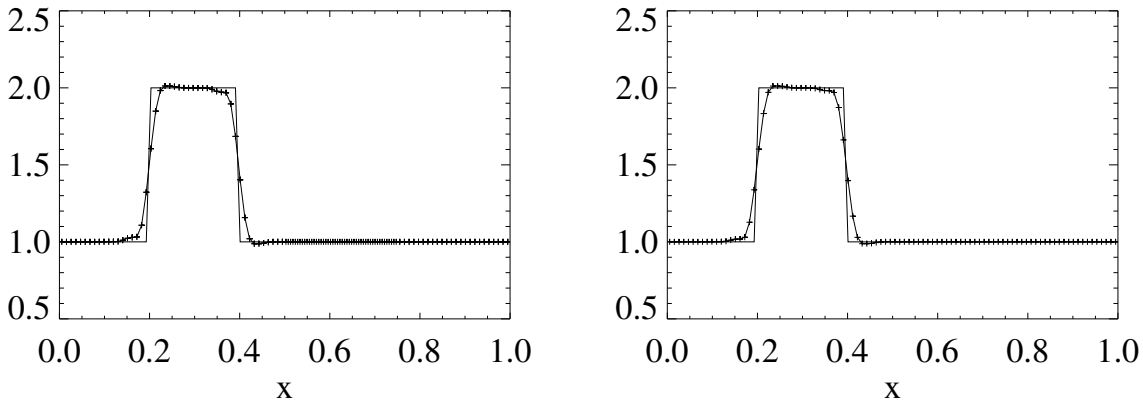

Figure 2.12: Results of the square wave advection test after one period. Left: the cut at $y \sim 0.45$ from a 2D grid (middle panel of Figure 2.10) is shown. The cell size is $1/192$ for $x \in [0.5, 0.75]$ and $1/96$ elsewhere. Right: uniform grid with cell size $1/96$. $CFL = 0.8$ are used for both cases.

give very similar results. Since there is a resolution change at $x = 2$ in the non-uniform grid, which is just behind the contact discontinuity, the oscillation of density is more obvious for the refined mesh. A simulation with much smaller cell sizes, which is not shown here, confirms that the solution converges to the correct weak solution.

To test how the locally refined curvilinear mesh deals with discontinuities, the Lax's problem is also done on the mesh, which is shown in Figure 2.11. It is difficult to set exact boundaries for this case, so we simply use zero gradient boundary condition for all boundaries. Initially the discontinuity is at $x = 0$, and the results at $t = 1.3$ are shown in Figure 2.15. The simulation is influenced by the non perfect boundaries. But the middle of the domain has not been affected by $t = 1.3$, and the shock front keeps straight even after it moves across the locally refined region. A cut along $y = 6$ shows that the discontinuities and the rarefaction wave are well resolved (see right panel of Figure 2.15). These tests verify that the scheme can resolve shocks correctly and accurately.

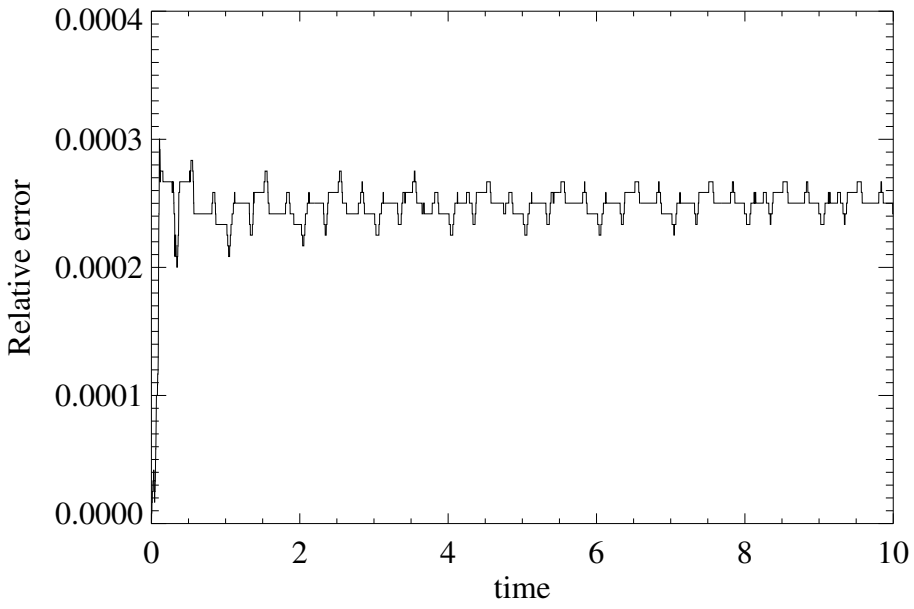

Figure 2.13: The relative error of average density for square wave advection on a two-level mesh for 10 periods.

2.4.6 Freee-Stream Preservation on Two-Level Curvilinear Grid

To verify the free-stream preservation property in 3D, we do a test on a refined spherical grid. To avoid singularities at the poles and the center, the computational domain is $(r, \phi, \theta) \in [120, 200] \times [0, 2\pi] \times [-\pi/4, \pi/4]$. The cell size for $r > 160$ is $\Delta r = 80/24$, $\Delta\phi = 2\pi/24$ and $\Delta\theta = \pi/12$, while for $r < 160$ the grid is refined by one level. The initial condition is a uniform flow with $\rho = 1$, $u_x = u_y = u_z = 1$ and $p = 1$. After 100 steps, the maximum error of all the variables is 2.5×10^{-14}, which is close to the rounding error.

2.4.7 The Shock-Ramp Problem on a 3-Level Dynamically Refined Grid

Shock-ramp problem (*Woodward and Colella*, 1984) describes a Mach 10 shock moving at an angle 60° into a reflecting wall on the computational domain $(x, y) \in [0, 4] \times [0.1]$. The wall is represented by reflecting boundary conditions from $x = 1/6$ to

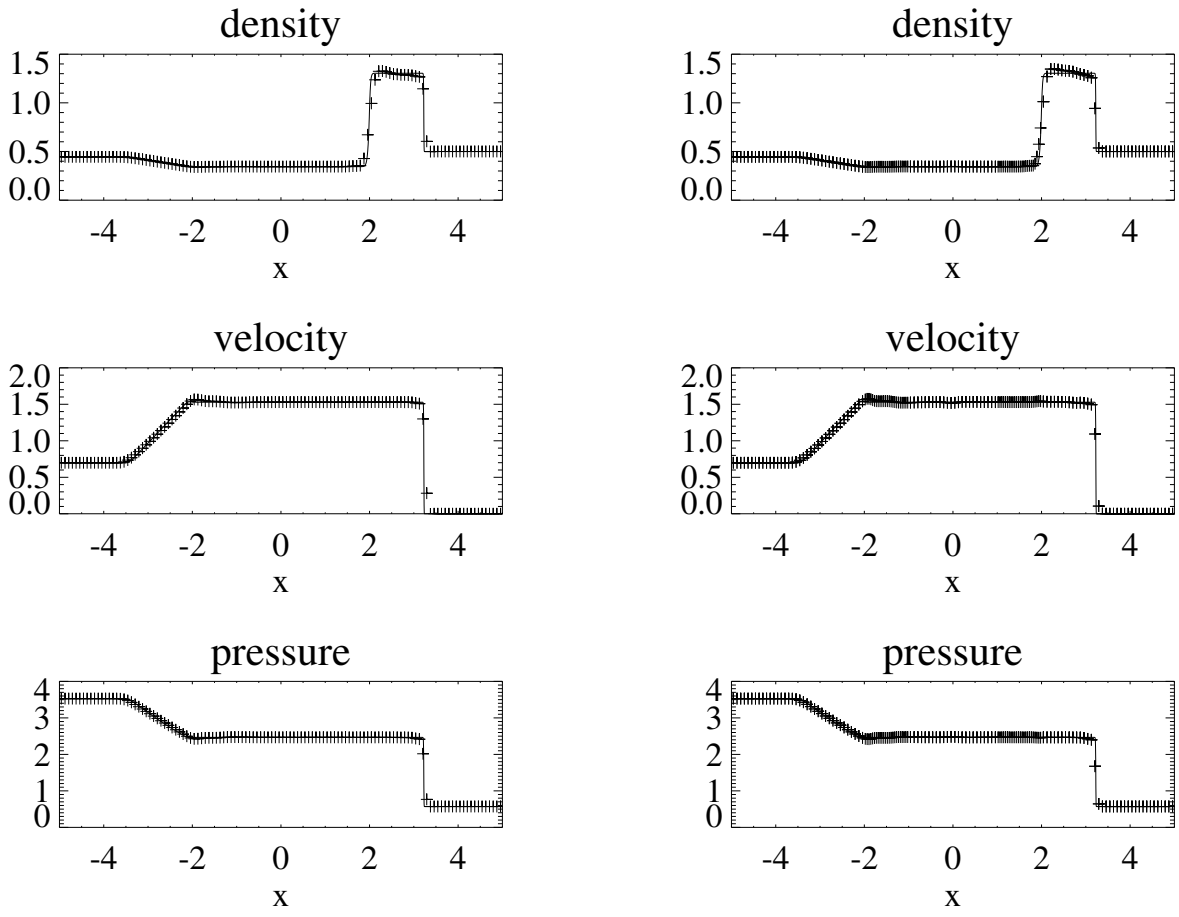

Figure 2.14: Lax's problem at $t = 1.3$. Left: uniform grid with cell size $1/12$. Right: cell size for $x \in [-2, -1]$ and $x \in [1, 2]$ is $1/24$, otherwise is $1/12$. $CFL = 0.8$ is used.

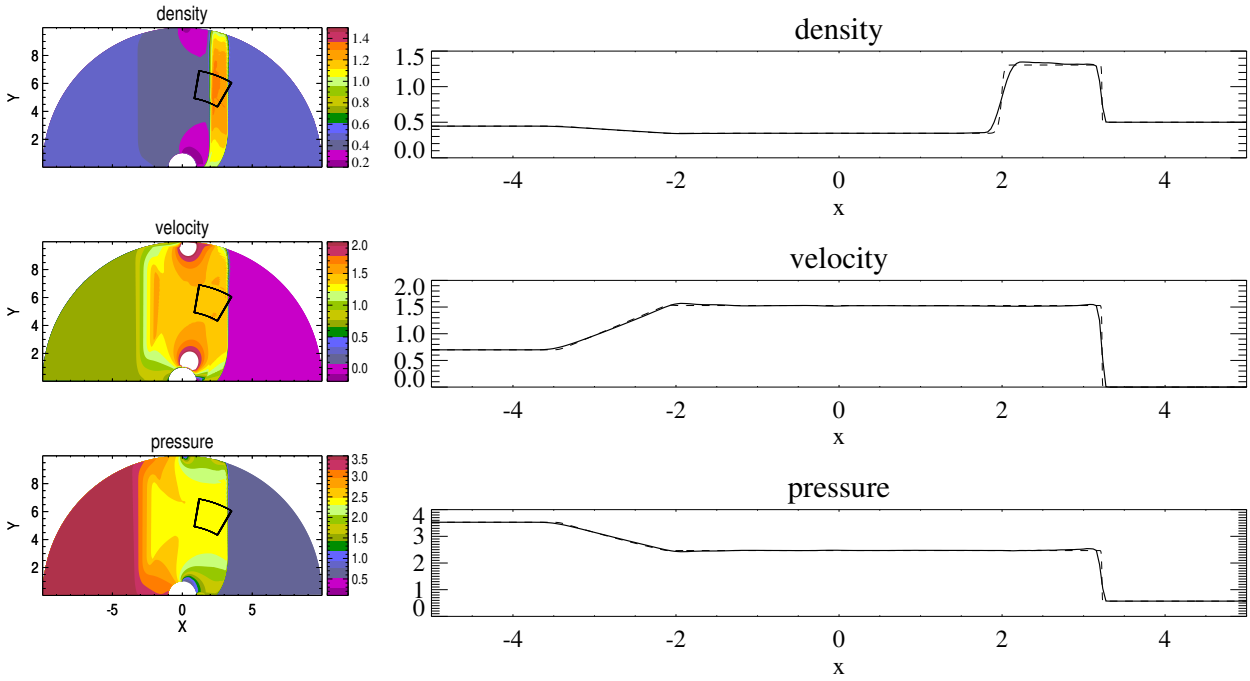

Figure 2.15: Lax's problem on a 2D locally refined cylindrical mesh. The mesh is the same as the one shown in Figure 2.11 and $CFL = 0.8$ is used. Left: results at $t = 1.3$. Right: solid lines are numerical solutions along y=6.0, and dashed lines are exact solutions.

$x = 4$ at the $y = 0$ boundary. The inclined shock front goes through $(x, y) = (1/6, 0)$ initially. In the pre-shock region, the uniform state is

$$(\rho, u_x, u_y, p) = (1.4, 0, 0, 1)$$

while in the post-shock region:

$$(\rho, u_x, u_y, p) = (8.0, 7.1447, -4.125, 116.5)$$

We run this test on a three-level dynamically refined mesh. The base grid has 240×60 cells, so the effective resolution is 960×240. The mesh is dynamically refined every time step to capture large density gradients. $CFL = 0.8$ is used from the beginning. The density and the AMR grid at $t = 0.2$ are shown in Figure 2.16.

Details of the solution are presented in Figure 2.17, which shows that our scheme resolves the various features, including the K-H instability as well as other high-order schemes with comparable grid resolution (*McCorquodale and Colella*, 2011; *Li and Jaberi*, 2012; *Dumbser et al.*, 2013; *Shen et al.*, 2011; *Balsara et al.*, 2009).

The efficiency of the fifth-order scheme is compared with the second-order scheme for this shock-ramp problem (see Table 2.6). The second-order scheme, which employs the HLLE solver and the generalized Koren's limiter (*Koren*, 1993), uses second-order ghost cells and is combined with a two-stage time integration. For the runs with 240×60 uniform grid on one processor, the fluxes and face values calculations dominate the simulation cost. The high-order scheme needs about 3 times more computational time, because 1) it employs the three-stage RK3 to keep both accuracy and stability, 2) the face value calculation and face flux correction make the scheme more complicated. The three-level dynamic adaptive grid that has 960×240 effective resolution is tested on 32 processors, and the high-order scheme also needs about 3 times more time. In addition to face values and fluxes calculations, the ghost cell filling, block refinement and coarsening also need more computation for the high-order scheme. The cell center flux calculation uses about 20% of the total computing time for the uniform grid, and about 10% for the three-level AMR grid.

Table 2.6: Timings for the shock ramp test in seconds. The AMR grid has 4 times higher effective resolution.

	uniform grid on 1 processor		three-level AMR on 32 processors	
	2nd order	5th order	2nd order	5th order
Calculate fluxes	8.38	29.31	2.28	7.66
Calculate center flux	–	9.67	–	2.40
Calculate face values	2.70	9.48	0.84	3.58
Filling ghost cells	–	–	1.25	6.88
Dynamic AMR	–	–	2.22	4.11
Total	13.76	43.63	7.61	22.42

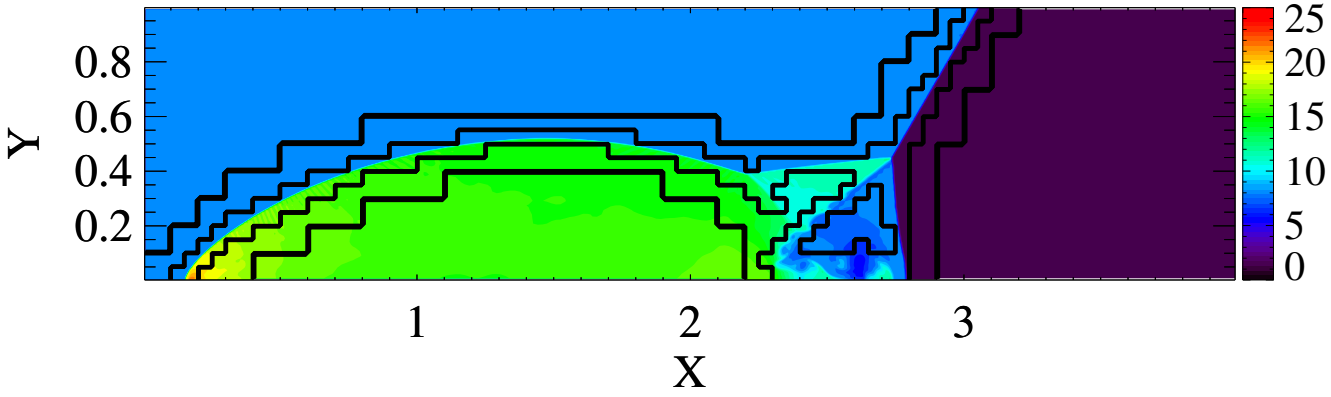

Figure 2.16: Shock-ramp problem: density contour at $t = 0.2$. Black lines show grid resolution changes. There are 3 levels with refinement ratio 2. The effective resolution is 960×240.

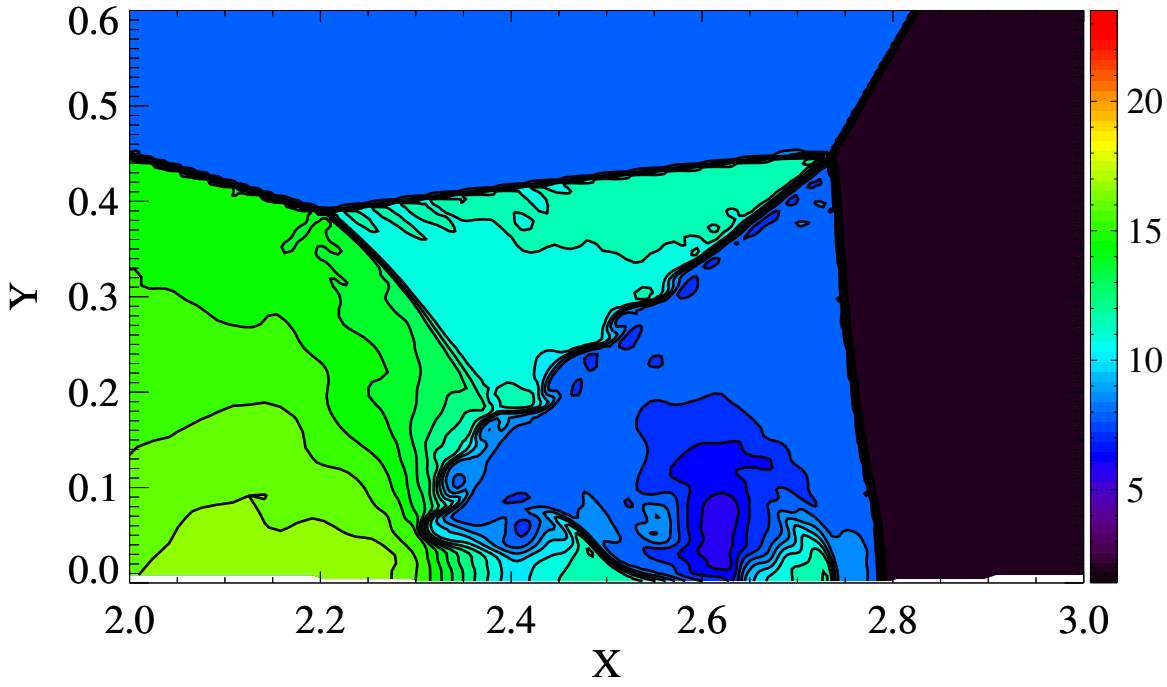

Figure 2.17: Detail of Figure 2.16 near the shock front. The white regions at the bottom edge are due to plotting the AMR grid.

2.5 Summary

In this chapter, a fifth-order accurate finite difference scheme for hyperbolic equations on block-adaptive curvilinear grids was introduced. Our goal is to solve a variety of hyperbolic systems of equations, so the scheme does not use characteristic variables or other equation specific algorithms. Based on a careful evaluation of available options, we opted for a finite difference discretization with a fifth-order montonicity preserving limiter, combined with the flux correction introduced by *Deng and Zhang* (2000) and *Del Zanna et al.* (2007) as the base scheme. First, the scheme constructs fifth-order accurate left and right states at the cell faces. These states are used to calculate face fluxes with a standard approximate Riemann solver. The face fluxes are corrected to make sure that the spatial derivatives are fifth-order accurate. As a novelty, we use cell centered fluxes for the correction step so that the stencil of the scheme is not increased. The solution is updated by simple finite differences of the corrected fluxes. Source terms can be easily evaluated at the cell centers. The stencil of the scheme is only 3 cells on both sides in all dimensions, so 7 cells in 1D, 13 cells in 2D and 19 cells in 3D. This is quite compact compared to typical high-order accurate finite difference and finite volume methods. We use a third order accurate Runge-Kutta scheme for time discretization.

Extending the scheme to curvilinear grids is relatively straightforward. The equations are transformed into a conservative form in generalized coordinates. The geometrical coefficients of the transformation are calculated with the proper discretization so that free-stream solution is preserved.

For block-adaptive grids, our scheme requires 3 layers of ghost cells only, which is only moderately larger than the 2 ghost cell layers required by TVD type schemes. Due to this, the minimum size of the grid blocks is 6 cells in each direction compared to 4 cells for the second order scheme. We note that the scheme can be easily adapted to patch-based AMR grids too as long as the patches have at least 6 cells in every

dimension. The face and corner ghost cells at resolution changes are interpolated with consequtive one-dimensional interpolations. Each 1D interpolation step employs a limiter, which is a simplified version of MP5 but generalized to non-uniform stencil. The limiter suppresses spurious oscillations near sharp gradients, but the ghost cells are still filled in with fifth-order (or in some exceptional cases forth-order) accuracy in smooth regions including local extrema. We use the same interpolation technique and limiter for coarsening and refining the grid during dynamic grid adaptation. The resulting discretization is fifth-order accurate in the L_1 norm on the multi-level AMR meshes. The free-stream preserving property also carries over to curvilinear adaptive grids.

There are, of course, some compromises we had to make. While the finite difference scheme is conservative to round-off errors on a uniform (curvilinear) grid, the conservation is only down to truncation error at grid resolution changes and during dynamic refinement and coarsening. This is not easy to fix, because the high-order finite difference algorithm is not compatible with a simple flux correction step that is standard for finite volume AMR methods. As long as the grid resolution changes and discontinuities (shocks) are not aligned for extended time, the error remains small, and correct weak solutions can be obtained, as demonstrated by some of the numerical tests.

We also note, that our finite difference scheme is not monotonicity-preserving because the flux correction step (2.5) is not limited. This latter problem should be relatively easy to fix with a properly designed limiter, but our numerical tests suggest that the scheme performs remarkably well even without a flux-correction limiter.

CHAPTER III

Magnetohydrodynamics with Embedded Particle-in-Cell Simulation of Earth's Dayside reconnection

This chapter discusses the MHD-EPIC simulation of Earth's magnetosphere. The dayside magnetopause is covered by a PIC box to study the magnetic reconnection. The flux transfer events (FTEs) and the reconnection related kinetic phenomena are presented.

3.1 Model Description

The MHD-EPIC model has been successfully applied to investigate the interaction between the Jovian wind and Ganymede's magnetosphere, where the ion inertial length is large compared to the size of its magnetosphere (*Tóth et al.*, 2016). In this chapter, the same model is applied to study Earth's magnetosphere, which is more challenging because of the small kinetic scale. The MHD-EPIC model two-way couples the BATS-R-US (*Powell et al.*, 1999; *Tóth et al.*, 2008) MHD code and the implicit particle-in-cell code iPIC3D (*Markidis et al.*, 2010) through the Space Weather Modeling Framework (SWMF) (*Tóth et al.*, 2005, 2012). A general description of the these models and the simulation setup is provided in this session.

3.1.1 Global MHD Model: BATS-R-US

In order to make the MHD model as complete as possible, the Hall term and the electron pressure gradient term are included in the generalized Ohm's law, and a separate electron pressure equation is solved. The generalized Ohm's law we use is:

$$\mathbf{E} = -\mathbf{u} \times \mathbf{B} + \frac{\mathbf{J} \times \mathbf{B}}{q_e n_e} - \frac{\nabla p_e}{q_e n_e} \tag{3.1}$$

where q_e, n_e and p_e are the charge per electron, electron number density and electron pressure, respectively. The electron pressure is obtained from:

$$\frac{\partial p_e}{\partial t} + \nabla \cdot (p_e \mathbf{u}_e) = (\gamma - 1)(-p_e \nabla \cdot \mathbf{u}_e) \tag{3.2}$$

where $\gamma = 5/3$ is the adiabatic index, and $\mathbf{u_e} = \mathbf{u} - \mathbf{J}/(q_e n_e)$ is the electron velocity.

From the numerical prospective, it is not trivial to incorporate the Hall term into the MHD equations. The Hall MHD equations support the whistler mode wave, which is dispersive and the characteristic speed is inversely proportional to the wave length. Since the shortest wave length that can be resolved in a numerical system is twice the cell size, the fastest whistler wave speed is proportional to $1/\Delta x$. For an explicit time integration scheme, the time step is limited by the CFL condition, which leads to a time step approximately proportional to $1/(\Delta x)^2$ for Hall MHD. In order to use a reasonably large time step, a semi-implicit time discretization is employed (*Tóth et al.*, 2012). The semi-implicit scheme treats the stiff terms, which is the Hall term here, and other terms separately. Excluding the Hall term, the rest of the equations are updated with an explicit scheme, and the time step is only limited by the fast magnetosonic wave speed. The Hall term is handled by an implicit solver after the explicit update has been done.

The typical solar wind condition at 1AU with purely southward IMF is used as the boundary condition to drive the magnetosphere: $\mathbf{B} = (0, 0, -5)$ nT, mass density $\rho = 5\,\mathrm{amu/cm^3}$, ion pressure $p_i = 3.45 \times 10^{-3}$ nPa, and solar wind velocity $\mathbf{u} = (-400, 0, 0)$ km/s. Electron pressure $p_e = 8p_i = 2.76 \times 10^{-2}$ nPa is used, so that after crossing the shock, where the ions are heated by converting bulk into thermal energy while the electron thermal energy changes adiabatically, the ion-electron pressure ratio is about $p_i/p_e \sim 2.5$. *Wang et al.* (2012) shows that the temperature ratio T_i/T_e in the solar wind varies from $0.1 \sim 2$, and the ratio is about $4 \sim 12$ inside the magnetosheath. The T_i/T_e ratio, which is the same as p_i/p_e, used in the simulation is close to but slightly smaller than the typical observed ratio. We use $T_i/T_e = 1/8$, because our numerical experiments show that the electrons can be numerically heated by PIC if colder solar wind electrons are used as boundary condition. A magnetic dipole with 30116 nT field strength at the magnetic equator is used. Its magnetic axis is aligned with the z axis. The total magnetic field $\mathbf{B}$ is split into the intrinsic dipole field $\mathbf{B_0}$ and the deviation $\mathbf{B_1}$. A three-dimensional block-adaptive Cartesian grid is used to cover the whole magnetosphere: $-224\,R_E < x < 32\,R_E$, $-128\,R_E < y < 128\,R_E$ and $-128\,R_E < z < 128\,R_E$. Since we focus on the dayside dynamics in this chapter, the mesh along the dayside magnetopause is refined to high resolution with $\Delta x = 1/16\,R_E$ (see Figure 3.1). 59 million cells are used in total. At the inner boundary $r = 2.5\,R_E$, the density is fixed as $28\,\mathrm{amu/cm^3}$, the pressure and the magnetic field $\mathbf{B_1}$ have zero gradient, the radial velocity is zero, while the tangential velocity is calculated from the ionosphere electrodynamics model developed by *Ridley et al.* (2004).

3.1.2 Implicit Particle-in-Cell Model: iPIC3D

The semi-implicit particle-in-cell code iPIC3D was developed by *Markidis et al.* (2010). The advantage of iPIC3D over explicit particle-in-cell codes is that iPIC3D is linearly unconditionally stable, so that iPIC3D can handle larger time step and larger cell size than explicit PIC. Compared to the explicit PIC method, the cell size of iPIC3D is chosen based on the scale of interest instead of the Debye length, and the time step of iPIC3D is not limited by the plasma frequency or the speed of light, but the accuracy condition, which requires $v_{rms}\Delta t/\Delta x < 1$ on all grid nodes for all species, where v_{rms} is the root mean square of macro-particle velocities. In order to make the simulation as efficient as possible while keeping the accuracy condition satisfied, we use an adaptive time step:

$$\Delta t = c_0 \cdot \min(\Delta x/v_{rms},\, \Delta y/v_{rms},\, \Delta z/v_{rms}) \tag{3.3}$$

calculated for each grid nodes and the minimum is taken over the whole PIC mesh. The root mean square velocity v_{rms} is similar to the thermal velocity but contains the effect of bulk velocity. c_0 is a coefficient that should be smaller than 1. $c_0 = 0.4$ is used for the simulation in this chapter.

Since the focus of this chapter is the dayside magnetopause reconnection, the embedded PIC box is placed near the sub-solar magnetopause, where reconnection happens under purely southward IMF. In the GSM coordinates, the region inside $8\,R_E < x < 12\,R_E$ and $-6\,R_E < y, z < 6\,R_E$ (see Figure 3.1) is solved by iPIC3D. The PIC region covers the magnetopause and it is just inside the bow shock. Since the size of the ion diffusion region is the same order as the ion inertial length, such kinetic scale should be resolved in order to capture reconnection kinetic physics. However, the ion inertial length $d_i = c/\omega_{pi}$ is about 60km $\sim 1/100\,R_E$ for a typical magne-

tosheath density of $20\,\mathrm{amu/cm^3}$. The length is so small that it is extremely difficult to resolve even for a 3D global MHD model, not to mention the PIC code. Scaling up the kinetic length helps to reduce computational resources. In the present simulation, all the fluid values, including density, pressure, velocity, IMF and dipole field strength, hence the derived values like the sound speed, Alfven velocity and plasma beta, are realistic so that the global structure of the magnetosphere is comparable to the real situation. On the other hand, the ion inertial length is scaled up 16 times to about $1/6\,R_E$ in the magnetosheath by artificially increasing ion mass per charge by a scaling factor of 16. Since all the quantities are normalized in the numerical model, there are several ways to understand or interpret the scaling. One way is treating the scaling as changing the charge of ions and electrons. Compared with the original system, we reduce the charge by a factor of 16 while all the other basic physical quantities, like mass per ion, number density, and temperature remain realistic. From the perspective of ideal magnetohydrodynamics, the scaled system is exactly equivalent to the original one. For a particle-in-cell code, the reduction of charge per ion reduces the electromagnetic force on an ion and therefore increases the gyroradius and gyroperiod by a factor of 16. But the gyroradius and the gyroperiod are still several orders smaller than the global spatial and temporal scale, for example the distance from Earth to the magnetopause and the time for the plasma moving from the subsolar point to the cusp, respectively. How the scaling changes the structure of reconnection is discussed in details in the paper by *Tóth et al.* (2017, submitted paper). We also apply a reduced ion-electron mass ratio $m_i/m_e = 100$, which is sufficiently large to separate the electron and ion scales. We choose $\Delta x = 1/32\,R_E$ as the PIC grid resolution so that $\Delta x/d_i \sim 5$ and $\Delta x/d_e \sim 0.5$. This resolution keeps a balance between the computational cost and the requirement of resolving kinetic scales. 216 particles per cell per species are used and there are about 9 billion particles in total inside the domain initially. Our numerical experiments suggest smoothing the electric field $\mathbf{E}$

and the current density $\mathbf{j}$ can help to suppress the numerical noise (*Tóth et al.*, 2017, submitted paper).

The typical magnetic field strength in the magnetosheath is about 30 nT, and the corresponding ion gyro-frequency is $\Omega_{ci} = 0.0286$Hz and $\Omega_{ce} = 2.86$Hz with scaled charge-mass ratio. As mentioned above, the time step of iPIC3D is determined by the accuracy condition (Eq. 3.1.2). From the simulation, we find the maximum thermal speed of electrons inside the PIC domain is about 2500km/s, which leads to a time step of $\Delta t \sim 0.03s \sim 10^{-3}\Omega_{ci}^{-1} \sim 0.1\Omega_{ce}^{-1}$ with cell size $\Delta x = 1/32\, R_E$. Therefore, the time step is small enough to resolve the gyro-motion of both electrons and ions.

3.1.3 Coupling Between BATS-R-US and iPIC3D

In the simulation presented here, the time step for BATS-R-US and iPIC3D are around $\Delta t_{MHD} = 0.015$ s and $\Delta t_{PIC} = 0.032$ s, respectively. The coupling time interval is set to a small value $\Delta t_{couple} = 0.005$ s so that MHD and PIC are coupled every time step. We note that the time step of PIC is even larger than the MHD, because the MHD time step is limited near the magnetic poles due to the high Alfven speed, while these regions are outside the PIC domain.

We used to generate particles in only one ghost cell layer (*Daldorff et al.*, 2014) as particle boundary condition. Our numerical experiments suggest using more layers (5 layers specifically in this chapter) as the particle boundary, while the electromagnetic field boundary is still only enforced at the outermost layer, is helpful to smoothly transit from PIC to MHD. The MHD cells overlapped with the PIC particle boundary are not overwritten by PIC. Similar technique has been used to implement open boundary condition for stand-alone PIC simulations (*Peng et al.*, 2015).

We run the simulation on 6400 processors for 170 hours to model one hour simulation time on Blue Water supercomputer (*Bode et al.*, 2012). iPIC3D and BATS-R-US use about 80% and 15% of the simulation time, respectively. The coupling and other overheads use the remaining 5%.

3.1.4 Energy Conservation

Even though the PIC region is not a closed system, therefore mass and energy flow into and out of the region, it is important to check the energy variation during the simulation to make sure the PIC model does not suffer from numerical heating or cooling. The normalized energy changes are shown in Figure 3.2. Throughout the simulation, the total energy E_t variation is less than 3%. The small variation suggests that the numerical heating or cooling are insignificant. The initial condition for iPIC3D is under MHD equilibrium, but not necessarily under Vlasov equilibrium. The electromagnetic field energy E_{EM} and kinetic energy of each species normalized by the initial total energy are also shown in Figure 3.2. During the first several minutes, energy is transferred from the particles to the electromagnetic field. After 200s, the ion and electron energy decreases about 5%, while the electromagnetic field energy increases from 0.3 to about 0.36. This is the transition from the MHD steady state to a PIC preferred solution. Further changes of these energies are gradual and small. E_{EM} is mainly magnetic field energy, which is about 3 orders larger than electric field energy.

3.2 Results

3.2.1 Overview

The iPIC3D code is initialized from a steady Hall MHD state, which is shown in Figure 3.1. The steady state is obtained from the Hall MHD run by using a local time stepping scheme, and a reconnection X-line already exists near the equatorial plane along the dayside magnetopause. Since the local time stepping scheme is diffusive in this case, the reconnection signature near the X-line is weak, for example, the Hall magnetic field strength is only about 1 nT. The PIC code inherits the magnetic field topology and starts evolving based on Maxwell's equations and the motion of the macro-particles. An overview of the evolution of the dayside magnetopause is shown in Figure 3.3, which contains the Hall magnetic field B_y and the field lines at the meridional plane inside the PIC box. At $t = 70$ s, B_y has already increased to about 8 nT. The Hall field extends far away from the X-line with roughly the same field strength for each branch. 15s later, south of the existing reconnection point, another X-line starts to form at around $x = 10.2\,R_E$ and $z = -1\,R_E$. At $t = 145$ s, both X-lines can be seen clearly, and a flux rope like structure forms between the two X-lines. The top X-line has moved to about $z = 0.5\,R_E$. The bottom X-line is almost steady so far, but it will move southward later. At $t = 325$ s, the top and bottom X-lines reach about $z = 1.8\,R_E$ and $z = -3.5\,R_E$, respectively, and the center of the flux rope is moving southward with the bottom X-line. Since the flux rope is moving away from the top X-line, the current sheet between them becomes unstable and a secondary flux rope is generated (rightmost panel of Figure 3.3). During the one hour simulation, flux ropes form near the subsolar point and move toward poles quasi-periodically. More details about reconnection and flux ropes, both macroscopic and microscopic scales, are discussed in the following sub-sections.

3.2.2 Evolution of FETs

The meridional cut of the first two FTEs formed in the simulation are already shown in Figure 3.3. When we go beyond the 2D view, more complicated but completed structures arise. The flux ropes colored with the ion velocity z component u_{iz} at different times are shown in Figure 3.4. At $t = 100\,\mathrm{s}$, a short flux rope appears near the subsolar point. It is labeled as FTE-A. This flux rope extends from $y \sim -1\,R_E$ to $y \sim 1\,R_E$ in the dawn-dusk direction. It suggests that next to the primary X-line near $z = 0$, another X-line starts to form south of the subsolar point. We have checked a series of 2D $x - z$ plane cuts, and found that the signature of reconnection, like the ion jets, at the second X-line is clear at $y = 0$, but appears very weak far away from the Sun-Earth line, for example at $y = 0.78\,R_E$ or $y = -0.78\,R_E$. At $t = 150$ s, the flux rope has extended significantly in both dawn and dusk directions. Along the flux rope, the ion velocity varies. Close to the dusk side (positive y), the reconnection at the second X-line produces fast northward ion jet flow to slow down the southward flow from the primary X-line, so that the flux rope moves relatively slowly. Close to the dawn side (negative y), the reconnection at the second X-line is not strong enough to offset the southward flow ejected from the primary X-line. The varying ion velocity leads to an inclined flux rope. At $t = 240$ s, the flux rope is even more tilted because of the varying ambient ion jet velocity. A new small flux rope, FTE-B in Figure 3.4, is generated at $t = 320$ s above FTE-A. FTE-A bifurcates at $y \sim -2.5$ and the new branch extends along the dawn-northward direction. FTE-A keeps moving southward while FTE-B is growing. At $t = 540$ s, a large portion of FTE-A, except for the dawn part, already moves to the southern edge of the PIC domain ($z = -6$). FTE-B elongates significantly along the dawn-dusk direction. It is twisted at the dawn side so that the axial direction is almost parallel to the z-axis. At the dusk side, FTE-B connects to a newly formed flux rope FTE-C. At $t = 660$ s, FTE-B and FTE-C have merged and become indistinguishable. These 3D plots

suggest:1) flux ropes arise from multiple X-line reconnection and can grow in time along the dawn-dusk direction, 2) the pole-ward moving velocity varies along a flux rope and makes them tilted, and 3) two flux ropes can merge and form a new long rope.

Since the PIC code is two-way coupled with the MHD model, the flux ropes can smoothly move out of the PIC region. Figure 3.5 shows a series of j_y and field lines of FTE-A in the meridional plane after it leaves the PIC domain. FTE-A moves southward along the magnetopause after it is generated near the subsolar point. At $t = 600\,\mathrm{s}$, the flux rope is already close to the southern cusp. There is strong axial current $j_y \sim 0.02\mu\mathrm{A/m}^2$ near the center of the flux rope. As FTE-A moves toward the cusp, j_y inside the flux rope decreases in intensity, which indicates the dissipation of the magnetic helicity, as we can see at $t = 660\,\mathrm{s}$. When the FTE reaches the center of the cusp ($t = 720\,\mathrm{s}$), the field lines at the leading edge of the FTE and the cusp field lines are anti-parallel and creates a narrow and short current sheet with negative j_y around $x \sim 4\,R_E$ and $z \sim -9.5\,R_E$. The ion velocity u_{iz} at $x = 4\,R_E$ in Figure 3.6 shows a jump around $z = -9.5\,R_E$. The narrow current sheet and the velocity jump imply that reconnection occurs between the flux rope field lines and the cusp field lines. At $t = 840\,\mathrm{s}$, after FTE-A leaves the cusp, the signature of the flux rope becomes very weak: even though the magnetic field is still perturbed, the j_y component is close to zero near the center and no 'O' line can be found. Finally, the remnant of the flux rope completely disappears as it moves toward the tail. Here we show the dissipation of FTEs in the meridional plane. But FTEs were observed along the distant tail magnetopause ($x = -67\,R_E$) on the dusk flank (*Eastwood et al.*, 2012). One possibility to explain the conflict is that these survived FTEs may bypass the cusps and move along the flank from the dayside to tail magnetopause.

3.2.3 Magnetic Field Signature

Since the most widely used indicator of FTEs in satellite data is the magnetic field signature, we discuss how the flux rope magnetic field looks like along a virtual satellite trajectory. A series of meridional cuts are shown in Figure 3.7 to illustrate the magnetic field evolution. At $t = 290\,\mathrm{s}$, north of the FTE-A event, there is an X-line at about $z = 1\,R_E$ surrounded by the quadrupolar Hall magnetic field B_y. As expected, the two branches on the magnetosheath side with amplitude of ~ 30 nT are stronger than the other two on the magnetosphere side with amplitude of ~ 10 nT. Near the X-line, the magnetosheath and magnetosphere are separated by a current sheet accompanied with very weak magnetic field. 30 s later, another X-line near $z = 0$ arises, and an O line forms between the two X-lines. Around the edge of the O lines, the azimuthal component of the magnetic field grows, while the B_y component is still very weak just near the center. We note that the strong field on the magnetosheath side of the flux rope is mainly contributed by the B_z component because of the accumulation of the inflow magnetic field lines. The reconnection at the northern X-line is stronger than the southern one, so the ion jet around the O line is moving southward with a slow speed less than $100\,\mathrm{km/s}$. Inside the O line, the pressure starts increasing. 100 s later, the pressure at the center of the flux rope already reaches about 1.3 nPa while the core field is still small. At $t = 540\,\mathrm{s}$, the O line structure continues to grow as the two X-lines move northward and southward, respectively. We can see the core field B_y at the center of the O line has grown to a significant value of $\sim 30\,\mathrm{nT}$ now, while the center pressure drops to $\sim 1.0\,\mathrm{nPa}$. The converging jets from the two X-lines are comparable and the flux rope is almost steady. 180 s later, the core field grows to $\sim 40\,\mathrm{nT}$ and the corresponding pressure drops to about 0.8 nPa. The whole structure at this stage is moving northward driven by the ion jet generated by the southern X-line. To demonstrate the scaling factor has weak influence on the global structures, we perform another simulation with

ion inertial length increased by a factor of 32. The simulation results are shown in Figure 3.8. The FTE in Figure 3.8 shows similar dynamic process as the event in Figure 3.7: the core field grows gradually and the ion pressure is anti-correlated with the core field strength. The FTEs in Figure 3.8 and Figure 3.7 also have comparable sizes.

At the early time when the O line just formed, for example, at $t = 420\,\mathrm{s}$, the weak core field is surrounded by relatively large toroidal fields. We argue that this is an example of the so-called 'crater FTEs' that have been observed by spacecrafts (*LaBelle et al.*, 1987; *Zhang et al.*, 2010). Since the O line moves slowly during its initial stage of formation, the magnetic field observed at a fixed point can not reflect its global structure. Instead, the magnetic field along the magnetopause (the red curve in the left panel of Figure 3.9) is shown in the right panel of Figure 3.9 to illustrate its magnetic field structure. Along the magnetopause, from south to north, the B_x field, which is roughly normal to the magnetopause, reaches a local minimum of ~ -15 nT at $z = 0$ and then quickly increases to ~ 15 nT at $z = 1\,R_E$. The flux rope is bounded by the depressed magnetic field 'trenches' at $z = -0.2\,R_E$ and $z = 2\,R_E$ as indicated by B_t. The depression results from the low magnetic field strength inside the current sheet as can be seen from the right panel of Figure 3.9. B_t reaches local maximum at the same position of the B_x peaks ($z = 0\,R_E$ and $z = 1\,R_E$), while the field strength decreases to about 10 nT between the peaks. We refer to the event on 30 July 2007 observed and analyzed by *Zhang et al.* (2010) as a comparison. Figure 6 of *Zhang et al.* (2010) shows the magnetic field signature of this event. Even though the 30 July 2007 event has a large guide field (corresponding to B_y component in our simulation), and its magnetic field around the flux rope is more steady than our simulation, the whole structure of this event is similar to what is shown in Figure 3.9.

As the flux rope evolves, the core field strength grows to a significant value. The

magnetic field measured at a fixed position $x = 10.2\,R_E$, $z = 2.75\,R_E$ is shown in the right panel of Figure 3.10. The vertical dashed line at $t = 760\,\mathrm{s}$ represents the location of the maximum B_t. Around this time, the B_x field, which is roughly perpendicular to the magnetopause, jumps from ~ 5 nT to ~ -20 nT within about 25 s. At $t = 760\,\mathrm{s}$, both the axial field B_y and the total field B_t reach a maximum. These features match the signatures of an FTE with typical flux rope structure (*Zhang et al.*, 2010). During the one-hour long simulation, there are ten FTEs with significant core field moving across the southern PIC edge. The occurrence frequency is consistent with observations (*Rijnbeek et al.*, 1984) and previous MHD simulations (*Raeder*, 2006).

The IMF is purely southward in our simulation and there is no uniform background guide field at the magnetopause. But a significant core field can still arise during the FTE generation and evolution as seen in Figure 3.7. When a flux rope is still close to the X-lines, the core field may be encompassed by the Hall magnetic field generated by the reconnection, resulting in complicated guide field structure. The B_M field at $t = 540\,\mathrm{s}$ is shown in Figure 3.11. In order to compare with observations, the magnetic field has been transformed into a boundary normal coordinate system (**LMN**), in which the **N** component points outward, normal to the magnetopause, the **M** component is determined by $\mathbf{N} \times \mathbf{Z}_{GSM}$ and the **L** component completes the right-hand coordinate system. Since the plot is shown in the meridional plane, the $\mathbf{Y}_{GSM}$ direction is anti-parallel to the **M** direction. Around the flux rope center, the guide field B_M is negative, while the southern part of this flux rope is surrounded by positive B_M. The polarity of the positive 'Y' shape B_M is consistent with the Hall magnetic field generated by the X-line at $z = -1\,R_E$. If a satellite is moving across the flux rope along the red solid line in the left panel of Figure 3.11, the satellite will observe a tripolar guide field structure (right panel of Figure 3.11). Similar structure was first observed in the solar wind (*Eriksson et al.*, 2015), and then it was observed

by the Polar satellite at the magnetopause (see Figure 1 of *Eriksson et al.* (2016)). The Polar event shows a large negative B_M core field bounded by two narrow B_M depressions in the presence of a large background guide field. There is no background guide field in our simulation and thus the right panel of Figure 3.11 shows a pure tripolar structure: the large negative B_M field is surrounded by two relative small positive peaks. Despite the difference in the background guide field, the topology of B_M obtained from our simulation is very similar to the Polar observation.

3.2.4 Kinetic Features

We have examined the global structure of the FTEs in the previous discussion. In this subsection, we will demonstrate that the underlying kinetic physics is properly captured by our model. The Larmor electric field, identified by *Malakit et al.* (2013), is a localized electric field that appears on the magnetospheric side of the dayside reconnection site. The x-component of the electric field E_x at the end of the simulation (t=3600s) is shown in Figure 3.12. The positive E_x pointing towards the Sun along the magnetopause is the Hall electric field, while behind the Hall electric field, the localized negative field pointing towards the Earth is the Larmor electric field. A 1D cut through the reconnection site along the x direction is also shown in Figure 3.12. The Larmor field strength is -3 mV/m, the magnetospheric side ambient field is about 2 mV/m, and the nearby Hall field is about 12 mV/m. These values are reasonably close to the MMS observation by *Graham et al.* (2016): the Hall electric field strength is $\sim 20\,\mathrm{mV/m}$ and the Larmor field strength is about 10 mV/m (see Figure 2 of *Graham et al.* (2016)).

Even though the ion inertial length is scaled up by a factor of 16 in the present simulation, the electric field strength is not sensitive to the scaling factor. Ignoring

the electron inertia term, the generalized Ohm's is:

$$\mathbf{E} = -\mathbf{u_i} \times \mathbf{B} + \frac{1}{q_i n_i}\mathbf{j} \times \mathbf{B} - \frac{1}{q_i n_i}\nabla p_e = -\mathbf{u_e} \times \mathbf{B} - \frac{1}{q_i n_i}\nabla p_e \tag{3.4}$$

Tóth et al. (2017, submitted paper) shows the electron velocity $\mathbf{u_e}$ of the current sheet does not change with the scaling factor while the current sheet width scales. The gradient of electron pressure is inversely proportional to the scaling factor, because the pressure jump is fixed across the current sheet and the current sheet width is proportional to the scaling factor. Since the charge per ion or electron is also reduced by the same factor, the scaling does not change the electric field strength. Besides the scaling of the ion inertial length, a reduced ion-electron mass ratio $m_i/m_e = 100$ is used in this study to increase electron kinetic scales (see section 3.1.2). The influence of the mass ratio m_i/m_e has been studied in numerous papers (*Shay and Drake*, 1998; *Hesse et al.*, 1999; *Ricci et al.*, 2004; *Shay et al.*, 2007; *Lapenta et al.*, 2010). For the Larmor electric field , *Malakit et al.* (2013) specifically estimates its amplitude to be:

$$E \sim \frac{k_B T_i}{q_i r_i} \tag{3.5}$$

where k_B is the Boltzmann's constant, T_i, q_i and r_i are the temperature, charge per ion and ion Larmor radius of the ions on the magnetospheric side. In the simulation, q_i reduces by a factor of 16 and r_i becomes 16 times larger compared to the realistic situation, while the temperature T_i does not change. So, the scaling of inertial length should not influence the strength of the Larmor electric field. On the magnetosheath side, our simulation shows the ion temperature is about $2 \times 10^6\,K$, magnetic field strength is about 60 nT. Substituting these values into Eq. 3.5 gives $E \sim 5.5\,\mathrm{nT}$. As mentioned above, the value obtained from simulation is about -3 mV/m.

The crescent shape electron phase space distribution has been observed near

the electron diffusion region at the dayside magnetopause by MMS (*Burch et al.*, 2016). The same distribution is also found in our 3D global simulation. The phase space distribution of electrons inside a cube region: $10.27\,R_E < x < 10.33\,R_E$, $-0.3\,R_E < y < 0.3\,R_E$ and $-2.1\,R_E < z < -1.9\,R_E$ is shown in Figure 3.12. The crescent distribution is found in the $V_y - V_x$ plane, corresponding to the two velocity components perpendicular to the magnetic field. The crescent hot electrons are drifting along negative y direction with a speed close to 3000 km/s. The direction of the flow is consistent with the $\mathbf{E} \times \mathbf{B}$ direction, and the velocity of the crescent particles is very close to the MMS observation (*Burch et al.*, 2016). Slightly further away from the reconnection site, where the Larmor field appears, inside a cube $10.08\,R_E < x < 10.14\,R_E$, $-0.3\,R_E < y < 0.3\,R_E$ and $-2.1\,R_E < z < -1.9\,R_E$, the ion phase space distribution also presents crescent like shape as it is shown in Figure 3.12(c). The crescent ions drift in positive y direction because E_x is negative. We also checked the distributions for particles inside the current sheet but far from the reconnection site, and no crescent distributions are found for either electrons or ions.

Kinetic effects along the magnetopause current direction are also captured by our 3D MHD-EPIC model. Figure 3.13 shows the fully developed lower hybrid drift instability (LHDI) at the end of the simulation (t=3600 s) at the $z = -3\,R_E$ plane. The electric field E_M shown in Figure 3.13 is the $\mathbf{M}$ component in the boundary normal coordinates, and $\mathbf{M}$ is anti-parallel to the current direction. The black curve in Figure 3.13 separates the negative and positive B_z. We can see the LHDI appears along the magnetopause on the magnetospheric side. A closer view of E_M, as well as B_z, ion mass density ρ_i and electron velocity u_{ey} are also shown Figure 3.13. It is clear to see the LHDI arising near the interface of magnetosheath and magnetosphere, where there is a sharp density gradient. B_z, ρ_i and u_{ey} show sawtooth pattern at the same location. The amplitude of the LHDI electric field is about 8 mV/m, which

is consistent with MMS observation (*Graham et al.*, 2016). The dominant wave length shown in Figure 3.13(b) is about $0.38\,R_E$, and the ambient magnetosheath side electron gyroradius is about $r_e = 0.025\,R_E$ with the artificially changed charge per electron mass ratio, which results in $kr_e \sim 0.4$, where $r_e = m_e v_e/(q_e B)$ and v_e is defined as $v_e = \sqrt{2T_e/m_e}$. The value of kr_e is also consistent with observation (*Graham et al.*, 2016) and theory (*Daughton*, 2003). LHDI at different time and different location is analyzed, the value of kr_e varies from ~ 0.3 to ~ 0.5, and $kr_e \sim 0.4$ is a typical value. Similar as the argument above with the Ohm's law, the electric field strength is not sensitive to the scaling, that is why the LHDI electric field strength agrees with MMS observations. But the length scale does change with the scaling. The charge per mass of electron q_e/m_e is artificially increased by a factor of 294 in the simulation, and the electron thermal velocity reduces by a factor of $\sqrt{18.36} = 4.3$ for $m_i/m_e = 100$. The magnetic field is realistic, hence the electron gyroradius is about 68 times larger than in reality. If we scale back the LHDI wavelength of the simulation by the same factor, it will be ~ 35 km. As a comparison, MMS observed 10km $\sim$ 13km wavelength (*Graham et al.*, 2016). Figure 3.13(f) shows the isosurfaces of $E_M = 4$ mV/m colored by the ion velocity u_{iz} viewed from the Sun. Along the magnetic field direction, the isosurfaces are cut off two or three times. The ion velocity jumps or even change directions across a cut-off region. It suggests these cut-off regions corresponding to the reconnection sites and the LHDI electric field is weak near the diffusion regions (*Pritchett*, 2013).

3.2.5 Comparison with Hall MHD

For comparison, we also run a pure Hall MHD simulation with the same setup except the PIC region is removed and the MHD grid resolution around the day-side magnetopause is refined to $1/32\,R_E$, which is the resolution used by PIC in the MHD-EPIC run. Even for Hall MHD, resolving the ion inertial length is necessary

in order to capture the Hall effect correctly. Due to the small kinetic scale inside the magnetosheath, scaling the ion inertial length is also required for a global Hall MHD simulation since Hall MHD is also computationally expensive as we will see. We note that the ion inertial length in the pure Hall MHD simulation is also scaled up by a factor of 16 so it can be resolved by $1/32\,R_E$ cell. Hall MHD is reasonably optimized by using semi-implicit scheme to overcome the time step imposed by the whistler mode wave and speed up the simulation. It still takes 6400 cores running about 67 hours to model one hour because of the high resolution and the stiffness of the Hall term. As a comparison, the MHD-EPIC simulation (170 hours on 6400 cores) is about 2.5 times more expensive. Hall MHD produces the Hall magnetic field near the X-line and generates flux ropes in a way similar to MHD-EPIC. But Hall MHD can not reproduce the kinetic features, neither the crescent particle distributions nor the LHDI.

3.3 Summary

We have performed a one-hour long high-resolution global simulation with the MHD-EPIC model to study dayside reconnection and FTEs. Our simulation is the first attempt to investigate the FTEs and reconnection with kinetic physics resolved in a realistic magnetopause environment. Although the kinetic scale is artificially increased to reduce the computational cost, the model captures the kinetic features very well. MMS observations, like the crescent particle phase space distribution and LHDI, are reproduced in our model. The FTEs from the simulation also agree well with spacecraft observations. The key results from the present simulation are:

- When an FTE arises, its cross section is small and it is short in the dawn-dusk direction. During its growth, the cross section increases and the FTE extends

along the dawn-dusk direction.

- An FTE forms near the subsolar point and moves toward the poles under steady southward IMF conditions. When the FTE reaches the cusp, reconnection happens between the FTE magnetic field and the cusp magnetic field lines, thus dissipating the FTE. The signature of FTE is weak behind the cusps.

- FTE is flanked by two reconnection sites during its formation, and the converging ion jets around the FTE are found.

- The present simulation confirms that the 'crater FTEs' magnetic field signature can be found at the early stage of an FTE formation when the axial magnetic field is still weak. A strong core field may develop as the FTE evolves, and the Hall magnetic field may provides the initial seed core field. Therefore a fully developed FTE has the typical strong core field structure.

- A tripolar guide field structure is found from our simulation.

- The Larmor electric field is found near the reconnection site on the magnetospheric side, and its amplitude is about -3 mV/m.

- A crescent electron phase space distribution is found near the reconnection site where the Hall electric field reaches its maximum. A similar distribution is also found for ions at the place where the Larmor electric field appears.

- The lower hybrid drift instability (LHDI) appears at the interface of the magnetosheath plasma and magnetosphere plasma. The LHDI electric field peak strength is about 8 mV/m, and a typical ratio between its wavelength and the electron gyroradius is about $kr_e \sim 0.4$. The simulation agrees with the MMS observations and theory.

Compared to the models relying on ad hoc resistivity or numerical resistivity to generate FTEs or investigate reconnection process, our 3D MHD-EPIC model makes

one significant step forward by incorporating a self-consistent kinetic description of reconnection into a global MHD model. While the kinetic scales are increased by artificially reducing the charge per mass for both ions and electrons, all the other parameters are realistic. The scaling changes the size of kinetic features, for example the wavelength of LHDI, but other values, like the strength of Larmor electric field or LHDI electric field, are not modified by the scaling. Another artificial change is the solar wind electron pressure. It is set to a value 8 times larger than the ion pressure so that $p/p_e \sim 2.5$ inside the magnetosheath while the ratio is usually about $4 \sim 12$ from observation (*Wang et al.*, 2012). The artificially increased electron pressure can help to stabilize the simulation, and it does not deviate significantly from the observed values. We plan to improve this in the future studies.

The MHD-EPIC model offers a powerful tool to study magnetospheric physics. The PIC code only covers the dayside magnetopause in the present simulation. As a natural extension, it can be elongated to cover the bow shock so that the kinetic processes associated with the bow shock can be modeled. Another future application is covering the tail reconnection site with another PIC region, so that both dayside and tail reconnections are handled by a kinetic code and we can study substorm in a more realistic way.

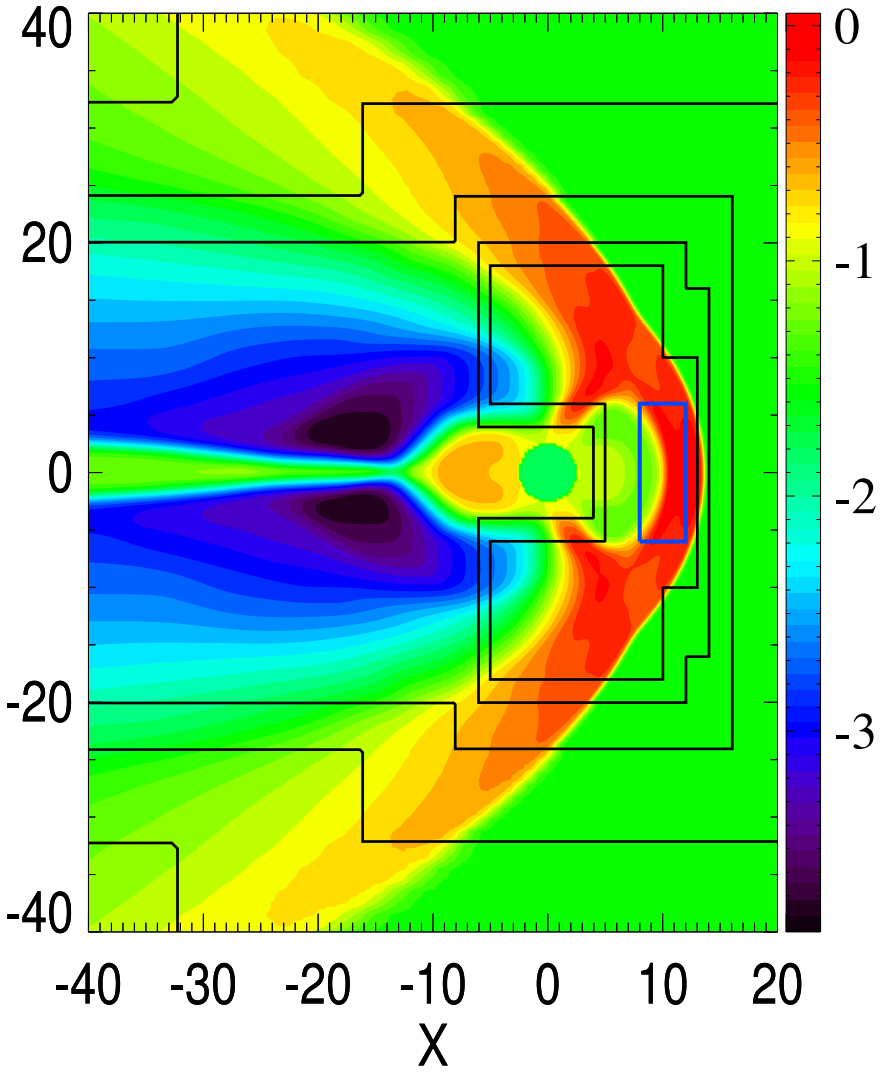

Figure 3.1: Part of the meridional plane with the adaptive MHD grid and the PIC region. The color represents the plasma pressure on a logarithmic scale. The black lines represent the refinement level, where the cell size changes. The resolution of the finest level around the dayside magnetopause is $1/16\,R_E$, and the refinement ratio between two nearby levels is 2. The blue box ($8\,R_E < x < 12\,R_E$, $-6\,R_E < z < 6\,R_E$) is the edge of the PIC region covered by iPIC3D, and it extends from $-6\,R_E$ to $6\,R_E$ in the y direction.

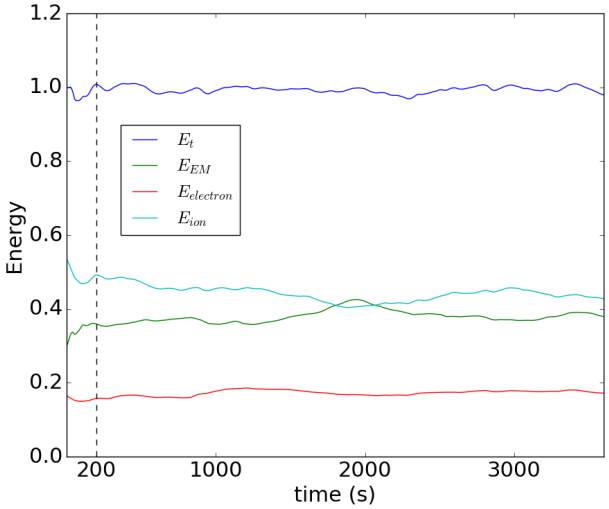

Figure 3.2: The normalized the total energy E_t, electric field and magnetic field energy E_{EM}, ion energy E_{ion} and electron energy $E_{electron}$. They are normalized by the initial total energy.

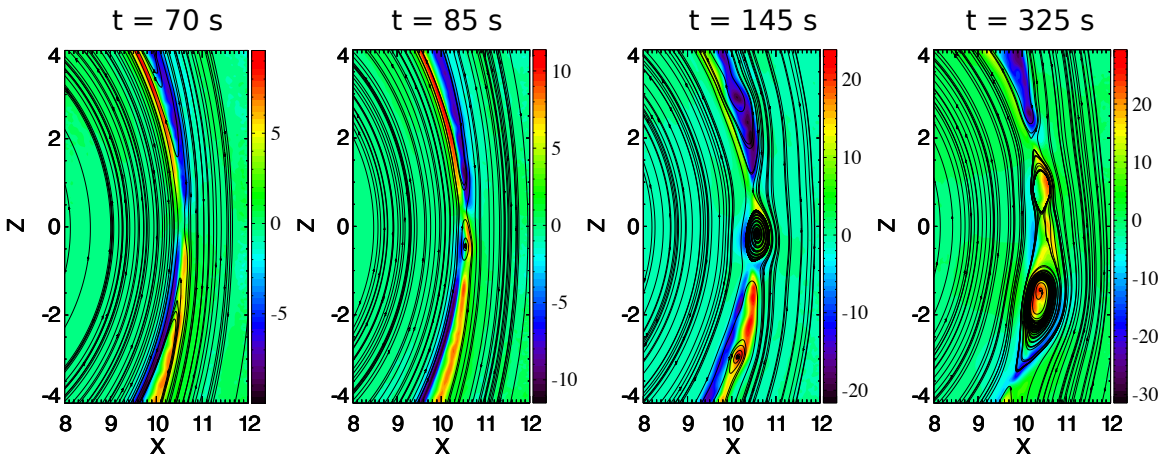

Figure 3.3: A series of snapshots showing B_y strength and the projected magnetic field lines in the meridional plane inside the PIC region. The color bar is different in each plot.

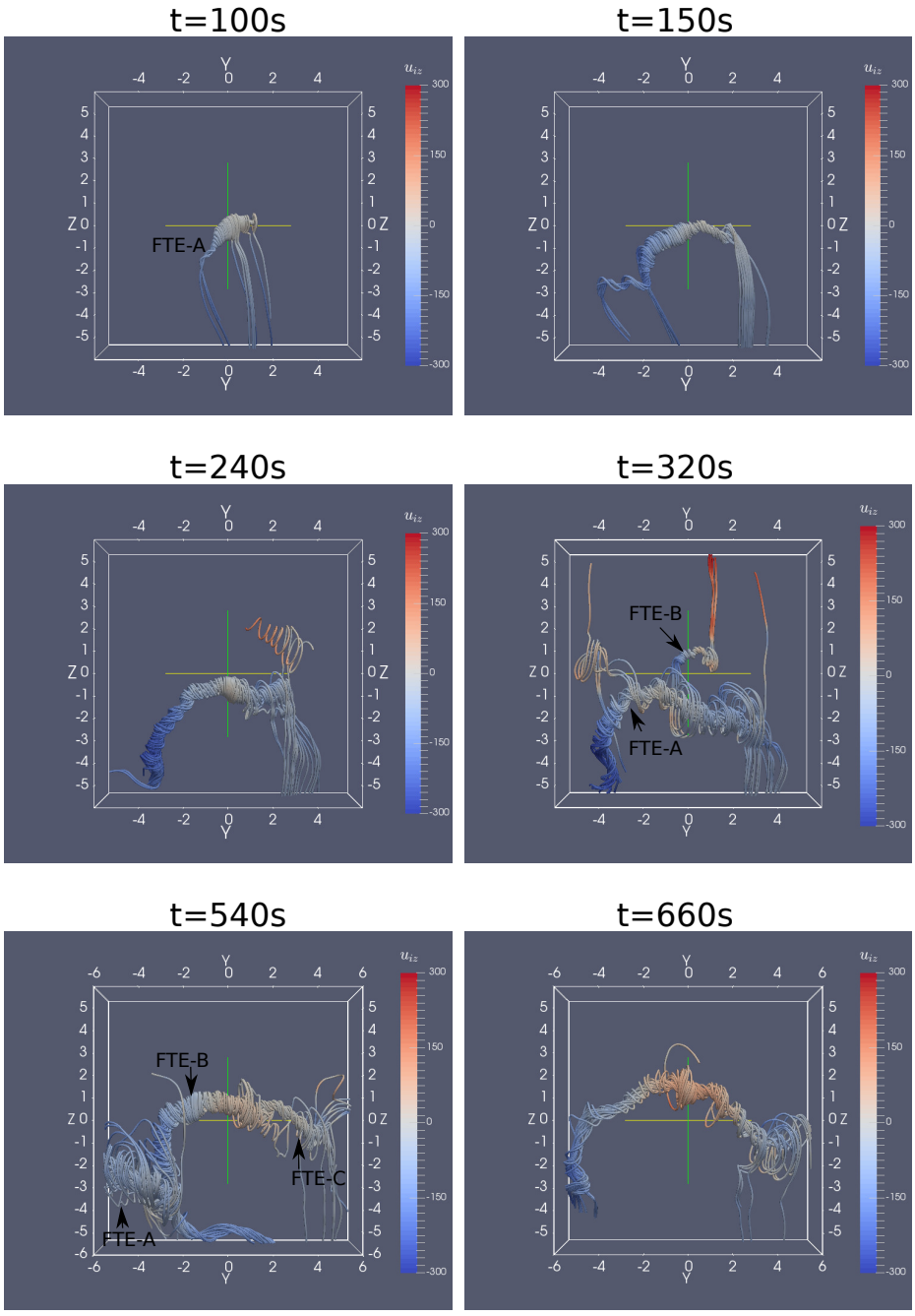

Figure 3.4: The evolution of FTEs. Viewed from the Sun, a series of snapshots with magnetic field lines colored by ion velocity u_{iz}[km/s] are shown.

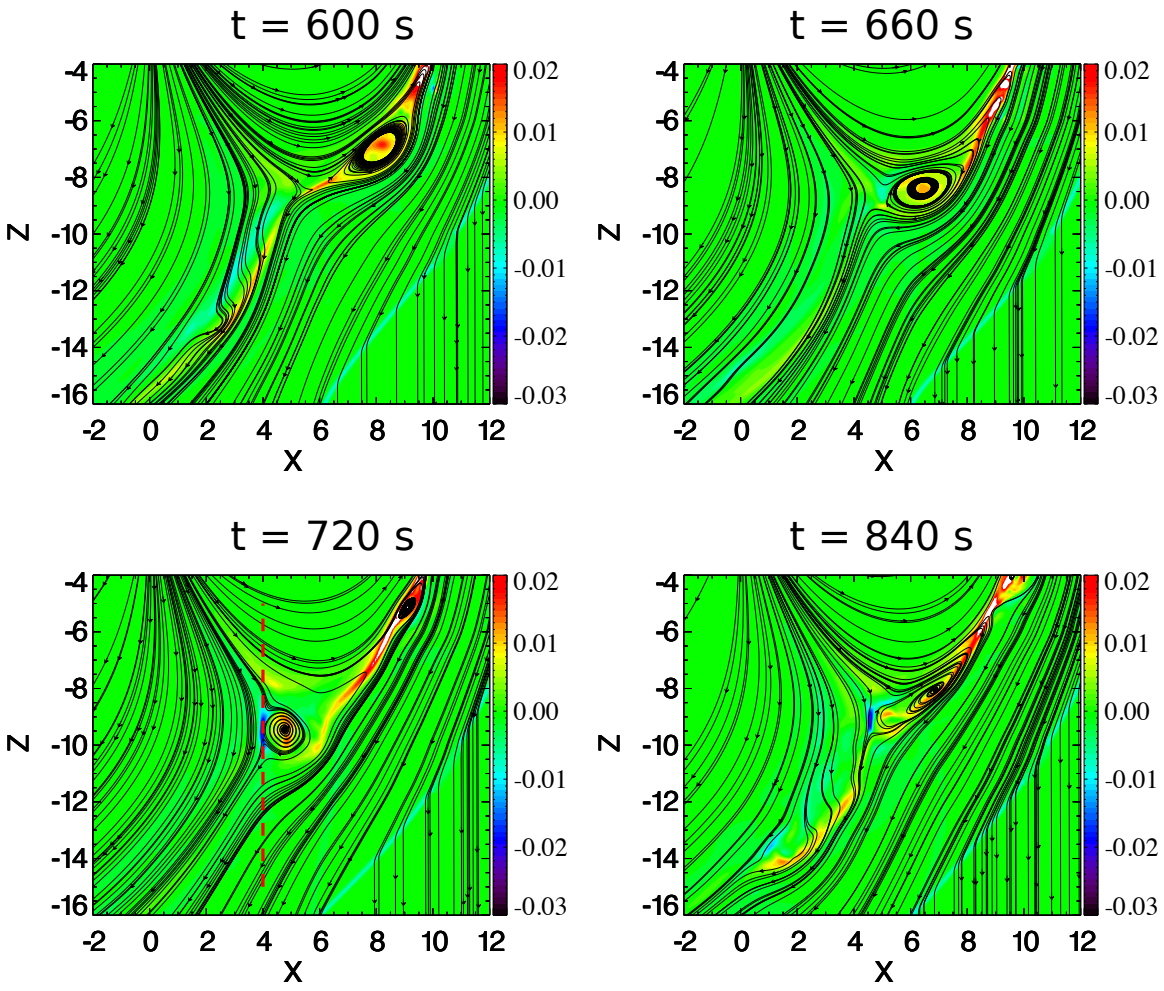

Figure 3.5: The FTE dissipation when it is crossing the southern cusp. A series of snapshots of current density $j_y[\mu\mathrm{A/m}^2]$ and field lines are shown. The plots are obtained from MHD output. Along the FTE's trajectory, the grid is uniform and the cell size is $1/16\,R_E$. The red dashed line indicates the cut used in Figure 3.6

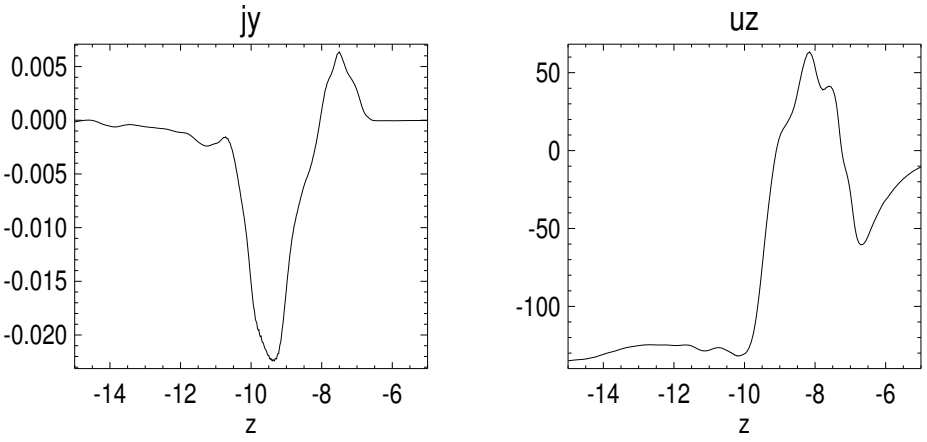

Figure 3.6: $j_y[\mu\mathrm{A/m}^2]$ and u_z[km/s] along the vertical red dashed line marked in Figure 3.5. The jump of u_z around $z \sim -9\,R_E$ implies the occurrence of magnetic reconnection.

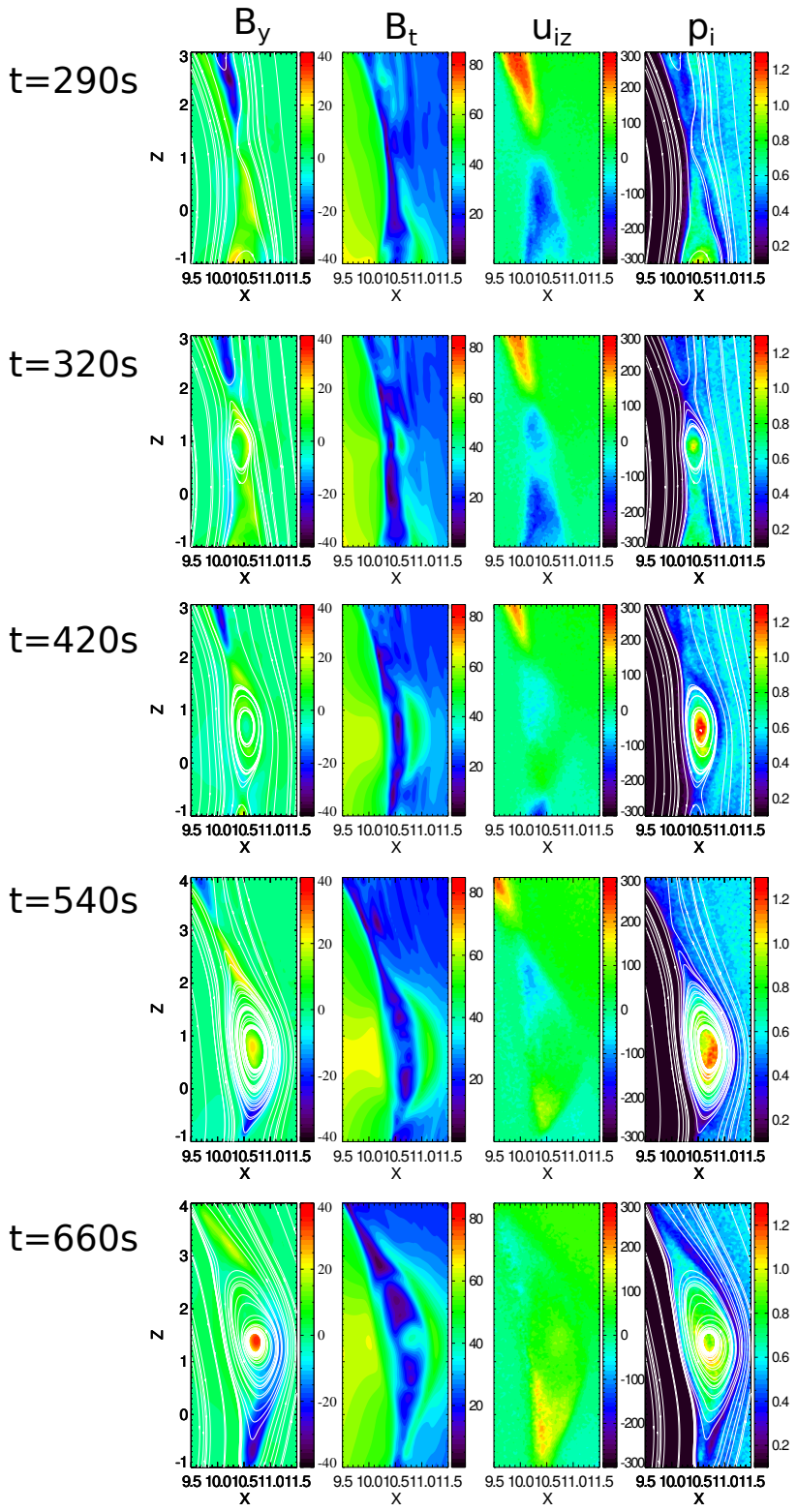

Figure 3.7: The evolution of FTEs in the meridional plane. From left to right, the four columns show the B_y[nT] and the projected magnetic field lines; the field strength B_t[nT]; the ion velocity in z direction U_{iz}[km/s]; and the ion pressure p_i[nPa] overlapped with magnetic field lines.

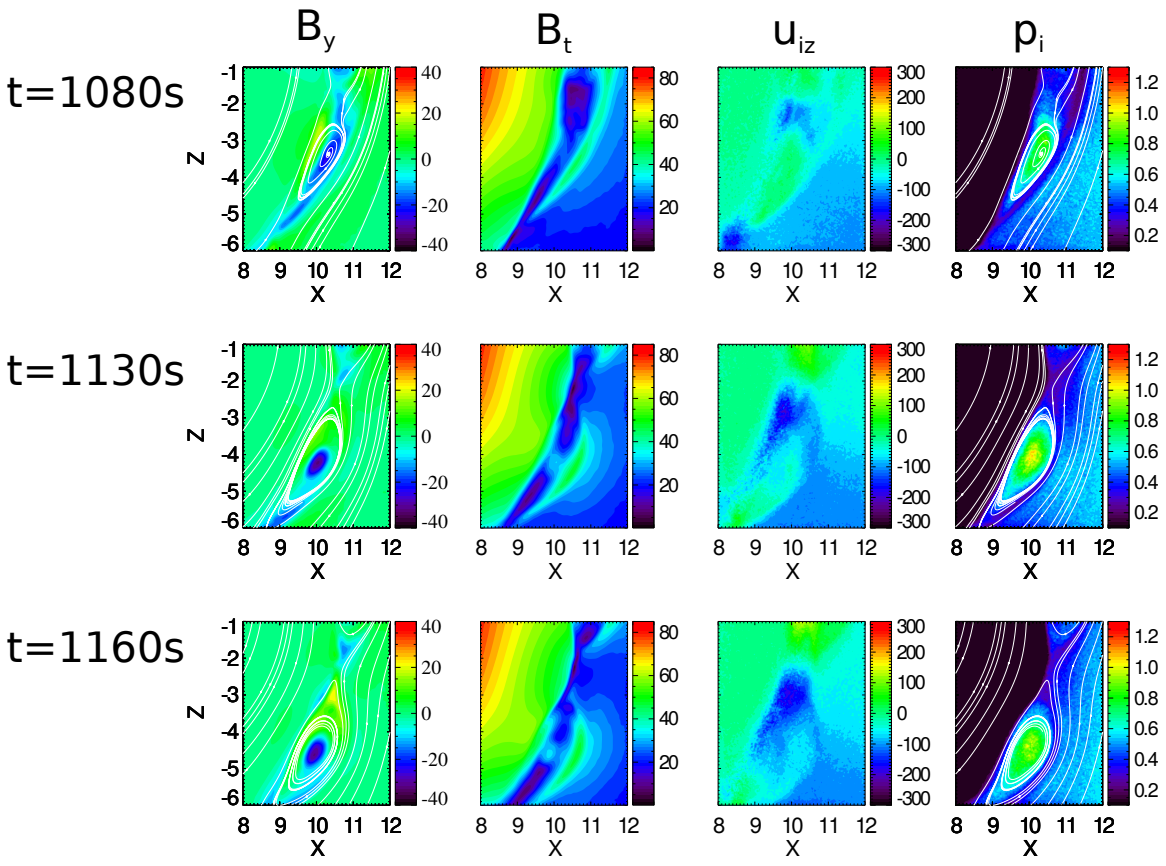

Figure 3.8: The same variables as Figure 3.7 are shown. But these plots are created from a simulation with the ion inertial length scaled up by a factor of 32.

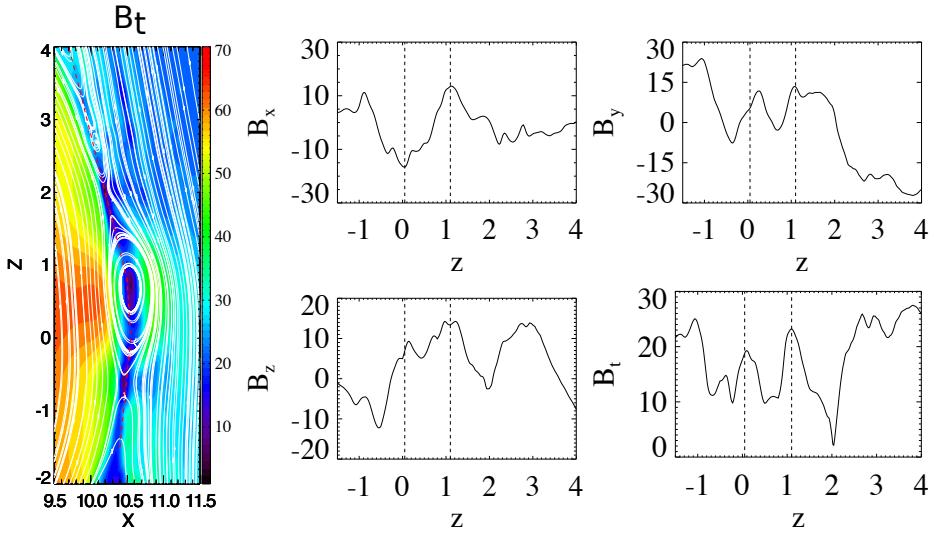

Figure 3.9: The crater flux rope at $t = 420\,\mathrm{s}$. The left panel shows the magnetic field strength and field lines. The right four plots show the magnetic field along the red dashed line in the left panel. The two vertical dashed lines represent the two peaks of B_x.

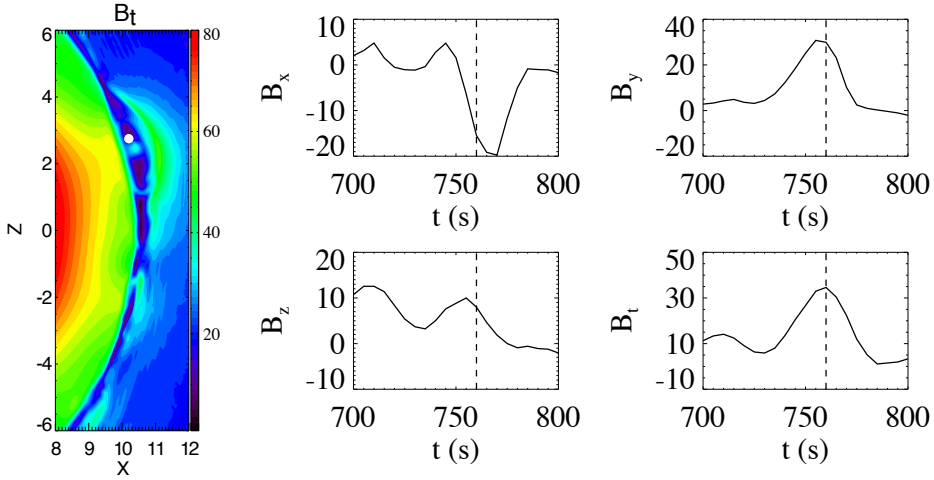

Figure 3.10: The magnetic field signature of a flux rope with significant core field. The left panel is the magnetic field strength at $t = 740\,\mathrm{s}$. The white filled circle at $x = 10.2\,R_E$, $z = 2.75\,R_E$ is the location of the steady virtual satellite. The right panels show the magnetic field observed by the satellite. The vertical dashed line at $t = 760\,\mathrm{s}$ indicates the location of maximum B_t.

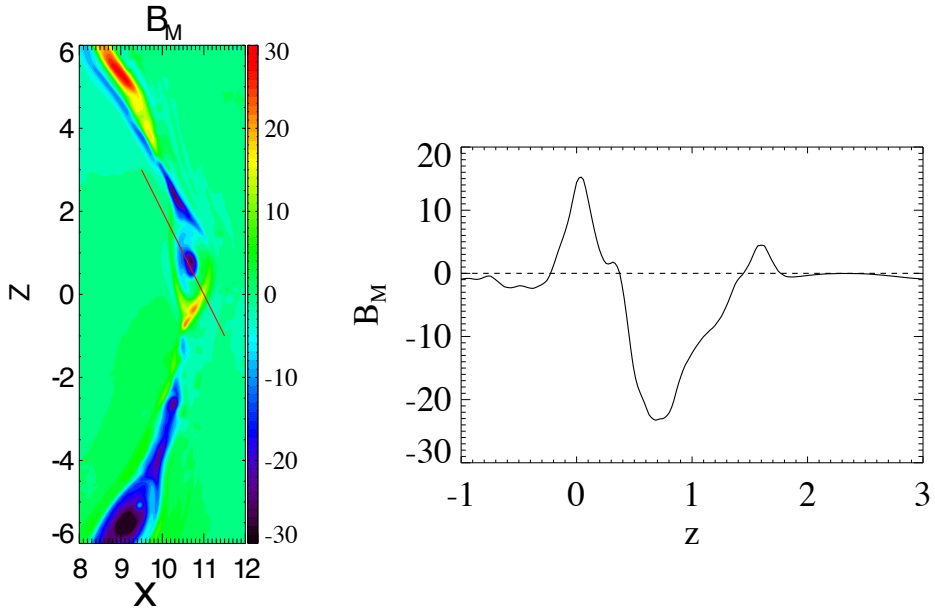

Figure 3.11: The tripolar guide field structure. The left panel shows the B_M component in the meridional plane at $t = 540\,\mathrm{s}$. Around the flux rope center, the guide field is negative, while the southern part of this flux rope is surrounded by the 'Y' shaped positive B_M. The field along the red solid line is shown in the right panel.

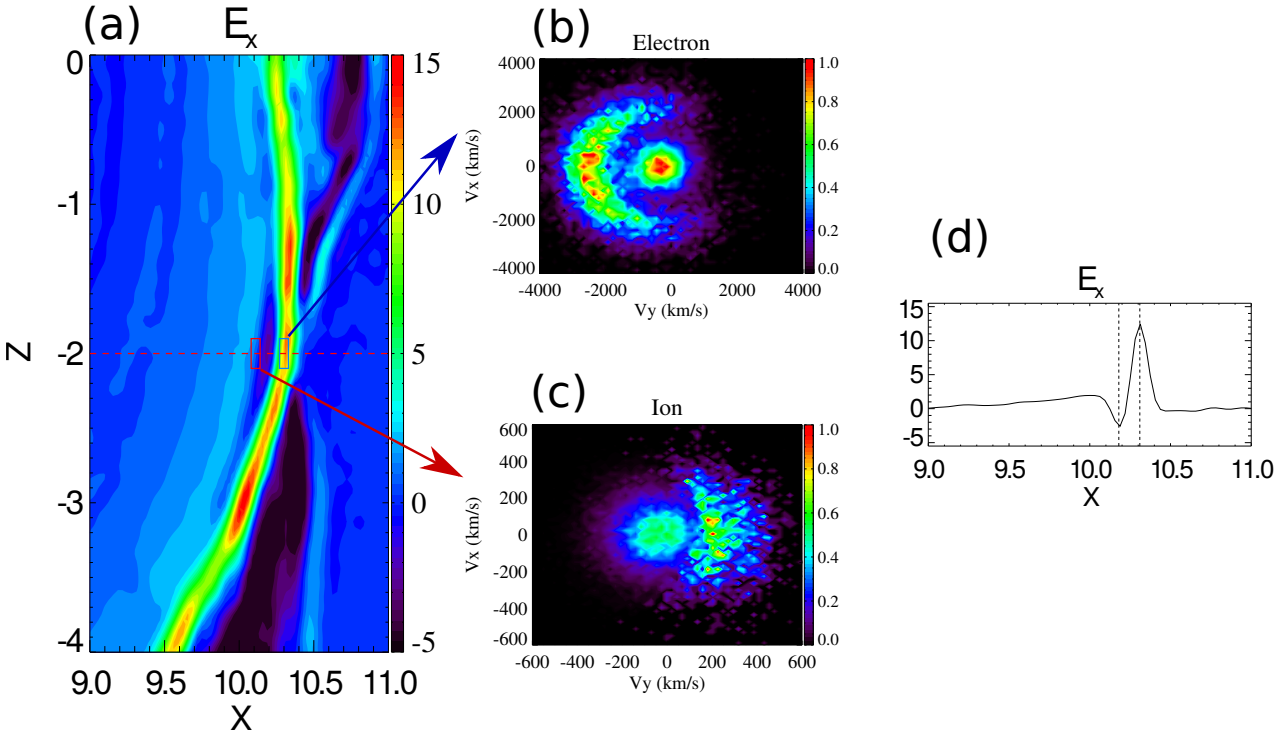

Figure 3.12: The Larmor electric field and crescent electron and ion phase space distributions. (a) E_x[mV/m] in the meridional plane at $t = 3600\,\mathrm{s}$. (b) The normalized electron distribution in $V_y - V_x$ phase space. The electrons are inside the blue box shown in (a): $10.27\,R_E < x < 10.33\,R_E, -0.3\,R_E < y < 0.3\,R_E, -2.1\,R_E < z < -1.9\,R_E$. (c) Ion phase space distribution for particles inside the red box in (a):$10.08\,R_E < x < 10.14\,R_E, -0.3\,R_E < y < 0.3\,R_E, -2.1\,R_E < z < -1.9\,R_E$. The phase density is normalized. (d) E_x along the red dashed line in panel (a).

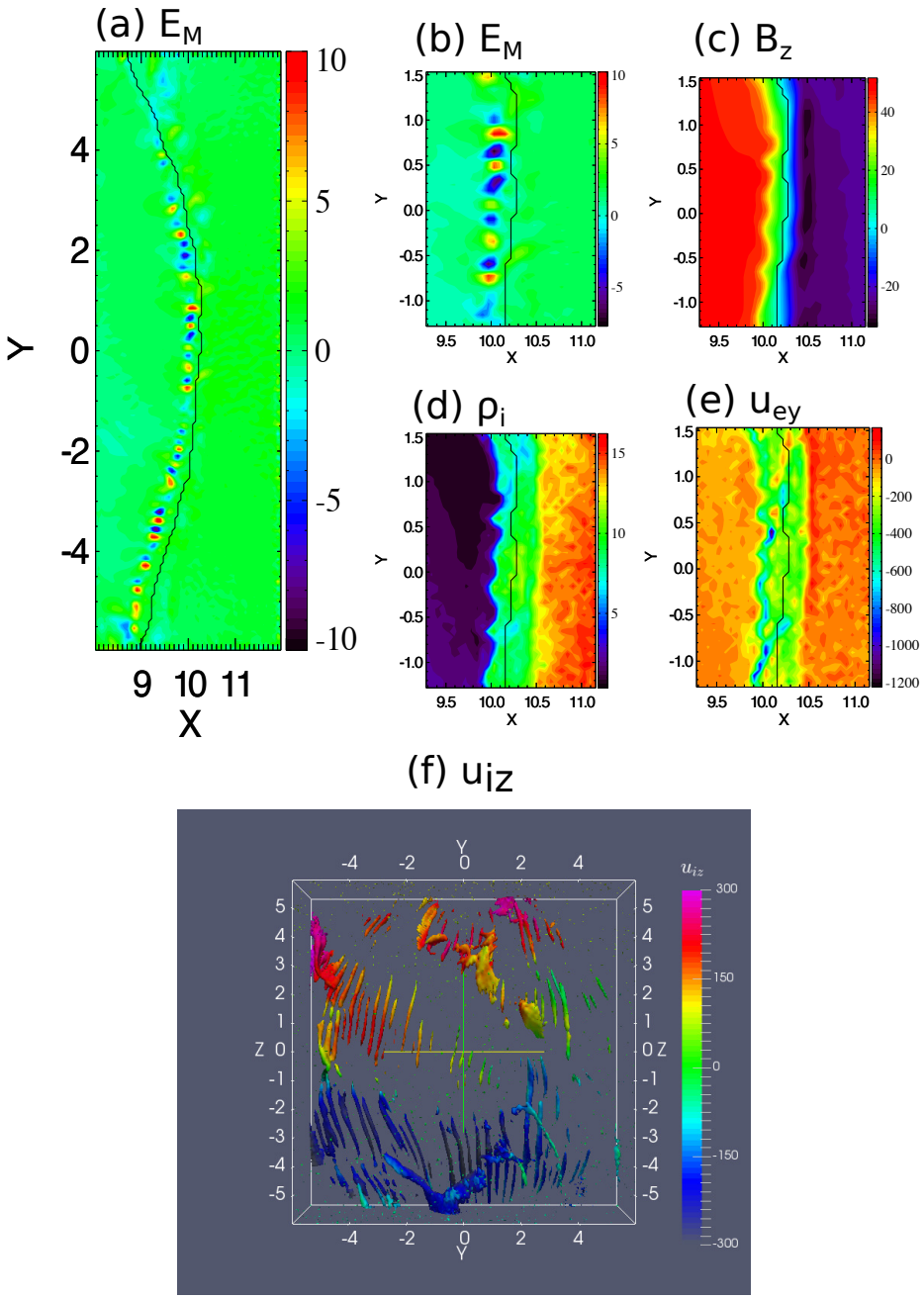

Figure 3.13: The Low hybrid drift instability (LHDI) at $t = 3600\,\mathrm{s}$. (a) Electric field E_M[mV/m] along the direction that is anti-parallel to the magnetopause current direction in the $z = -3\,R_E$ plane. Near $y = 0$, the current direction is almost parallel to the y direction. (b)-(e): zoom-in of different variables for LHDI at $z = -3\,R_E$. (c) is the B_z field in nT, (d) is the ion density in amu/cm^3 and (e) is the electron velocity along y direction. The black curves in (a)-(e) separate the negative and positive B_z. (f) The 3D contour surface of $E_M = 4$ mV/m colored by the ion velocity along the z direction (u_{iz}[km/s]).

CHAPTER IV

Magnetohydrodynamics with Embedded Particle-in-Cell Simulation of Mercury's magnetotail reconnection

BATS-R-US was the first MHD model applied for 3D global simulation of Mercury's magnetosphere (*Kabin et al.*, 2000, 2008). *Kabin et al.* (2000) studied the global structure of Mercury's magnetosphere and found the dayside magnetopause can be eroded to very low altitude with solar wind conditions of high ram pressure. *Jia et al.* (2015) developed the resistive body capability for BATS-R-US and studied how the induction effect arising from the conducting core affects the magnetospheric global response to the varying solar wind conditions. The dominant heavy ion Na^+, which has number density about 10% of the H^+ density in the plasma sheet, may have remarkable influence on the structure and dynamics of the magnetosphere, so the multi-fluid MHD models that treat Na^+ as a separate fluid have also been used for Mercury's magnetosphere simulations (*Kidder et al.*, 2008). Hybrid models, which treat the electrons as a massless charged fluid, while model the ions as particles, have also been used for global simulations (*Kallio and Janhunen*, 2003; *Wang et al.*, 2010; *Müller et al.*, 2012). Due to the limitation of the physics capability and grid resolution of these simulations, the magnetotail reconnection and tail flux ropes have not been

studied in detail. Thanks to the new model MHD-EPIC, we can use the PIC code to cover the tail region around the near Mercury neutral line (NMNL) and study the dynamics of the tail reconnection and the properties of the flux ropes.

4.1 Simulation Setup

During our MHD-EPIC simulation of Mercury's magnetosphere, we run the MHD code BATS-R-US first to reach a steady state, then couple the MHD model with the PIC code iPIC3D. The simulation setup for both BATS-R-US and iPIC3D is described in the following subsections.

4.1.1 MHD Model

Following the work of *Jia et al.* (2015), a resistive body with finite conductivity layer is used to mimic the interior structure of Mercury: the region within $r < 0.8\,R_M$ is the highly conducting core, and the layer between $0.8\,R_M$ and $1\,R_M$ with finite conductivity represents the mantle. The conductivity inside the mantle is set to $\sim 10^{-7}\,S/m$. We refer to *Jia et al.* (2015) for more details about the profile of the conductivity. The Hall effect and the electron pressure gradient term are also included in Ohm's law for the simulations presented here:

$$\mathbf{E} = -\mathbf{u} \times \mathbf{B} + \frac{\mathbf{J} \times \mathbf{B}}{q_e n_e} - \frac{\nabla p_e}{q_e n_e} + \eta \mathbf{J} \tag{4.1}$$

where q_e, n_e and p_e are the charge per electron, electron number density and electron pressure, respectively. η represents the resistivity, which is the inverse of the conductivity. The electron pressure is obtained from:

$$\frac{\partial p_e}{\partial t} + \nabla \cdot (p_e \mathbf{u}_e) = (\gamma - 1)(-p_e \nabla \cdot \mathbf{u}_e) \tag{4.2}$$

where $\gamma = 5/3$ is the adiabatic index, and $\mathbf{u_e} = \mathbf{u} - \mathbf{J}/(q_e n_e)$ is the electron velocity. In summary, resistive Hall MHD equations with separate electron pressure equation are solved in our MHD model. Inside the mantle region ($0.8\,R_M < r < 1\,R_M$), there is no plasma flow, but the magnetic field can still change due to the finite conductivity. So only the reduced Faradays law is solved inside the mantle:

$$\frac{\partial \mathbf{B}}{\partial t} = -\nabla \times (\eta \mathbf{J}), \tag{4.3}$$

where $\mathbf{J} = \frac{1}{\mu_0}\nabla \times \mathbf{B}$. Outside the planet surface, the whole set of equations are solved. Since both the Hall term and the resistivity term are stiff, a semi-implicit scheme (*Tóth et al.*, 2012) is used to speed up the simulation: the equations excluding the stiff terms are solved explicitly first, then solve the stiff terms with an implicit solver.

The whole simulation domain is a cube of $-64\,R_M < x < 24\,R_M$, $-32\,R_M < y, z < 32\,R_M$. The center of Mercury coincides with the origin of the coordinates. A dipole field with strength of 200 nT at the magnetic equator is used. The dipole axis is aligned with the z axis but the dipole center is shifted northward by $0.2\,R_M$. A stretched locally refined spherical grid is used. The tail region is refined so that the cell size is about $0.02R_M$ near $x = -2R_M$. The plasma density in the lobes is about $0.5\,\mathrm{amu/cm^3}$, and the corresponding ion inertial length is about 300 km or $0.13\,R_M$. The Hall effect can be well resolved because one inertial length is covered by ~ 6 cells. The inner boundary condition for the magnetic field is set at the interface of the mantle and the conducting core $r = 0.8\,R_M$, where the magnetic field is fixed due to the high conductivity. Since there is no plasma flow inside the surface, the inner boundary for plasma density, velocity and pressure is at the surface $r = 1.0\,R_M$. A zero gradient boundary condition is applied to plasma density and pressure. The boundary condition for velocity is set in a way that the plasma can be absorbed by

the surface, and the surface is not an important source of plasma. If the velocity in the cell just above the surface is outflow, then the radial component of the velocity is set to zero and we keep the tangential component. If there is inflow, the zero gradient boundary condition is applied for all components of velocity. The plasma can flow around the surface or flow into the surface, but it cannot have a significant outflow component near the surface.

Three simulations with different interplanetary magnetic field (IMF) are presented in this chapter (see Table 4.1). The average IMF (*Slavin et al.*, 2009; *Jia et al.*, 2015) is used for case-1. A purely southward IMF is used for case-2 so that the IMF is symmetric in the y direction. The B_x component is eliminated for case-3 but it has a large B_y component. The IMF strength and the solar wind plasma properties, including the density, velocity and pressure, are the same for these three simulations, as shown in Table 4.1.

Table 4.1: The solar wind conditions for three simulations

	B	ρ	**u**	p_i	p_e
case-1	(-15.21,8.4,-8.51) nT	40 amu/cm^3	(-400,0,0) km/s	0.048 nPa	0.048 nPa
case-2	(0,0,-19.35) nT	40 amu/cm^3	(-400,0,0) km/s	0.048 nPa	0.048 nPa
case-3	(0,17.38,-8.51) nT	40 amu/cm^3	(-400,0,0) km/s	0.048 nPa	0.048 nPa

4.1.2 PIC Parameters

MESSENGER observations suggest that the near Mercury neutral line (NMNL) is around $x = -2\,R_M$. To study the magnetic reconnection, the region around the NMNL is covered by the PIC code: $-4.2\,R_M < x < -1.2\,R_M$, $-1.5\,R_M < y < 1.5\,R_M$ and $-1\,R_M < z < 1.5\,R_M$ (see Figure 4.1). The cell size is $1/64\,R_M$ in all directions. 216 macro-particles per species per cell are used, resulting in 2.5 billion macro-particles in total. To reduce the computational cost, an artificially reduced ion-electron mass ratio of $m_i/m_e = 100$ is used. The cell size is $\sim 1/8$ of the ion

inertial length or ~ 1.2 of the plasma skin depth.

4.2 Simulation Results

Each simulation of $300\,s$ physical time takes about 230,000 core hours on Pleiades. About 60% of the core hours were used for iPIC3D and BATS-R-US used the remaining 40%. BATS-R-US almost used as many core hours as iPIC3D because the time step of BATS-R-US is limited to a small value ($\sim 3 \times 10^{-4}\,s$) by the high Alfven velocity near the poles. In contrast, iPIC3D takes $\sim 10^{-3}\,s$ as time step. The results from these three simulations are presented in this section.

4.2.1 Magnetotail Reconnection

Magnetotail reconnection is crucial for global magnetospheric convection. It transfers the magnetic flux back to the dayside magnetosphere. This subsection will discuss the tail reconnection seen in the simulations. To reduce the complexity, we will start the discussion with the simulation results of case-2, which has purely southward IMF. The Hall magnetic field B_y and the field lines at the meridional plane at $t = 89.8\,s$ are shown in Figure 4.2. There are two X-lines in the snapshot: the primary X-line is at $x = -1.8\,R_M$ and the secondary X-line is near $x = -2.1\,R_M$. A small flux rope with negative core field B_y is formed between these two X-lines. The reconnection sites are surrounded by a quadrupolar Hall magnetic field. Since there is no B_y component in the IMF, the background B_y field is also close to zero in the tail meridional plane, and the quadrupolar field is approximately north-south symmetric with a field strength of $\sim 20\,\mathrm{nT}$.

The electron velocity in the x direction u_{ex} and the electron number density n_e are shown in Figure 4.3. The electrons are flowing towards the reconnection sites along the separatrices. The velocity of the electron inflow from the tail side is $\sim 3000\,\mathrm{km/s}$, and the planet side inflow can be accelerated to $\sim 10000\,\mathrm{km/s}$. The fast inflow leads to

two narrow electron density depletion layers along the interface of close and open field lines (see the right panel of Figure 4.3). The electron density of the depletion layers is about one order smaller than that of the surrounding region. The width of these layers are $\sim 0.02\,R_M$ or $\sim 50km$, which is the same order as the ambient electron skin depth. Similar depletion layers have been observed in Earth's magnetotail (*Oieroset*, 2001). More information about the plasma velocities are shown in Figure 4.4. The ion jets shown in Figure 4.4(c) further confirm the existence of two X-lines. The ion and electron velocities in the y direction create the cross-tail current. The electrons are moving along the negative y direction while the ions are flowing along the positive y direction. The ion velocity can reach $\sim 1000\,\mathrm{km/s}$ near the reconnection sites. Similar high ion velocity is also found from Hall MHD simulation of Ganymede's magnetosphere (*Dorelli et al.*, 2015). The width of the electron (ion) velocity layer is about $0.02\,R_M$ ($0.2\,R_M$), which is close to the electron (ion) inertial length.

4.2.2 The Properties of the Flux Ropes

Flux ropes are the products of magnetic reconnection. They can move either tailward or planetward. The tailward moving flux ropes are also termed as plasmoids. The generation and evolution of a planetward moving flux rope is shown in Figure 4.5. At $t = 90\,s$, there is only one X-line near $x = -1.9\,R_M$. $0.6\,s$ later, another X-line appears near $x = -1.6\,R_M$ and a small flux rope-like structure forms between these two X-lines. The center of this flux rope is overlapped with one branch of the quadrupolar Hall magnetic field, and the Hall field is the seed of the core field. At this moment, the amplitude of the core field B_y has increased to $\sim 30\,\mathrm{nT}$. At $t = 91.4\,s$, the core field with positive B_y of $\sim 60\,\mathrm{nT}$ is surrounded by another branch of the Hall field, the sign of which reverses. The magnetic field components along the line $z = 0.17\,R_M$ are shown in Figure 4.6. The B_z field jumps from the positive peak at $x = -1.75\,R_M$ to the negative peak at $x = -1.6\,R_M$. The peak-to-peak distance

of $0.15\,R_M$ or 360 km agrees with the MESSENGER observations (*DiBraccio et al.*, 2015). The amplitudes of the B_z peak-to-peak jump and the core field B_y are about twice of the averaged MESSENGER observations. The ion number density at the flux rope center is $2.5\,\mathrm{cm}^{-3}$, and the MESSENGER observations indicate an average value of $3.15\,\mathrm{cm}^{-3}$. The 3D view of the flux rope is shown in Figure 4.7. The field lines are connected to Mercury on one side. Interestingly, the other end of the flux rope is still connected to the tailward field lines. Since the field lines at the planetward edge of the flux rope are southward, but the closed field lines are northward, the flux rope will finally reconnect with the closed field lines. The remnant of the flux rope can be seen near $x = -1.4\,R_M$ and $z = 0.15\,R_M$ at $t = 92.2\,s$ in Figure 4.5.

A typical tailward flux rope is shown in Figure 4.8. It is generated near $x = -2.2\,R_M$ and then propagates tailward. Finally it merges with the open filed lines near $x = -3.8\,R_M$. The magnetic field structure at $t = 34.8\,s$ is presented in Figure 4.9, which shows the fields along the line of the $z = 0.16\,R_M$. The B_z peak-to-peak distance is about $0.2\,R_M$, the B_z jump amplitude is $\sim 35\,\mathrm{nT}$, and the core field strength is $\sim 25\,\mathrm{nT}$. The ion number density near the core is about $2\,\mathrm{cm}^{-3}$. All these values agree with MESSENGER observations (*DiBraccio et al.*, 2015). The length of the flux rope in the dawn-dusk direction is about $0.5\,R_M$, which can be seen from Figure 4.10.

The event shown in Figure 4.8 is a typical tailward flux ropes for case-2 simulation in terms of the size and field structure. Figure 4.11 shows an example of typical flux ropes from case-3 simulation, which has a large positive IMF B_y component. This flux rope has larger size (B_y peak-to-peak length is $\sim 0.6\,R_M$) and stronger core field compared with the case-2 flux ropes. By checking a series of snapshots, it is found all the flux ropes in case-3 have positive core field B_y, which is consistent with the IMF B_y. Case-2 simulation generates both negative and positive core field flux ropes, for example, the core field of the small flux rope in Figure 4.2 is negative and it is positive

in the event shown in Figure 4.8, but, surprisingly, positive B_y flux ropes dominate for the tailward flux ropes for case-2 simulation. More detailed further investigation is needed for this topic.

4.2.3 Dawn-Dusk Asymmetry

For the ideal MHD system, the simulation with purely southward IMF is symmetric in the dawn-dusk direction; therefore the observed dawn-dusk asymmetry (*Sun et al.*, 2016) must be caused by the non-ideal MHD effects. This section will present the dawn-dusk asymmetry seen from the simulations.

Since the current aligned instabilities can develop inside the current sheet, the current sheet is twisting and flapping during the simulation. In order to visualize the difference in the dawn-dusk direction during magnetic reconnection, we can project the values on the surface of $B_x = 0$ on an x-y plane. The projected plane is calculated every $0.1\,s$, and the average of all the projections during the $300\,s$ long simulations is shown in Figure 4.12. The 1D cuts at $x = -1.5\,R_M$ and $x = -2.6\,R_M$ are also shown in Figure 4.13 and Figure 4.14, respectively. Even for the case-2 simulation, where the IMF is purely southward, the dawn-dusk asymmetry still arises. The asymmetries of the electron pressure p_e and ion pressure p_i are the consequences of the Hall effect. Inside the current sheet, the ions are moving from the dawn (the negative y direction) side to the dusk (the positive y direction) (see Figure 4.4). Along the dawn-dusk direction, the ion velocity u_{iy} reaches local maximum near the x-axis, therefore the ion pressure is enhanced on the dusk direction due to the ion velocity divergence (compression). The electrons are moving from the dusk to the dawn, and the electron pressure is increased on the dawn side. The pressure asymmetry can be clearly seen in all three simulations.

The products of the magnetic reconnection, the ion and electron jets are also shown in Figure 4.12. The case-1 and case-2 simulations show obvious dawn-dusk

asymmetry for the planetward flows. Figure 4.13 shows the 1D cuts at $x = -1.5\,R_M$. It is clear that the planetward jets have the largest velocity near $y = -0.25\,R_M$ for case-1 and case-2. This suggests that the fast reconnection jets should be more frequently observed on the dawn side. For the case-3 simulation, the asymmetry is less obvious. The x component of the ion and electron velocities along the $x = -2.6\,R_M$ cut are shown in Figure 4.14. Similar to the planetward jets, the centers of the tailward jets are near $y = -0.25\,R_M$ for the case-1 and case-2 simulations.

From Figure 4.12, we can see another significant difference between these three simulations: the reconnection jets in case-2 are faster than that of the other two simulations. That is because the southward IMF B_z of case-2 is stronger, and more field lines are transported from the dayside to the tail; in order to maintain the flux conservation, the tail reconnection should be stronger or more frequent for case-2, and creates faster averaged plasma flows.

4.3 Discussion and Summary

This chapter discusses the MHD-EPIC simulations of Mercury's magnetosphere. The PIC box is placed around the near tail X-line to study the tail reconnection. Typical symmetric magnetic reconnection signatures, such as the quadrupolar Hall magnetic field, the ion and electron flow patterns, are identified from the simulations. We found the electron density near the interfaces of the open-closed field lines is about one order smaller than the surrounding region. Flux ropes, both the planetward and the tailward, are generated. The flux rope cross-sectional scale, magnetic field signature, and the ion density around the flux rope center agree well with the MESSENGER observations (*DiBraccio et al.*, 2015). The length of the flux ropes in the dawn-dusk direction is about $0.5\,R_M$. The dawn-dusk asymmetry is also identified from the simulations. The averaged electron and ion jets are stronger on the dawn side, which is also consistent with the MESSENGER observations (*Sun et al.*, 2016).

In these simulations, the PIC box extends from $y = -1.5\,R_M$ to $y = 1.5\,R_M$ in the y direction. It is still far away form the magnetopause, thus the kinetic effect of the Kelvin-Helmholtz instability (KHI) is not included in the current simulations. The heavy ions, such as Na^+, are also not included. But the dawn-dusk asymmetry still arises in the simulations. The electron pressure and ion pressure are asymmetric in the dawn-dusk direction, but the total pressure is almost symmetric, which suggests the current sheet thickness is also symmetric. The pressure asymmetry for each species leads to different temperature and gyroradius on each side. How the difference in the gyroradius is related to the reconnection asymmetry still needs to be explored in the future (*Lu et al.*, 2016). In our three simulations, the one with large IMF B_y does not show clear reconnection asymmetry. It suggests another possibility: the reconnection dawn-dusk asymmetry may be caused by the mechanism that is responsible for the spreading of X-lines. *Shepherd and Cassak* (2012) suggested that the X-lines spread with the electron velocity for the weak guide field system, while the X-lines extend in both directions with Alfven velocity in the system with strong guide field. If the onset location of the reconnection were symmetric in the Mercury's magnetotail, we would expect the X-lines occur more frequently on the dawnside for case-1 and case-2, but not case-3 based on the theory of *Shepherd and Cassak* (2012). This expectation is consistent with the simulation results. More analysis are needed to confirm this hypothesis.

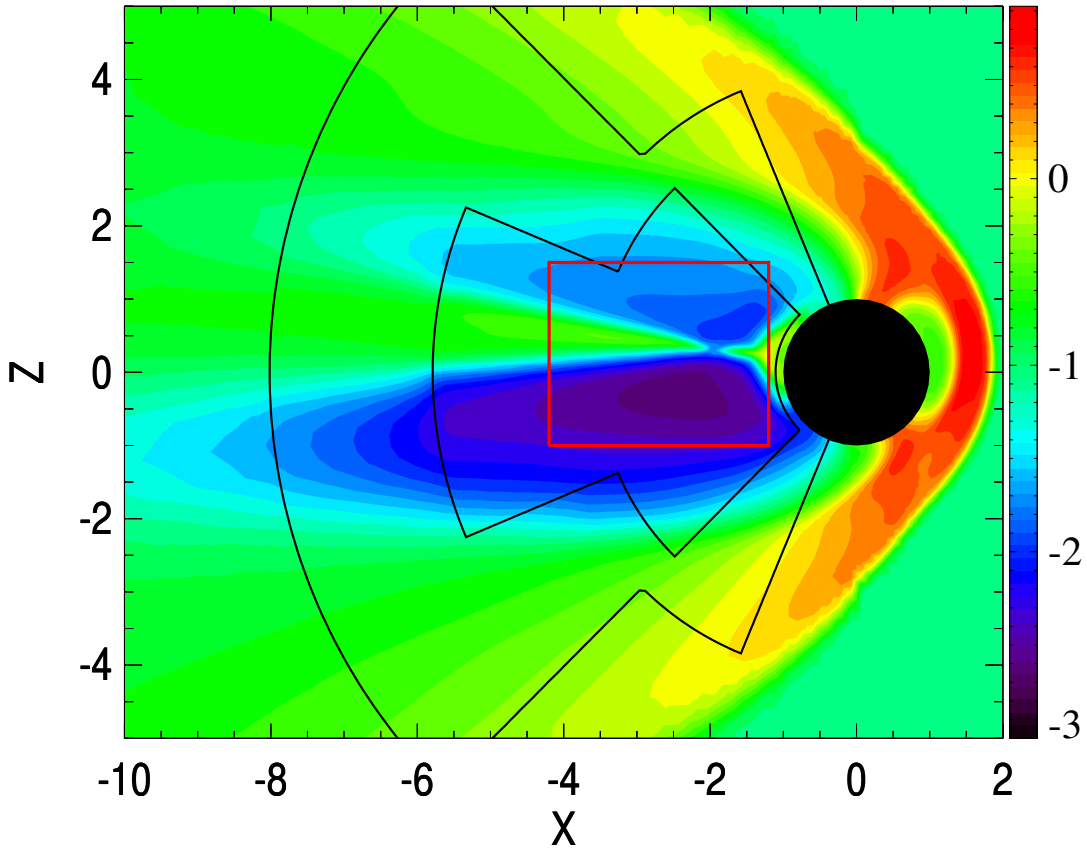

Figure 4.1: Part of the meridional plane with the adaptive MHD grid and the PIC region. The color represents the plasma pressure in nPa on a logarithmic scale. The black lines represent the grid refinement levels. The red box ($-4.2\,R_M < x < -1.2\,R_M$, $-1\,R_M < z < 1.5\,R_M$) is the edge of the PIC region covered by iPIC3D, and it extends from $-1.5\,R_M$ to $1.5\,R_M$ in the y direction.

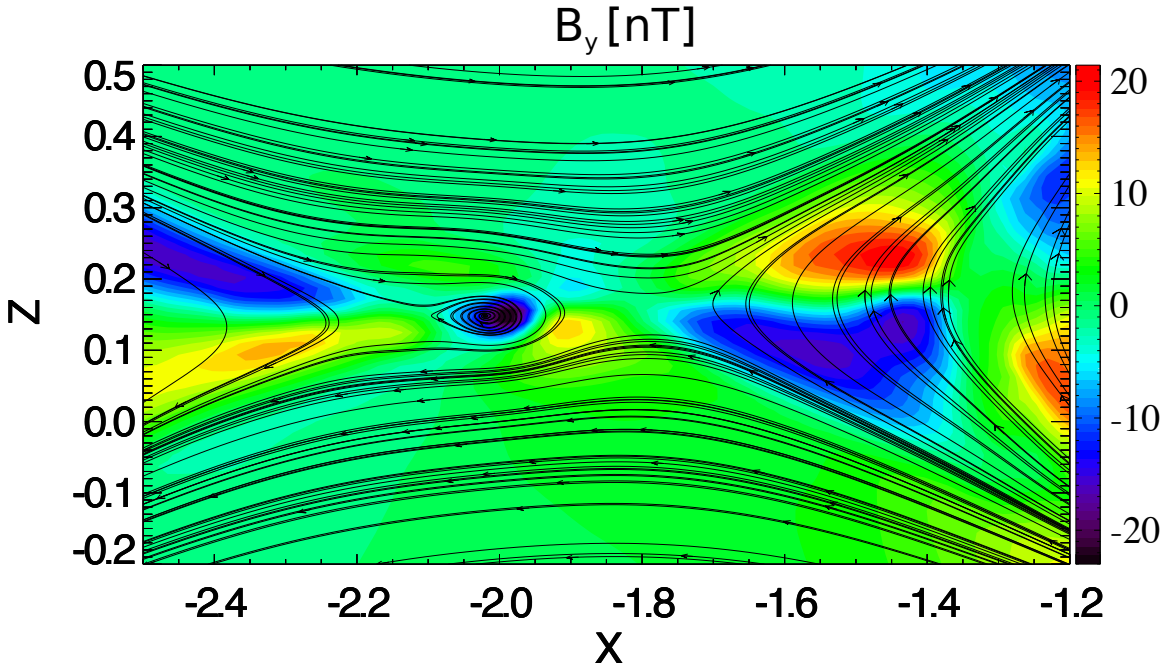

Figure 4.2: The B_y [nT] field overplotted with magnetic field lines on the meridional plane at $t = 89.8\,s$.

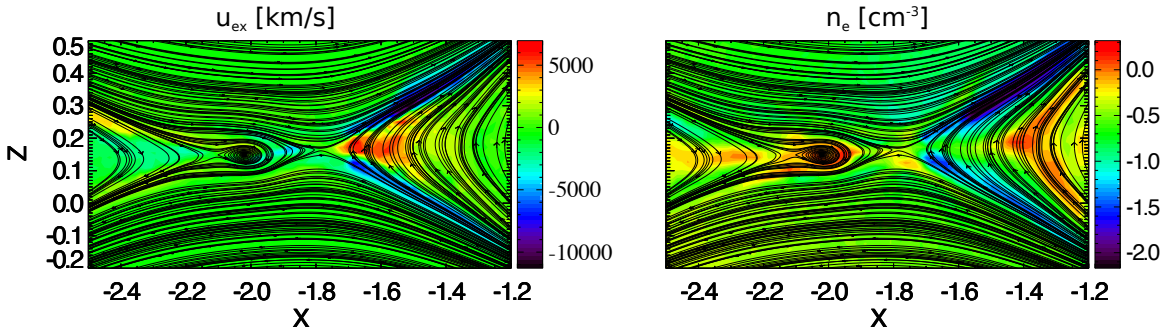

Figure 4.3: The left panel is the electron velocity in the x direction u_{ex} [km/s]. The right panel is the electron number density n_e [cm^{-3}] on a logarithmic scale. Both plots are overplotted with magnetic field lines.

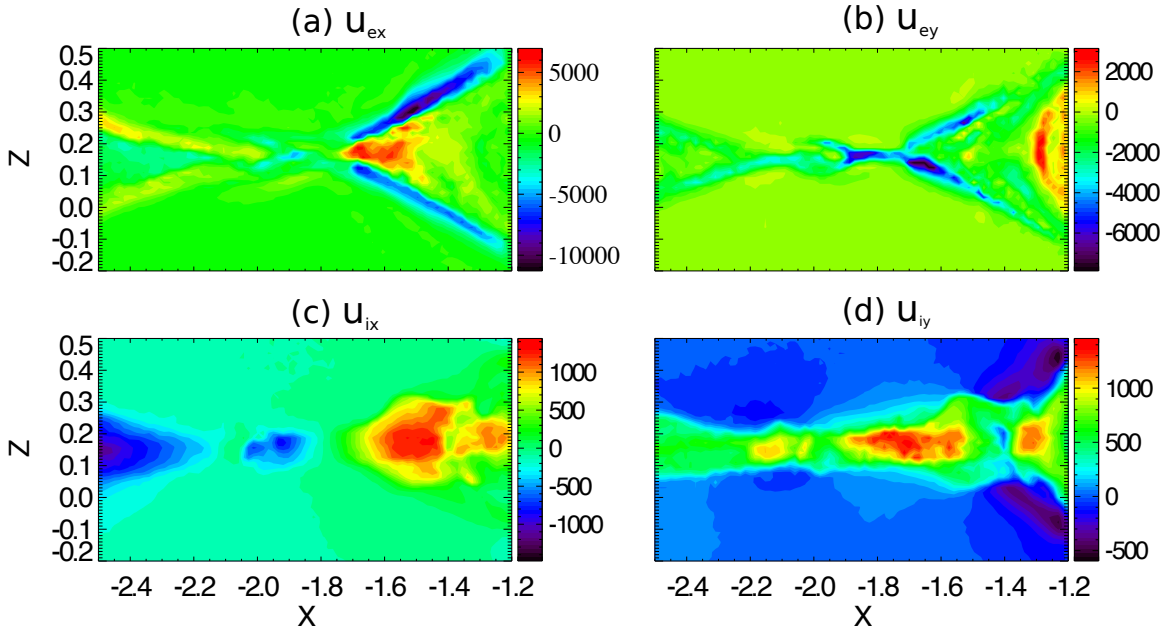

Figure 4.4: (a) Electron velocity in the x direction. The same as left panel of Figure 4.3. (b) Electron velocity in the y direction. (c) Ion velocity in the x direction. (d) Ion velocity in the y direction. Units: km/s

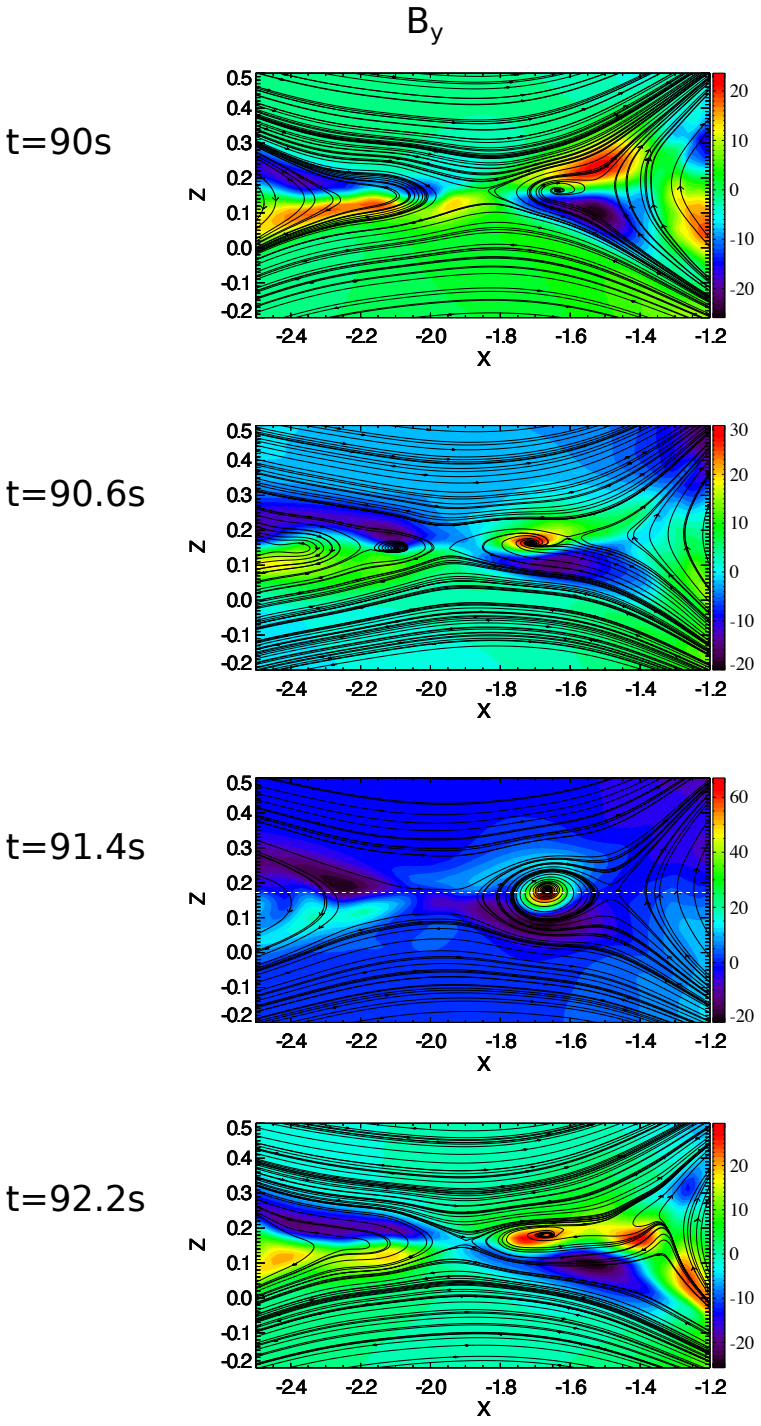

Figure 4.5: A series of the B_y [nT] field overplotted with magnetic field lines on the meridional plane.

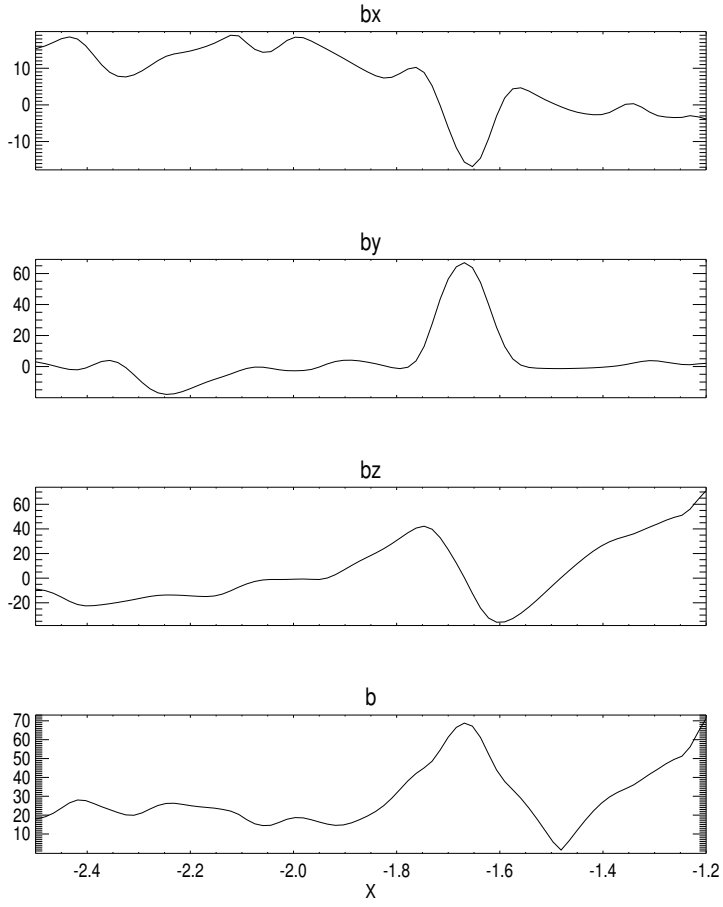

Figure 4.6: The magnetic field signature along the line of $y = 0$ and $z = 0.17\,R_M$, which is marked as white dashed line in panel 3 of Figure 4.5.

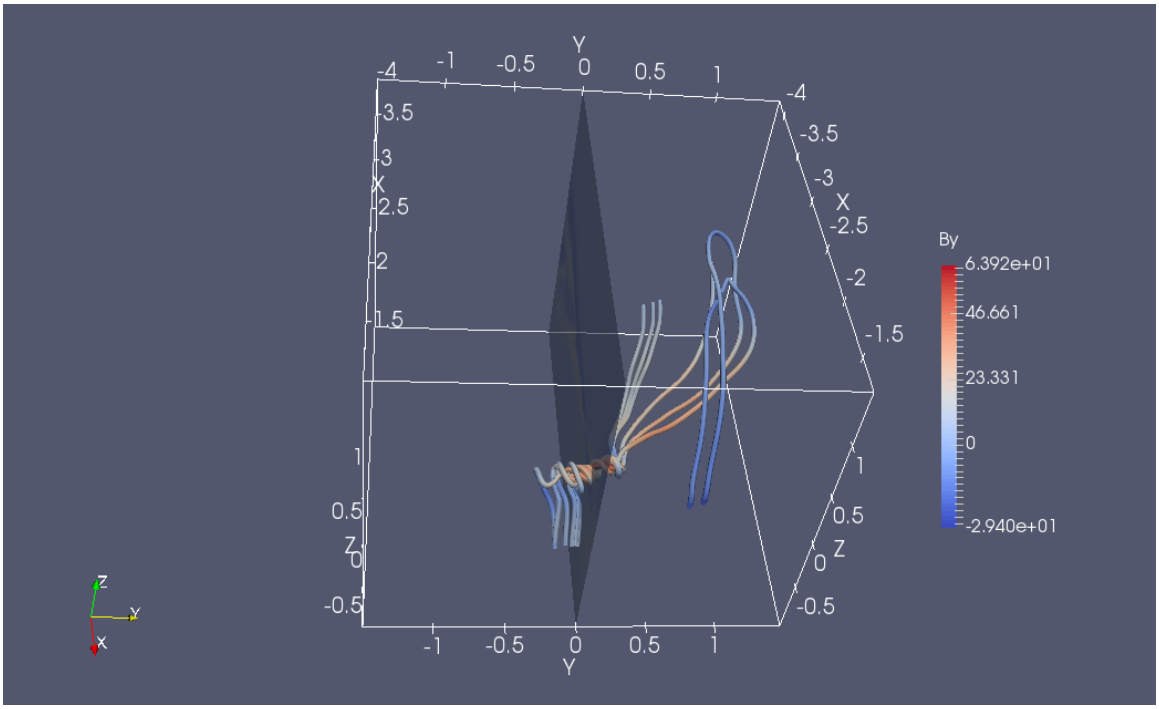

Figure 4.7: The 3D view of the planetward flux rope at $t = 94.4\,s$. The field lines are colored by the B_y field.

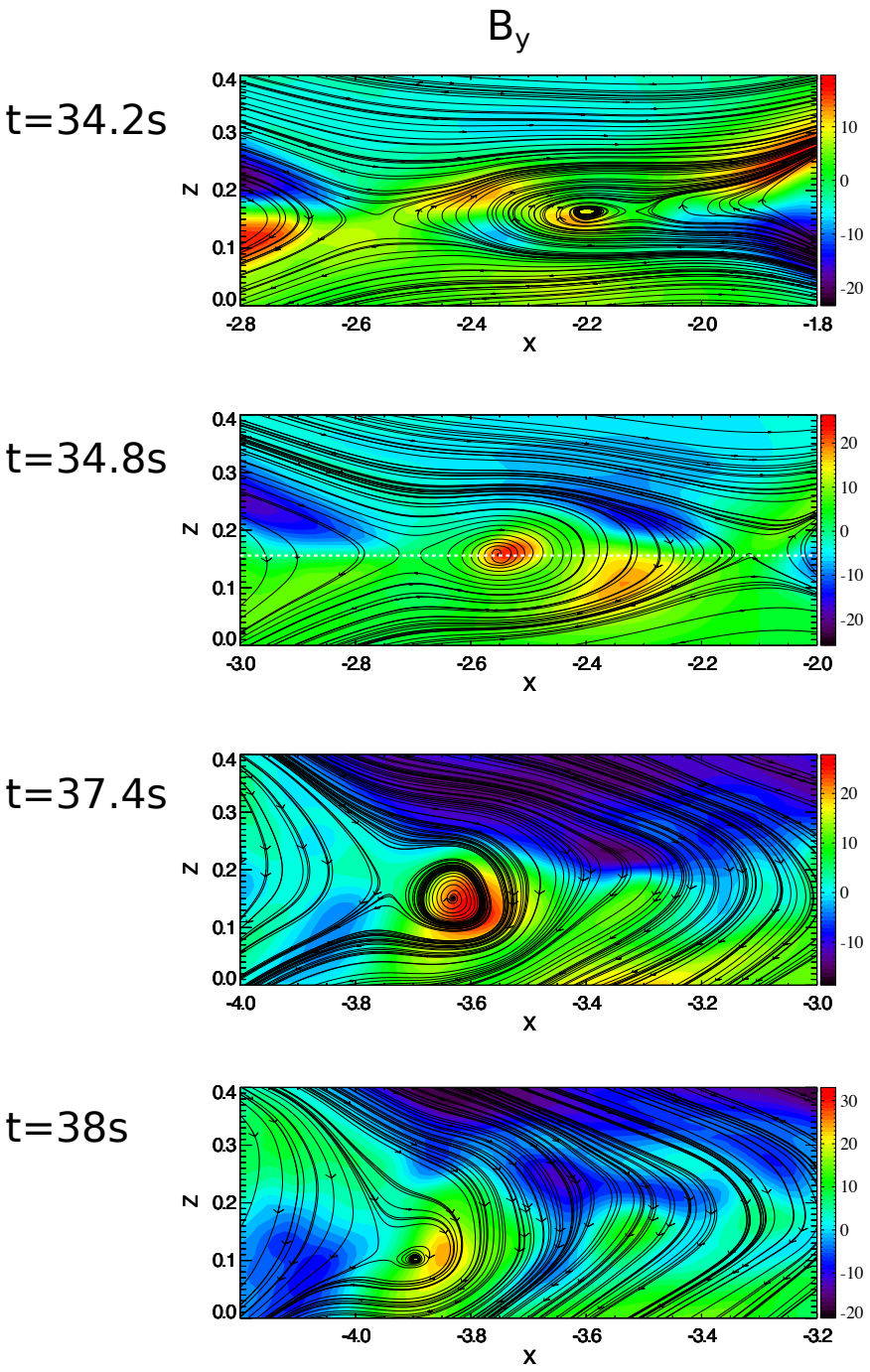

Figure 4.8: A series of the B_y [nT] field overplotted with field lines on the meridional plane. These plots show the evolution of a tailward flux rope. The white dotted line in the second panel shows the cut along which the field components are shown in Figure 4.9.

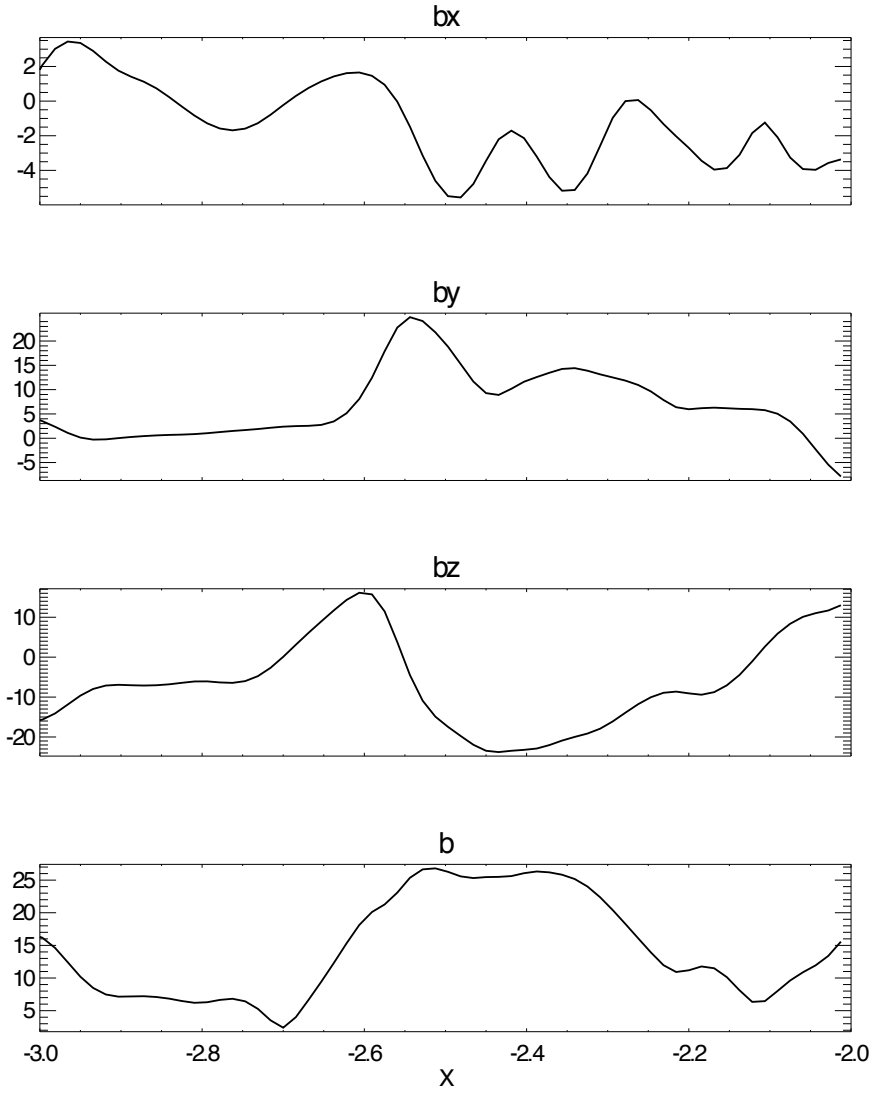

Figure 4.9: The magnetic field signature along the line of $y = 0$ and $z = 0.16\,R_M$, which is marked as white dashed line in the second panel of Figure 4.8.

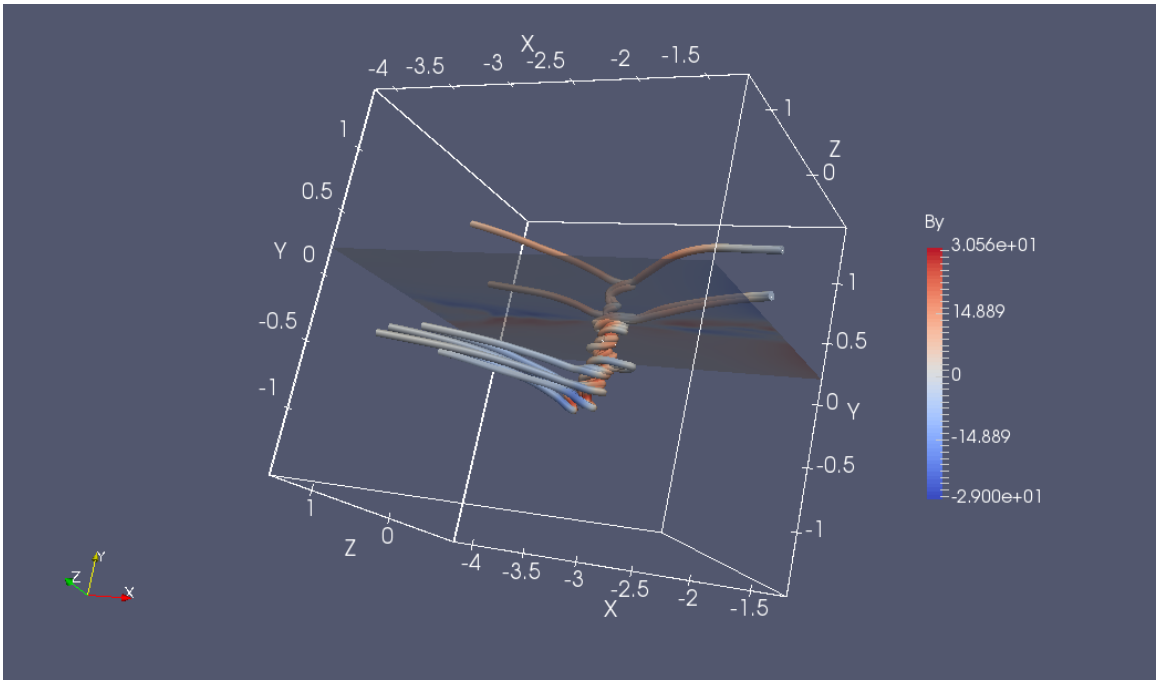

Figure 4.10: The 3D view of the tailward flux rope at $t = 34.8\,s$. The field lines are colored by the B_y field.

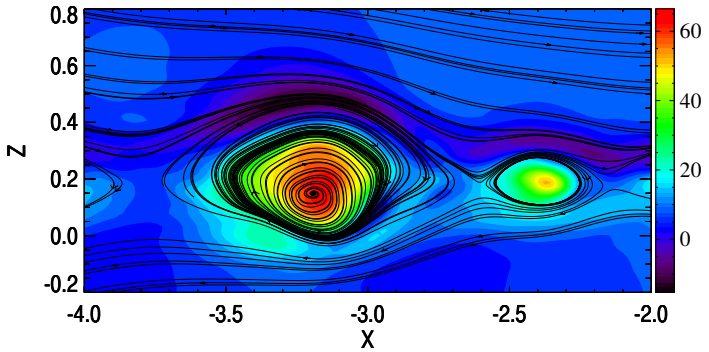

Figure 4.11: An example of typical flux ropes from the case-3 simulation, which has a large IMF B_y component. The B_y component and the field lines are shown.

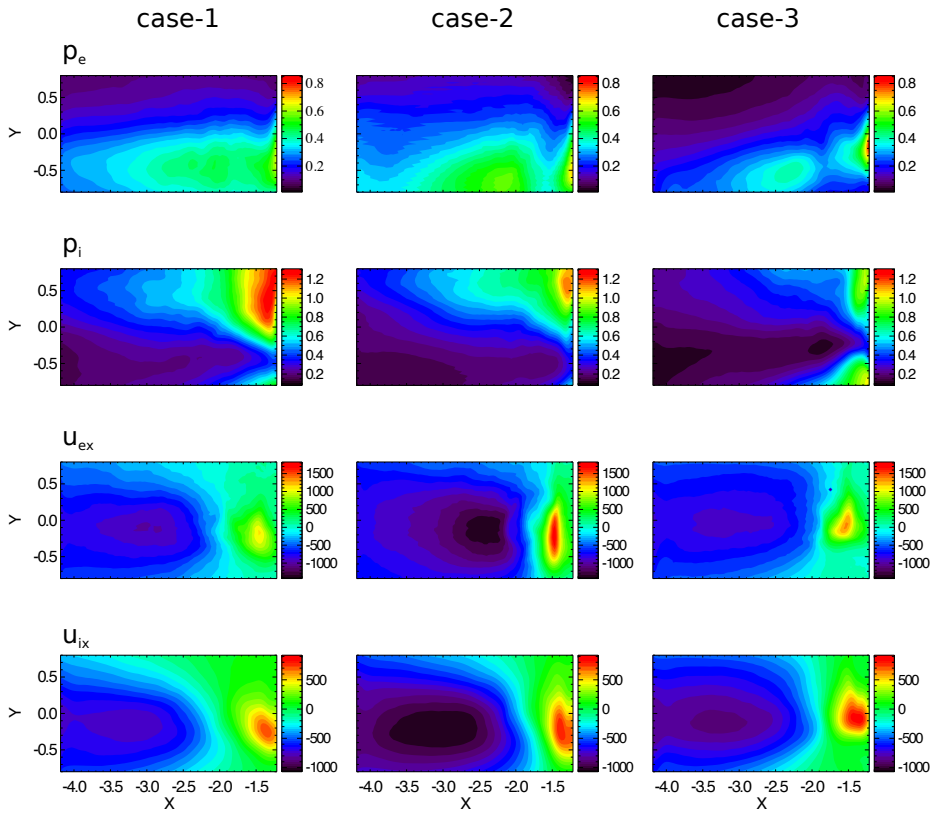

Figure 4.12: The average of various quantities at the $B_x = 0\,\mathrm{nT}$ surface over the $300\,s$ simulations. From top to bottom, the electron pressure p_e [nPa], the ion pressure p_i [nPa], the electron velocity in the x direction u_{ex} [km/s], and the ion velocity u_{ix} [km/s] are shown.

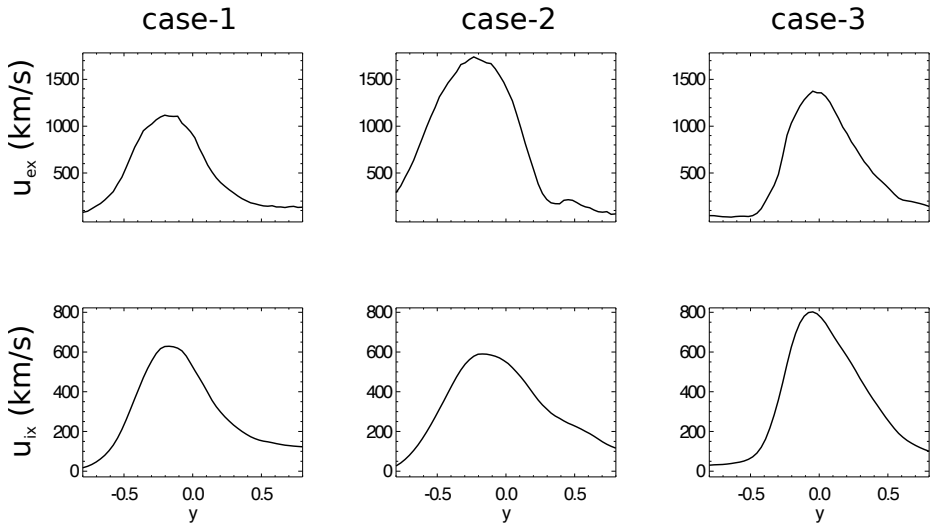

Figure 4.13: The 1D cuts at $x = -1.5\,R_M$ of the same data shown in Figure 4.12.

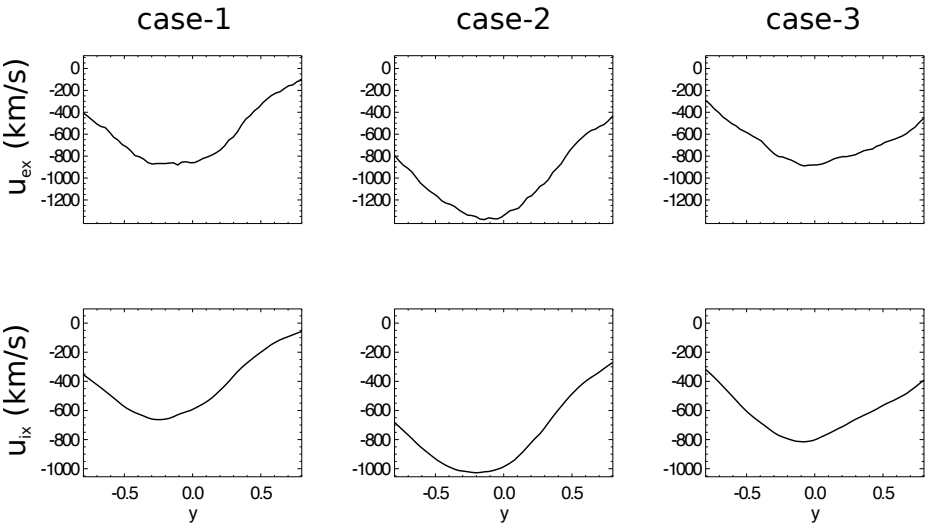

Figure 4.14: The 1D cuts at $x = -2.6\,R_M$ of the same data shown in Figure 4.12.

CHAPTER V

Summary and Future work

Numerical models are important tools for space physics research. In order to improve the numerical accuracy and physics capability of the MHD model BATS-R-US, a fifth-order accurate finite difference scheme on block-adaptive curvelinear grids and the magnetohydrodynamics with embedded particle-in-cell (MHD-EPIC) model are developed, respectively. The applications of the MHD-EPIC model to Earth's dayside magnetopause reconnection and Mercury's magnetotail reconnection are also presented in this dissertation.

5.1 Summary

Chapter II describes the high-order accurate scheme that has been implemented for BATS-R-US. This scheme employs the 5th order accurate monotonicity preserving limiter MP5 to construct high-order accurate face fluxes. The fifth-order accuracy of the spatial derivatives is ensured by a flux correction step. The method is generalized to curvilinear grids with a free-stream preserving discretization. It is also extended to block-adaptive grids using carefully designed ghost cell interpolation algorithms. Only three layers of ghost cells are required, and the grid blocks can be as small as $6 \times 6 \times 6$ cells. Dynamic grid refinement and coarsening are also fifth-order accurate. All interpolation algorithms employ a general limiter based on the principles of the

MP5 limiter. The finite difference scheme is fully conservative on static uniform grids. Conservation is only maintained at the truncation error level at grid resolution changes and during grid adaptation, but the numerical tests indicate that the results are still very accurate.

The MHD-EPIC model was originally developed by *Daldorff et al.* (2014). In the past two years, we have greatly improved its robustness and efficiency, extended its capabilities, and applied it to more simulations. The MHD-EPIC simulation of Earth's dayside magnetopause reconnection is discussed in chapter III. Both the global scale FTEs and the kinetic scale phenomena, such as the LHDI, are captured in one model. It is found the magnetic field signature of FTEs at their early formation stage is similar to a 'crater FTE'. After the FTE core field grows to a significant value, it becomes an FTE with typical flux rope structure. When an FTE moves across the cusp, reconnection between the FTE field lines and the cusp field lines can dissipate the FTE. The crescent electron phase space distribution, which has been observed by MMS, is found near the reconnection site. A similar distribution is found for ions at the location where the Larmor electric field appears. The lower hybrid drift instability (LHDI) along the current sheet direction also arises at the interface of magnetosheath and magnetosphere plasma. The LHDI electric field is about 8 mV/m and its dominant wavelength relative to the electron gyroradius agrees reasonably with MMS observations.

Mercury's magnetotail reconnection is also studied with the MHD-EPIC model in chapter IV. Both the planetward and tailward flux ropes are generated from the simulations. The flux rope size, magnetic field structure, and the plasma density are consistent with the observations. A typical flux rope is about $0.5\,R_M$ long in the dawn-dusk direction. The dawn-dusk asymmetries are identified from the simulations. The pressure asymmetry is caused by the velocity divergence. The asymmetry of the reconnection jets from the simulations is consistent with the observations, but the

cause of the asymmetry needs to be further explored.

5.2 Future Work

The high-order scheme has shown its significant improvement compared with the second-order schemes for the test problems. The high-order scheme provides an opportunity to do high resolution global simulations. A lot of works can be done with the scheme, such as the simulation of KelvinHelmholtz instability (KHI) along the magnetopause.

The MHD-EPIC model can be further improved in various ways:

- The Earth's dayside magnetopause simulations show the PIC code heats the electrons so that the electron-ion pressure is about $p_i/p_e \sim 2.5$. We are planning to investigate the heating mechanism. One potential reason is the cell size in the simulations is too large for electrons, and the electrons are heated by the finite grid instability.

- The next major improvement is to break the constraints on the shape the PIC regions. As shown in the Earth's simulation, a brick has to be used to cover the dayside magnetopause even though the magnetopause is a curved surface. The iPIC3D developers are developing the AMR mesh for iPIC3D. It will allow us to cover the magnetopause with a larger box, and we can refine the region along the magnetopause. Another approach is to develop curvilinear meshes for iPIC3D. A combination of these two techniques will be even more useful.

In terms of the Earth and Mercury simulations, a lot of interesting questions still need to be clarified:

- The spreading of the X-lines. From the evolution of the FTEs (see Figure 3.4), we can see the X-line starts from a point. The Mercury simulations suggest

the mechanism of X-line spreading may cause the dawn-dusk asymmetry in Mercury's tail. The current simulations show some evidence (not discussed in the dissertation) that the X-lines spread faster in the electron velocity direction, but further investigation is necessary.

- The properties of the flux ropes, including the FTEs. Some details are still unknown, such as how the core field is enhanced and how the plasma escapes from the flux rope center.

- Covering both the dayside and tail reconnection sites with PIC boxes in one simulation. This kind of simulations will contain realistic reconnection processes on both sides, and hopefully it will help us to understand some import topics, such as the trigger of a substorm, the consequences of a substorm and the global reconnection rate.

- Mercury's magnetospheric dynamics. Although the dawn-dusk asymmetry can arise from the current simulations, the heavy ions and the KHI at the magnetopause may play important roles in modulating the dawn-dusk asymmetry. The MHD-EPIC model already has the capability to include heavy ions in the MHD model and also in iPIC3D.

BIBLIOGRAPHY

BIBLIOGRAPHY

Anderson, B. J., et al. (2011), The global magnetic field of mercury from messenger orbital observations, *Science*, *333*(6051), 1859–1862.

Balsara, D. S., and C.-W. Shu (2000), Monotonicity preserving weighted essentially non-oscillatory schemes with increasingly high order of accuracy, *J. Comput. Phys.*, *160*(2), 405–452.

Balsara, D. S., T. Rumpf, M. Dumbser, and C.-D. Munz (2009), Efficient, high accuracy ader-weno schemes for hydrodynamics and divergence-free magnetohydrodynamics, *J. Comput. Phys.*, *228*(7), 2480–2516.

Berger, M. J., and P. Colella (1989), Local adaptive mesh refinement for shock hydrodynamics, *J. Comput. Phys.*, *82*, 67–84.

Biermann, L. (1951), Kometenschweife und solare korpuskularstrahlung, *Zeitschrift fur Astrophysik*, *29*, 274.

Birdsall, C. K., and A. B. Langdon (2004), *Plasma physics via computer simulation*, CRC Press.

Birn, J., et al. (2001), Geospace Environmental Modeling (GEM) magnetic reconnection challenge, *J. Geophys. Res.*, *106*(A3), 3715–3720, doi:10.1029/1999JA900449.

Bode, B., M. Butler, T. Dunning, W. Gropp, T. Hoe-fler, W.-m. Hwu, and W. Kramer (2012), The blue waters super-system for super-science. contemporary hpc architectures, jeffery vetter editor.

Brackbill, J., and D. Forslund (1982), An implicit method for electromagnetic plasma simulation in two dimensions, *J. Comput. Phys.*, *46*, 271–308, doi:10.1016/0021-9991(82)90016-X.

Burch, J. L., et al. (2016), Electron-scale measurements of magnetic reconnection in space, *Science*, *352*, 6290, doi:10.1126/science.aaf2939.

Capdeville, G. (2008), A centeral weno scheme for solving hyperbolic conservation laws on non-uniform meshes, *J. Comput. Phys.*, *227*(5), 2977 – 3014, doi: http://dx.doi.org/10.1016/j.jcp.2007.11.029.

Chen, Y., G. Tóth, and T. I. Gombosi (2016), A fifth-order finite difference scheme for hyperbolic equations on block-adaptive curvilinear grids, *J. Comput. Phys.*, *305*, 604, doi:10.1016/j.jcp.2015.11.003.

Cockburn, B., and C.-W. Shu (1998), The runge–kutta discontinuous galerkin method for conservation laws v: multidimensional systems, *Journal of Computational Physics*, *141*(2), 199–224.

Cockburn, B., and C.-W. Shu (2001), Runge–kutta discontinuous galerkin methods for convection-dominated problems, *Journal of scientific computing*, *16*(3), 173–261.

Daldorff, L. K. S., G. Tóth, T. I. Gombosi, G. Lapenta, J. Amaya, S. Markidis, and J. U. Brackbill (2014), Two-way coupling of a global Hall magnetohydrodynamics model with a local implicit Particle-in-Cell model, *J. Comput. Phys.*, *268*, 236, doi:10.1016/j.jcp.2014.03.009.

Daly, P., D. Williams, C. Russell, and E. Keppler (1981), Particle signature of magnetic flux transfer events at the magnetopause, *Journal of Geophysical Research: Space Physics*, *86*(A3), 1628–1632.

Daughton, W. (2003), Electromagnetic properties of the lower-hybrid drift instability in a thin current sheet, *Physics of Plasmas*, *10*(8), 3103–3119.

Dawson, J. M. (1983), Particle simulation of plasmas, *Reviews of modern physics*, *55*(2), 403.

Del Zanna, L., N. Bucciantini, and P. Londrillo (2003), An efficient shock-capturing central-type scheme for multidimensional relativistic flows-ii. magnetohydrodynamics, *Astronomy & Astrophysics*, *400*(2), 397–413.

Del Zanna, L., O. Zanotti, N. Bucciantini, and P. Londrillo (2007), Echo: a eulerian conservative high-order scheme for general relativistic magnetohydrodynamics and magnetodynamics, *Astronomy & Astrophysics*, *473*(1), 11–30.

Deng, X., and H. Zhang (2000), Developing high-order weighted compact nonlinear schemes, *Journal of Computational Physics*, *165*(1), 22–44.

Deng, X., M. Mao, G. Tu, H. Liu, and H. Zhang (2011), Geometric conservation law and applications to high-order finite difference schemes with stationary grids, *Journal of Computational Physics*, *230*(4), 1100–1115.

DiBraccio, G. A., et al. (2015), Messenger observations of flux ropes in mercury's magnetotail, *Planetary and Space Science*, *115*, 77–89.

Dorelli, J., and A. Bhattacharjee (2009), On the generation and topology of flux transfer events, *Journal of Geophysical Research: Space Physics*, *114*(A6).

Dorelli, J. C., A. Glocer, G. Collinson, and G. Toth (2015), The role of the hall effect in the global structure and dynamics of planetary magnetospheres: Ganymede as a case study, *JGR*, *120*, 5377–5392, doi:10.1002/2014JA020951.

Drake, J., M. Shay, and M. Swisdak (2008), The hall fields and fast magnetic reconnection, *Physics of plasmas*, *15*(4), 042,306.

Dumbser, M., O. Zanotti, A. Hidalgo, and D. S. Balsara (2013), Ader-weno finite volume schemes with space–time adaptive mesh refinement, *Journal of Computational Physics*, *248*, 257–286.

Dungey, J. (1961), Interplanetary magnetic field and the auroral zones, *Phys. Rev. Lett.*, *93*, 47, doi:10.1103/PhysRevLett.6.47.

Eastwood, J., T. Phan, R. Fear, D. Sibeck, V. Angelopoulos, M. Øieroset, and M. Shay (2012), Survival of flux transfer event (fte) flux ropes far along the tail magnetopause, *Journal of Geophysical Research: Space Physics*, *117*(A8).

Eastwood, J., et al. (2016), Ion-scale secondary flux ropes generated by magnetopause reconnection as resolved by mms, *Geophysical Research Letters*, *43*(10), 4716–4724.

Eastwood, J. P., H. Hietala, G. Toth, T. D. Phan, and M. Fujimoto (2015), What controls the structure and dynamics of earth's magnetosphere?, *Space Science Reviews*, *188*(1), 251–286, doi:10.1007/s11214-014-0050-x.

Einfeldt, B. (1988), On Godunov-type methods for gas dynamics, *SIAM J. Numer. Anal.*, *25*(2), 294–318.

Eriksson, S., P. Cassak, A. Retinò, and F. Mozer (2016), Subsolar magnetopause observation and kinetic simulation of a tripolar guide magnetic field perturbation consistent with a magnetic island, *Geophysical Research Letters*, *43*(7), 3035–3041.

Eriksson, S., et al. (2015), On multiple reconnection x-lines and tripolar perturbations of strong guide magnetic fields, *The Astrophysical Journal*, *805*(1), 43.

Fear, R., S. Milan, A. Fazakerley, E. Lucek, S. Cowley, and I. Dandouras (2008), The azimuthal extent of three flux transfer events.

Fedder, J. A., S. P. Slinker, J. G. Lyon, and C. T. Russell (2002), Flux transfer events in global numerical simulations of the magnetosphere, *J. Geophys. Res.*, *107*(A5), doi:10.1029/2001JA000025.

Godunov, S. K., A. W. Zabrodyn, and G. P. Prokopov (1961), A difference scheme for two-dimensional unsteady problems of gas dynamics and computation of flow with a detached shock wave, *Zhurnal Vychyslitelnoi Matematiki i Matematicheskoi Fiziki*, *1*(6), 1020.

Graham, D., et al. (2016), Lower hybrid waves in the ion diffusion and magnetospheric inflow regions, *Journal of Geophysical Research: Space Physics*.

Harten, A. (1983), High resolution schemes for hyperbolic conservation laws, *J. Comput. Phys.*, *49*, 357–393.

Harten, A., P. D. Lax, and B. van Leer (1983), On upstream differencing and Godunov-type schemes for hyperbolic conservation laws, *SIAM Rev.*, *25*(1), 35–61.

Harten, A., B. Enquist, S. Osher, and S. R. Chakravarthy (1987), Uniformly high order accurate essentially non-oscillatory schemes, iii, *J. Comput. Phys.*, *71*, 231–303.

Hasegawa, H., B. Ö. Sonnerup, C. Owen, B. Klecker, G. Paschmann, A. Balogh, and H. Rème (2006), The structure of flux transfer events recovered from cluster data, in *Annales Geophysicae*, vol. 24, pp. 603–618.

Hesse, M., K. Schindler, J. Birn, and M. Kuznetsova (1999), The diffusion region in collisionless magnetic reconnection, *Phys. Plasmas*, *6*, 1781, doi:10.1063/1.873436.

Hoilijoki, S., U. Ganse, Y. Pfau-Kempf, P. A. Cassak, B. M. Walsh, H. Hietala, S. von Alfthan, and M. Palmroth (2017), Reconnection rates and x line motion at the magnetopause: Global 2d-3v hybrid-vlasov simulation results, *Journal of Geophysical Research: Space Physics*, pp. n/a–n/a, doi:10.1002/2016JA023709, 2016JA023709.

Hood, L., and G. Schubert (1979), Inhibition of solar wind impingement on mercury by planetary induction currents, *Journal of Geophysical Research: Space Physics*, *84*(A6), 2641–2647.

Janhunen, P., M. Palmroth, T. Laitinen, I. Honkonen, L. Juusola, G. Facsk, and T. Pulkkinen (2012), The gumics-4 global {MHD} magnetosphereionosphere coupling simulation, *Journal of Atmospheric and Solar-Terrestrial Physics*, *80*, 48 – 59, doi:http://dx.doi.org/10.1016/j.jastp.2012.03.006.

Jia, X., J. A. Slavin, T. I. Gombosi, L. K. S. Daldorff, G. Toth, and B. van der Holst (2015), Global mhd simulations of mercury's magnetosphere with coupled planetary interior: Induction effect of the planetary conducting core on the global interaction, *Journal of Geophysical Research: Space Physics*, *120*(6), 4763–4775, doi:10.1002/2015JA021143, 2015JA021143.

Jiang, G., and C. Shu (1996), Efficient implementation of weighted ENO schemes, *J. Comput. Phys.*, *126*(1), 202–228.

Jiang, Y., C.-W. Shu, and M. Zhang (2013), Free-stream preserving finite difference schemes on curvilinear meshes, *Brown University, Scientific Computing Group, Report*, *10*, 2013.

Kabin, K., T. I. Gombosi, D. L. De Zeeuw, and K. G. Powell (2000), Interaction of Mercury with the solar wind, *Icarus*, *143*, 397–406.

Kabin, K., et al. (2008), Global {MHD} modeling of mercury's magnetosphere with applications to the {MESSENGER} mission and dynamo theory, *Icarus*, *195*(1), 1 – 15, doi:http://dx.doi.org/10.1016/j.icarus.2007.11.028.

Kallio, E., and P. Janhunen (2003), Modelling the solar wind interaction with mercury by a quasi-neutral hybrid model, in *Annales Geophysicae*, vol. 21, pp. 2133–2145.

Kidder, A., R. Winglee, and E. Harnett (2008), Erosion of the dayside magnetosphere at mercury in association with ion outflows and flux rope generation, *Journal of Geophysical Research: Space Physics*, *113*(A9).

Kivelson, M. G., and C. T. Russell (1995), Geophysical coordinate transformations, in *Introduction to Space Physics*, edited by M. G. Kivelson and C. T. Russell, pp. 531–543, Cambridge University Press, Cambridge, UK.

Koren, B. (1993), A robust upwind discretisation method for advection, diffusion and source terms, in *Numerical Methods for Advection-Diffusion Problems*, edited by C. Vreugdenhil and B.Koren, p. 117, Vieweg, Braunschweig.

LaBelle, J., et al. (1987), Ampte irm observations of waves associated with flux transfer events in the magnetosphere, *Journal of Geophysical Research: Space Physics*, *92*(A6), 5827–5843.

Lapenta, G. (2012), Particle simulations of space weather, *J. Comput. Phys.*, *231*, 795–821.

Lapenta, G., S. Markidis, A. Divin, M. Goldman, and D. Newman (2010), Scales of guide field reconnection at the hydrogen mass ratio, *Physics of Plasmas*, *17*(8), 082,106, doi:10.1063/1.3467503.

Lax, P. D. (1954), Weak solutions of nonlinear hyperbolic equations and their numerical computation, *Communications on Pure and Applied Mathematics*, *7*, 159–193.

LeVeque, R. J. (1992), *Numerical methods for conservation laws*, Springer Science & Business Media.

Li, Z., and F. A. Jaberi (2012), A high-order finite difference method for numerical simulations of supersonic turbulent flows, *Int. J. Numer. Meth. Fluids*, *68*, 740–766, doi:10.1002/fld.2531.

Liu, X.-D., S. Osher, and T. Chan (1994), Weighted essentially non-oscillatory schemes, *Journal of computational physics*, *115*(1), 200–212.

Lu, S., Y. Lin, V. Angelopoulos, A. Artemyev, P. Pritchett, Q. Lu, and X. Wang (2016), Hall effect control of magnetotail dawn-dusk asymmetry: A three-dimensional global hybrid simulation, *Journal of Geophysical Research: Space Physics*.

Lyon, J., J. Fedder, and C. Mobarry (2004), The Lyon-Fedder-Mobarry (LFM) global MHD magnetospheric simulation code, *J. Atmos. Sol-Terr. Phys.*, *66*, 1333.

Ma, Z., and A. Bhattacharjee (2001), Hall magnetohydrodynamic reconnection: The geospace environment modeling challenge, *JGR*, *106*.

Malakit, K., M. A. Shay, P. A. Cassak, and D. Ruffolo (2013), New electric field in asymmetric magnetic reconnection, *Physical review letters*, *111*(13), 135,001.

Markidis, S., G. Lapenta, and Rizwan-Uddin (2010), Multi-scale simulations of plasma with ipic3d, *Mathematics and Computers in Simulation*, *80*, 1509–1519, doi:10.1016/j.matcom.2009.08.038.

Mason, R. J. (1981), Implicit moment particle simulation of plasmas, *J. Comput. Phys.*, *41*, 233–244.

McCorquodale, P., and P. Colella (2011), A high-order finite-volume method for conservation laws on locally refined grids, *Communications in Applied Mathematics and Computational Science*, *6*(1), 1–25.

Mignone, A., G. Bodo, S. Massaglia, T. Matsakos, O. Tesileanu, C. Zanni, and A. Ferrari (2007), Pluto: a numerical code for computational astrophysics, *The Astrophysical Journal Supplement Series*, *170*(1), 228.

Mignone, A., P. Tzeferacos, and G. Bodo (2010), High-order conservative finite difference glm–mhd schemes for cell-centered mhd, *Journal of Computational Physics*, *229*(17), 5896–5920.

Miyoshi, T., and K. Kusano (2005), A multi-state HLL approximate Riemann solver for ideal magnetohydrodynamics, *J. Comput. Phys.*, *208*, 315–344, doi: 10.1016/j.jcp.2005.02.017.

Müller, J., S. Simon, Y.-C. Wang, U. Motschmann, D. Heyner, J. Schüle, W.-H. Ip, G. Kleindienst, and G. J. Pringle (2012), Origin of mercury's double magnetopause: 3d hybrid simulation study with aikef, *Icarus*, *218*(1), 666–687.

Nagai, T., I. Shinohara, M. Fujimoto, M. Hoshino, Y. Saito, S. Machida, and T. Mukai (2001), Geotail observations of the Hall current system: Evidence of magnetic reconnection in the magnetotail, *J. Geophys. Res.*, *106*, 25,929, doi: 10.1029/2001JA900038.

Nonomura, T., N. Iizuka, and K. Fujii (2010), Freestream and vortex preservation properties of high-order weno and wcns on curvilinear grids, *Computers & Fluids*, *39*(2), 197–214.

Oieroset, M. e. a. (2001), In situ detection of collisionless reconnection in the earth's magnetotail, *Nature*, *412*.

Owen, C., et al. (2008), Cluster observations of crater flux transfer events at the dayside high-latitude magnetopause, *Journal of Geophysical Research: Space Physics*, *113*(A7).

Parker, E. (1965), Dynamical theory of the solar wind, *Space Science Reviews*, *4*(5-6), 666–708.

Parker, E. N. (1957), Sweet's mechanism for merging magnetic fields in conducting fluids, *Journal of Geophysical Research*, *62*(4), 509–520.

Parker, E. N. (1958), Dynamics of the interplanetary gas and magnetic fields, *Astrophys. J.*, *128*(3), 664–676.

Peng, I. B., S. Markidis, A. Vaivads, J. Vencels, J. Amaya, A. Divin, E. Laure, and G. Lapenta (2015), The formation of a magnetosphere with implicit particle-in-cell simulations, *Procedia Computer Science*, *51*, 1178–1187.

Phan, T., J. Drake, M. Shay, F. Mozer, and J. Eastwood (2007), Evidence for an elongated (¿ 60 ion skin depths) electron diffusion region during fast magnetic reconnection, *Physical review letters*, *99*(25), 255,002.

Porth, O., C. Xia, T. Hendrix, S. Moschou, and R. Keppens (2014), Mpi-amrvac for solar and astrophysics, *The Astrophysical Journal Supplement Series*, *214*(1), 4.

Powell, K., P. Roe, T. Linde, T. Gombosi, and D. L. De Zeeuw (1999), A solution-adaptive upwind scheme for ideal magnetohydrodynamics, *J. Comput. Phys.*, *154*, 284–309, doi:10.1006/jcph.1999.6299.

Pritchett, P. (2013), The influence of intense electric fields on three-dimensional asymmetric magnetic reconnection, *Physics of Plasmas*, *20*(6), 061,204.

Qiu, J., and C.-W. Shu (2002), On the construction, comparison, and local characteristic decomposition for high-order central weno schemes, *Journal of Computational Physics*, *183*(1), 187–209.

Raeder, J. (2006), Flux transfer events: 1. generation mechanism for strong southward imf, *Annales Geophysicae*, *24*, 381–392.

Raeder, J., et al. (2001), Global simulation of the Geospace Environment Modeling substorm challenge event, *J. Geophys. Res.*, *106*, 281.

Reed, W. H., and T. Hill (1973), Triangularmesh methodsfor the neutrontransportequation, *Los Alamos Report LA-UR-73-479*.

Ricci, P., J. U. Brackbill, W. Daughton, and G. Lapenta (2004), Collisionless magnetic reconnection in the presence of a guide field, *Phys. Plasmas*, *11*, 4102.

Ridley, A., T. Gombosi, and D. Dezeeuw (2004), Ionospheric control of the magnetosphere: conductance, *Annales Geophysicae*, *22*, 567–584, doi:10.5194/angeo-22-567-2004.

Rijnbeek, R., S. Cowley, D. Southwood, and C. Russell (1984), A survey of dayside flux transfer events observed by ISEE 1 and 2 magnetometers, *J. Geophys. Res.*, *89*, 786.

Roe, P. L. (1981), Approximate Riemann solvers, parameter vectors, and difference schemes, *J. Comput. Phys.*, *43*, 357–372.

Rusanov, V. (1961), Calculation of interaction of non-steady schock waves with obstacles, *J. Comp. Math. and Phys.*, *1*, 267.

Russell, C., and R. Elphic (1978), Initial ISEE magnetometer results: Magnetopause observations, *Space Sci. Rev.*, *22*, 681.

Shay, M. A., and J. F. Drake (1998), The role of electron dissipation on the rate of collisionless magnetic reconnection, *Geophys. Res. Lett.*, *25*, 3759, doi: 10.1029/1998GL900036.

Shay, M. A., J. F. Drake, and M. Swisdak (2007), Two-scale structure of the electron dissipation region during collisionless magnetic reconnection, *Phys. Rev. Lett.*, *99*, 155,002, doi:10.1103/PhysRevLett.99.155002.

Shen, C., J.-M. Qiu, and A. Christlieb (2011), Adaptive mesh refinement based on high order finite difference weno scheme for multi-scale simulations, *Journal of Computational Physics*, *230*(10), 3780–3802.

Shepherd, L., and P. Cassak (2012), Guide field dependence of 3-dx-line spreading during collisionless magnetic reconnection, *Journal of Geophysical Research: Space Physics*, *117*(A10).

Shu, C., and S. Osher (1988), Efficient implementation of essentially non-oscillatory shock-capturing schemes, *J. Comput. Phys.*, *77*(2), 439–471.

Shu, C., and S. Osher (1989), Efficient implementation of essentially non-oscillatory shock-capturing schemes: II, *J. Comput. Phys.*, *83*(1), 32–78.

Shu, C.-W. (2009), High order weighted essentially nonoscillatory schemes for convection dominated problems, *SIAM review*, *51*(1), 82–126.

Sibeck, D., M. Kuznetsova, V. Angelopoulos, K.-H. Glaßmeier, and J. McFadden (2008), Crater ftes: Simulation results and themis observations, *Geophysical Research Letters*, *35*(17).

Slavin, J. A., and R. E. Holzer (1979), The effect of erosion on the solar wind stand-off distance at Mercury, *J. Geophys. Res.*, *84*, 2076–.

Slavin, J. A., et al. (2009), Messenger observations of magnetic reconnection in mercury's magnetosphere, *science*, *324*(5927), 606–610.

Slavin, J. A., et al. (2012), Messenger and mariner 10 flyby observations of magnetotail structure and dynamics at mercury, *Journal of Geophysical Research: Space Physics*, *117*(A1).

Smith, D. E., et al. (2012), Gravity field and internal structure of mercury from messenger, *science*, *336*(6078), 214–217.

Sokolov, I., E. V. Timofeev, J. Sakai, and K. Takayama (2002), Artificial wind – a new framework to construct simple and efficient upwind shock-capturing schemes, *J. Comput. Phys.*, *181*, 354–393, doi:10.1006/jcph.2002.7130.

Suess, S. T., and B. E. Goldstein (1979), Compression of the hermaean magnetosphere by the solar wind, *Journal of Geophysical Research: Space Physics*, *84*(A7), 3306–3312.

Sun, W., S. Fu, J. Slavin, J. Raines, Q. Zong, G. Poh, and T. Zurbuchen (2016), Spatial distribution of mercury's flux ropes and reconnection fronts: Messenger observations, *Journal of Geophysical Research: Space Physics*, *121*(8), 7590–7607.

Suresh, A., and H. T. Huynh (1997), Accurate monotonicity-preserving schemes with runge-kutta time stepping, *J. Comput. Phys.*, *136*, 83.

Thomas, P., and C. Lombard (1979), Geometric conservation law and its application to flow computations on moving grids, *AIAA journal*, *17*(10), 1030–1037.

Tóth, G., Y. J. Ma, and T. I. Gombosi (2008), Hall magnetohydrodynamics on block adaptive grids, *J. Comput. Phys.*, *227*, 6967–6984, doi:10.1016/j.jcp.2008.04.010.

Tóth, G., Y. Chen, T. I. Gombosi, P. Cassak, , S. Markidis, and B. Peng (2017, submitted paper), Scaling the ion inertial length and its implications for modeling reconnection in global simulations, *J. Geophys. Res.*

Tóth, G., et al. (2005), Space Weather Modeling Framework: A new tool for the space science community, *J. Geophys. Res.*, *110*, A12,226, doi:10.1029/2005JA011126.

Tóth, G., et al. (2012), Adaptive numerical algorithms in space weather modeling, *J. Comput. Phys.*, *231*, 870–903, doi:10.1016/j.jcp.2011.02.006.

Tóth, G., et al. (2016), Extended magnetohydrodynamics with embedded particle-in-cell simulation of ganymede's magnetosphere, *J. Geophys. Res.*, *121*, doi:10.1002/2015JA021997.

van Leer, B. (1979), Towards the ultimate conservative difference scheme. V. A second-order sequel to Godunov's method, *J. Comput. Phys.*, *32*, 101–136.

Visbal, M. R., and D. V. Gaitonde (2002), On the use of higher-order finite-difference schemes on curvilinear and deforming meshes, *Journal of Computational Physics*, *181*(1), 155–185.

Walsh, A., et al. (2014), Dawn–dusk asymmetries in the coupled solar wind–magnetosphere–ionosphere system: a review, *Ann. Geophys*, *32*, 705–737.

Wang, C.-P., M. Gkioulidou, L. R. Lyons, and V. Angelopoulos (2012), Spatial distributions of the ion to electron temperature ratio in the magnetosheath and plasma sheet, *Journal of Geophysical Research: Space Physics*, *117*(A8).

Wang, Y.-C., J. Mueller, U. Motschmann, and W.-H. Ip (2010), A hybrid simulation of mercury's magnetosphere for the messenger encounters in year 2008, *Icarus*, *209*(1), 46–52.

Winslow, R. M., B. J. Anderson, C. L. Johnson, J. A. Slavin, H. Korth, M. E. Purucker, D. N. Baker, and S. C. Solomon (2013), Mercury's magnetopause and bow shock from messenger magnetometer observations, *Journal of Geophysical Research: Space Physics*, *118*(5), 2213–2227.

Woodward, P., and P. Colella (1984), The numerical simulation of two-dimensional fluid flow with strong shocks, *J. Comput. Phys.*, *54*, 115–173.

Zhang, H., et al. (2010), Evidence that crater flux transfer events are initial stages of typical flux transfer events, *Journal of Geophysical Research: Space Physics*, *115*(A8).